

1 **Jet-Track Correlation Studies of the Quark Gluon Plasma**

2 BY

3 HALLIE CAUSEY TRAUGER

4 M.Ed. University of Illinois at Chicago, 2015

5 M.S. University of Illinois at Chicago, 2014

6 B.A. University of Chicago, 2010

7 THESIS

8 Submitted in partial fulfilment of the requirements

9 for the degree of Doctor of Philosophy in Physics

10 in the Graduate College of the University of Illinois at Chicago, 2017

11 Chicago, IL

12 DEFENSE COMMITTEE:

13 Olga Evdokimov, Chair and Advisor

14 David Hofman

15 Zhenyu Ye

16 Misha Stephanov

17 Julia Velkovska, Vanderbilt University

18

ACKNOWLEDGEMENTS

19 Thanks go here...

20

HCT

21

CONTRIBUTION OF AUTHORS

- 22 - Note previous publications (HIN-14-016, HIN-15-011, HIN-16-020)
- 23 - Describe CMS authorship policy
- 24 - Outline general CMS inputs (reconstruction etc.) that contributed to work
- 25 - Outline aspects that are my own work (and others' contributions to these as well, esp. Run 2)

CONTENTS

27	1 Introduction	1
28	2 Jets in the Quark Gluon Plasma	2
29	2.1 The Quark Gluon Plasma	2
30	2.2 Collective behavior in the QGP	2
31	2.3 Jets as probes of the QGP	2
32	2.4 Models of jet energy loss	3
33	3 The Large Hadron Collider and the CMS Detector	4
34	3.1 The Large Hadron Collider	4
35	3.2 The CMS detector	5
36	3.3 Trackers in the CMS detector	5
37	3.4 Calorimeters in the CMS detector	7
38	3.5 The CMS trigger system	7
39	4 Track reconstruction and correction	9
40	4.1 Track reconstruction in pp collisions	9
41	4.2 Track reconstruction in PbPb collisions	10
42	4.3 High purity tracks	11
43	4.4 Tracking efficiency and fake rate evaluation and correction	12
44	5 Jet reconstruction and correction	14
45	5.1 Jet reconstruction with the anti- k_t algorithm	14
46	5.2 Underlying event subtraction in PbPb data	16
47	5.3 Jet energy corrections	17
48	6 Data and Monte Carlo samples	19
49	6.1 Data samples and event selection	19
50	6.2 Collision centrality determination and classes	20
51	6.3 Monte Carlo simulation	21
52	6.4 Jet selection and dijet asymmetry classes	25
53	6.5 Track selection and classes	25
54	6.6 Summary of analysis bins	27
55	7 Jet-track correlation measurements	28
56	7.1 Analysis procedure	28
57	7.2 Jet-track correlation pair-acceptance correction	29
58	7.3 Separation of correlations into long range and short-range components	29
59	7.4 Residual Jet Fragmentation Function correction	33
60	7.5 Background fluctuation bias correction	37
61	7.6 Evaluation of systematic uncertainties	44
62	8 Discussion of results	48
63	8.1 Inclusive jet particle density correlation results	48
64	8.2 Dijet correlation results	59
65	8.3 Jet shapes	68

66	8.4	Decomposition of hemisphere momentum balance in dijet events	72
67	8.5	Theory implications of these results	84
68	9	Conclusion	85
69	References		86
70	Appendices		88
71	A	Jet kinematics	88
72	B	Background fitting details	102
73	C	Pair acceptance and event decomposition systematic uncertainties	106
74	D	Correlation widths and related uncertainty	108
75	Vita		112

LIST OF TABLES

77	I	Summary of data samples and number of selected events	19
78	II	Summary of Monte Carlo samples and generated events at 2.76 TeV	23
79	III	Summary of Monte Carlo samples and generated events at 5.02 TeV	24
80	IV	Summary of data selections and analysis bins	27
81	V	Systematic uncertainties for particle density correlation studies at 2.76 TeV	46
82	VI	Systematic uncertainties for particle density correlation studies at 5.02 TeV	46
83	VII	Systematic uncertainties for balanced and unbalanced dijets in transverse momentum distribution studies at 2.76 TeV	47
84			

LIST OF FIGURES

86	1	CMS detector perspective drawing	6
87	2	Diagram of CMS trackers	6
88	3	Diagram of the HCAL	8
89	4	Tracking efficiency correction example	13
90	5	Closure with and without JFF-JEC for quark and gluon jets.	18
91	6	Centrality distribution for PYTHIA+HYDJET reweighted to match centrality distribution of PbPb data.	22
93	7	Vertex z distribution for PYTHIA+HYDJET reweighted to match centrality distribution of PbPb data.	22
95	8	Vertex z distribution for PYTHIA reweighted to match centrality distribution of pp data.	23
97	9	Illustration of the pair-acceptance correction procedure	30
98	10	Illustration of the event decomposition procedure without $\Delta\phi$ fitting	30
99	11	Illustration of the event decomposition procedure with $\Delta\phi$ fitting	31
100	12	Jet fragmentation function bias corrections for particles with $1 < p_T^{\text{trk}} < 2$ GeV	34
101	13	Jet fragmentation function bias corrections for particles with $2 < p_T^{\text{trk}} < 3$ GeV	34
102	14	Jet fragmentation function bias corrections for particles with $3 < p_T^{\text{trk}} < 4$ GeV	35
103	15	Jet fragmentation function bias corrections for particles with $4 < p_T^{\text{trk}} < 8$ GeV	35
104	16	Integrated yield attributed to jet fragmentation function bias as a function of p_T^{trk}	36
105	17	Integrated yield attributed to jet fragmentation function bias as a function of centrality	36
106	18	Background fluctuation bias corrections for particles with $1 < p_T^{\text{trk}} < 2$ GeV	38
107	19	Background fluctuation bias corrections for particles with $2 < p_T^{\text{trk}} < 3$ GeV	38
108	20	Background fluctuation bias corrections for particles with $3 < p_T^{\text{trk}} < 4$ GeV	39
109	21	Background fluctuation bias corrections for particles with $4 < p_T^{\text{trk}} < 8$ GeV	39
110	22	Integrated yield attributed to background fluctuation bias as a function of p_T^{trk}	40
111	23	Data-driven check of integrated yields attributed to background fluctuation bias	41
112	24	Data-driven check of correlated $\Delta\eta$ yields attributed to background fluctuation bias	42
113	25	Comparison of background selection bias effect for quark verus gluon jets	43
114	26	Inclusive jet $\Delta\eta$ correlations for tracks with $1 < p_T^{\text{trk}} < 2$ GeV at 2.76 TeV	49
115	27	Inclusive jet $\Delta\phi$ correlations for tracks with $1 < p_T^{\text{trk}} < 2$ GeV at 2.76 TeV	50
116	28	Inclusive jet $\Delta\eta$ correlations for tracks with $2 < p_T^{\text{trk}} < 3$ GeV at 2.76 TeV	51
117	29	Inclusive jet $\Delta\phi$ correlations for tracks with $2 < p_T^{\text{trk}} < 3$ GeV at 2.76 TeV	52
118	30	Inclusive jet $\Delta\eta$ correlations for tracks with $3 < p_T^{\text{trk}} < 4$ GeV at 2.76 TeV	53
119	31	Inclusive jet $\Delta\phi$ correlations for tracks with $3 < p_T^{\text{trk}} < 4$ GeV at 2.76 TeV	54
120	32	Inclusive jet $\Delta\eta$ correlations for tracks with $4 < p_T^{\text{trk}} < 8$ GeV at 2.76 TeV	55
121	33	Inclusive jet $\Delta\phi$ correlations for tracks with $4 < p_T^{\text{trk}} < 8$ GeV at 2.76 TeV	56
122	34	Inclusive jet $\Delta\eta$ correlations at 5.02 TeV	56
123	35	Inclusive jet $\Delta\phi$ correlations at 5.02 TeV	57
124	36	Inclusive jet distribution of charged particles as a function of Δr at 5.02 TeV	57
125	37	Integrated inclusive jet charged particle yields at 2.76 and 5.02 TeV	58
126	38	Dijet $\Delta\eta$ correlations for tracks with $1 < p_T^{\text{trk}} < 2$ GeV at 2.76 TeV	60
127	39	Dijet $\Delta\phi$ correlations for tracks with $1 < p_T^{\text{trk}} < 2$ GeV at 2.76 TeV	61
128	40	Integrated charged particle yields for inclusive, leading, and subleading jets	62
129	41	Leading jet $\Delta\eta$ correlation widths as a function of p_T^{trk} at 2.76 TeV	64
130	42	Leading jet $\Delta\phi$ correlation widths as a function of p_T^{trk} at 2.76 TeV	65
131	43	Subleading jet $\Delta\eta$ correlation widths as a function of p_T^{trk} at 2.76 TeV	66

132	44	Subleading jet $\Delta\phi$ correlation widths as a function of p_T^{trk} at 2.76 TeV	67
133	45	Inclusive jet shape at 5.02 TeV, shown differentially in p_T^{trk}	69
134	46	Leading jet shape at 2.76 TeV, shown differentially in p_T^{trk}	70
135	47	Subleading jet shape at 2.76 TeV, shown differentially in p_T^{trk}	71
136	48	Dijet subleading-to-leading hemisphere momentum balance for balanced dijets	74
137	49	Dijet subleading-to-leading hemisphere momentum balance for unbalanced dijets . .	75
138	50	Jet peak subleading-to-leading momentum balance for balanced dijets	76
139	51	Jet peak subleading-to-leading momentum balance for unbalanced dijets	77
140	52	long-range subleading-to-leading momentum balance for balanced dijets	79
141	53	long-range subleading-to-leading momentum balance for unbalanced dijets	80
142	54	Integrated transverse momentum in the long-range $\Delta\phi$ -correlated distribution as a function of track- p_T	81
143	55	Relative contributions from jet peaks and long-range asymmetry to the double dif- ference PbPb-pp, subleading-leading in total hemisphere transverse momentum for central collisions	82
144	56	Relative contributions from jet peaks and long-range asymmetry to the double dif- ference PbPb-pp, subleading-leading in total hemisphere transverse momentum for peripheral collisions	83
145	57	Distribution of transverse momentum, pseudorapidity, and azimuthal distribution of all jet selections for Pythia data compared to PYTHIA simulation.	88
146	58	Transverse momentum distribution of all jet selections for PbPb data at 2.76 TeV compared to PYTHIA+HYDJET simulation.	89
147	59	Pseudorapidity distribution of all jet selections for PbPb data at 2.76 TeV compared to PYTHIA+HYDJET simulation.	90
148	60	Azimuthal angle distribution of all jet selections for PbPb data at 2.76 TeV compared to PYTHIA+HYDJET simulation for each collision centrality bin.	91
149	61	Distribution of pseudorapidity distribution of all jet selections for PbPb data com- pared to PYTHIA+HYDJET simulation for each collision centrality bin.	92
150	62	Transverse momentum distribution for PbPb data compared to PYTHIA+HYDJET simulation for each collision centrality bin.	92
151	63	Jet η distribution for PbPb data compared to PYTHIA+HYDJET simulation for each collision centrality bin.	92
152	64	Jet ϕ distribution for PbPb data compared to PYTHIA+HYDJET simulation for each collision centrality bin.	93
153	65	Jet p_T , η , and ϕ for all pp dijets and for pp dijets with $A_J: 0 < A_J < 0.11$	94
154	66	Jet p_T , η , and ϕ for all pp dijets and for pp dijets with $A_J: 0.11 < A_J < 0.22$	95
155	67	Jet p_T , η , and ϕ for all pp dijets and for pp dijets with $A_J: 0.22 < A_J < 0.33$	96
156	68	Jet p_T , η , and ϕ for all pp dijets and for pp dijets with $A_J: A_J > 0.33$	97
157	69	Jet p_T , η , and ϕ for all PbPb dijets and for PbPb dijets with $0 < A_J < 0.11$	98
158	70	Jet p_T , η , and ϕ for all PbPb dijets and for PbPb dijets with $0.11 < A_J < 0.22$. . .	99
159	71	Jet p_T , η , and ϕ for all PbPb dijets and for PbPb dijets with $0.22 < A_J < 0.33$. . .	100
160	72	Jet p_T , η , and ϕ for all PbPb dijets and for PbPb dijets with $A_J > 0.33$	101
161	73	Dijet background fits (preliminary step)	102
162	74	Leading jet background fits	103
163	75	Subleading jet background fits	104
164	76	Inclusive jet background fits	105
165	77	Pair acceptance uncertainty determination	106
166	78	Background subtraction uncertainty determination	107

180	79	Width determination for PbPb leading jets	108
181	80	Width determination for pp leading jets	109
182	81	Width determination for PbPb subleading jets	110
183	82	Width determination for pp subleading jets	111

LIST OF ABBREVIATIONS

BNL	Brookhaven National Laboratory
CERN	Conseil Européen pour la Recherche Nucléaire
CMS	Compact Muon Solenoid
ECAL	Electromagnetic Calorimeter
E_T	Transverse Energy
HCAL	Hadronic Calorimeter
HF	Hadronic Forward
HLT	High Level Trigger
JEC	Jet Energy Correction
JES	Jet Energy Scale
JFF	Jet Fragmentation Function
LHC	Large Hadron Collider
MC	Monte Carlo
PbPb	Lead-lead (collision data)
pPb	Proton-lead (collision data)
pp	Proton-proton (collision data)
p_T	Transverse Momentum
QCD	Quantum Chromodynamics
QGP	Quark Gluon Plasma
RHIC	Relativistic Heavy Ion Collider
UE	Underlying Event

SUMMARY

1 INTRODUCTION

187

2 JETS IN THE QUARK GLUON PLASMA

188 **2.1 The Quark Gluon Plasma**

- 189 – Anticipation based on QCD
 - 190 – QCD phase diagram
 - 191 – Early predicted signatures and motivation for heavy ion collisions

192 **2.1.1 Creating the QGP in heavy ion collisions**

- 193 – Experimental programs (RHIC, LHC)
 - 194 – Basic kinematic variables (pT, rapidity, pseudorapidity, phi)
 - 195 – Centrality (Glauber, other centrality classification schemes)

196 **2.1.2 Basic properties of the QGP and stages of heavy ion collisions**

- 197 – Temperature and energy density
 - 198 – Time-evolution (initial conditions, hydrodynamic expansion of the QGP, hadronization)

199 **2.2 Collective behavior in the QGP**

- 200 – Flow and interpretations (including harmonic decomp. examples)
 - 201 – Hydro
 - 202 – IS fluctuations

203 **2.3 Jets as probes of the QGP**

- 204 – Why consider high-pT probes?
 - 205 – Quenching studies with high-pT tracks
 - 206 – Variable RAA
 - 207 – What is a jet and why study fully reconstructed jets?
 - 208 – Jet quenching jets
 - 209 – Previous jet shapes –*j* include dR definition
 - 210 – Dijet motivation and dijet balance studies
 - 211 – Missing-pT measurements

212 **2.4 Models of jet energy loss**

213 – And efforts to account for jet shapes $dR \geq 0.3$

214 – And comparison to mpT

215 – Need for detailed characterization of angular distribution of particles and pT in the event,

216 as presented here

217 **3 THE LARGE HADRON COLLIDER AND THE CMS DETECTOR**

218 **3.1 The Large Hadron Collider**

219 The Large Hadron Collider (LHC), located at CERN near Geneva, is the largest and highest-
220 energy particle accelerator in the world. It consists of two counter-rotating particle beam line in
221 a tunnel 26.7 km in circumference, located between 45 m and 170 m underground [16]. During
222 standard operation, the LHC collides beams of protons accelerated and focused using a series
223 of superconducting magnets, cooled to below 2 K using supercritical helium. Particle beams are
224 brought together for collisions at in experimental detectors at four points in the accelerator ring: the
225 ATLAS, CMS, ALICE, and LHCb detectors. In addition to the proton-proton (pp) data collected
226 at center-of-mass energies $\sqrt{S_{NN}} = 7 \text{ TeV}$, 8 TeV , and 13 TeV , the LHC has also been operated
227 for heavy ion physics by colliding with fully-stripped lead nuclei ($^{182}\text{Pb}^{82+}$) in lead-lead (PbPb)
228 and proton-lead (pPb) collisions. Heavy ion runs at the LHC have included PbPb data and pp
229 “reference” runs at $\sqrt{S_{NN}} = 2.76 \text{ TeV}$ (2011 and 2013, respectively) and 5.02 TeV (2015) and pPb
230 data at $\sqrt{S_{NN}} = 5.02 \text{ TeV}$ (2013 and 2016) and 8.16 TeV (2016). This analysis relies on PbPb
231 data at 2.76 TeV and 5.02 TeV , and corresponding pp reference data at the same center-of-mass
232 energies.

233 In peak proton-proton operation, the LHC collides 2,808 bunches each containing approx-
234 imately 10^{11} protons with a minimum bunch spacing of 25 ns, for a maximum luminosity of
235 $10^{34} \text{ cm}^{-2} \text{ s}^{-1}$ delivered to the high-luminosity detectors (ATLAS and CMS). The lead-lead per-
236 formance target of $10^{27} \text{ cm}^{-2} \text{ s}^{-1}$ delivered via 592 bunches of 10^7 lead ions was slightly exceeded
237 during the 2015 PbPb run. At this high-intensity frontier, it is common during nominal pp data
238 collection and possible in PbPb data collection that multiple distinct proton-proton collisions may
239 occur within a recorded event in a phenomenon known as “pile-up.” However, pile-up is relatively
240 rare in PbPb collisions due to the lower luminosities, and in the present analysis only one primary
241 vertex will be considered (with products of any other possible interactions removed via background
242 subtraction procedures).

243 **3.2 The CMS detector**

244 The CMS detector is named for the Compact Muon Solenoid at its heart: a superconducting magnet
245 with magnetic field of 3.8 T, length of 13 m, diameter of 6 m, and weight 14,000 tons. Inside
246 of this solenoid, the detector includes silicon pixel and strip detectors for particle tracking (see
247 Sec. 3.3 for a detailed explanation), and electromagnetic and hadronic calorimeters (see Sec. 3.4).
248 Calorimeters within the solenoid volume are complemented by additional calorimetry outside of the
249 solenoid that provides coverage in the very forward direction close to the beam line, including the
250 hadronic forward (HF) calorimeter in the region $3.0 < |\eta| < 5.2$ used in this analysis for centrality
251 determination, and the Zero Degree and CASTOR calorimeters in the even more forward region.
252 The CMS detector also includes an extensive muon system outside of the solenoid volume, consisting
253 of aluminum drift tubes in the barrel region, cathode strip chambers in the forward region, and a
254 complementary system of resistive plate chambers (not discussed in detail here as muons are not of
255 primary relevance to this analysis). Full details about the CMS detector may be found in Ref. [5],
256 and a perspective drawing of the CMS detector from this report is shown in Fig. 1.

257 In the CMS detector, the $+z$ axis is defined to be horizontal, pointing to the West along
258 the beam line direction. The x axis is horizontal, pointing to the South toward the center of the
259 LHC. The $+y$ axis is vertical, pointing upward. The azimuthal angle $\phi = \tan^{-1}(\frac{y}{x})$ is defined in
260 the x - y plane such that $\phi = 0$ is the $+x$ axis. Pseudorapidity $\eta = -\ln(\tan(\frac{\theta}{2}))$ is defined to have the
261 same sign as the $+z$ axis. Pseudorapidity coverage in the CMS detector ranges from $\eta = 0$ at the
262 y -axis, to $|\eta| > 8.3$ in Zero Degree Calorimeter approaching the $+/z$ axis.

263 **3.3 Trackers in the CMS detector**

264 The CMS tracking system consists of a small silicon pixel detector for precise measurement near
265 the interaction point (with three layers with radii 4.4 cm to 10.2 cm), surrounded by a large silicon
266 strip detector with layers to a radius of 110 cm. In both detectors, a cylindrical tracker “barrel” is
267 complemented by “endcap” disks that together provide full azimuthal coverage and pseudorapidity
268 coverage in the range $|\eta| < 2.5$. The pixel detector consists of 66 million pixels in 1440 modules.
269 It provides three-dimensional measurements of “hits,” or interactions of particles with tracker
270 materials, with a transverse resolution $10\mu\text{m}$ and longitudinal resolution $20 - 40\mu\text{m}$ (and a third

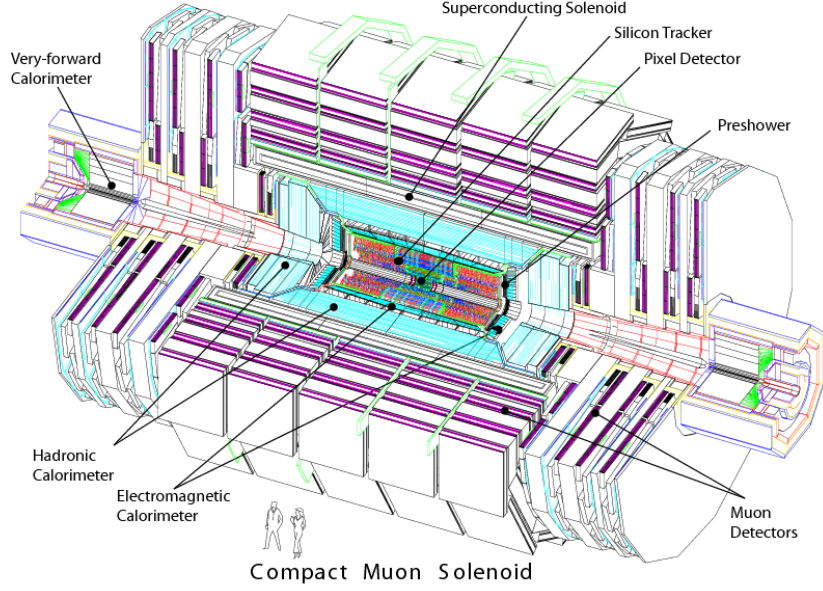


Figure 1. Perspective drawing of the CMS detector, showing component sub-detectors with humans drawn for scale perspective [5].

coordinate provided by the pixel plane). The silicon strip detector consists of 9.3 million strips in 15,148 modules, organized in four components: Tracker Inner Barrel (TIB) and Disks (TID), Tracker Outer Barrel (TOB, covering the region $r > 55$ cm), and Tracker End Caps (TEC, covering the region $124 < |z| < 282$ cm). Figure 2 shows a diagram of the pixel and strip detectors, which have total length 5.8 m and diameter 2.5 m [12]. Track reconstruction and tracking efficiency will be discussed in detail in Sec. 4.

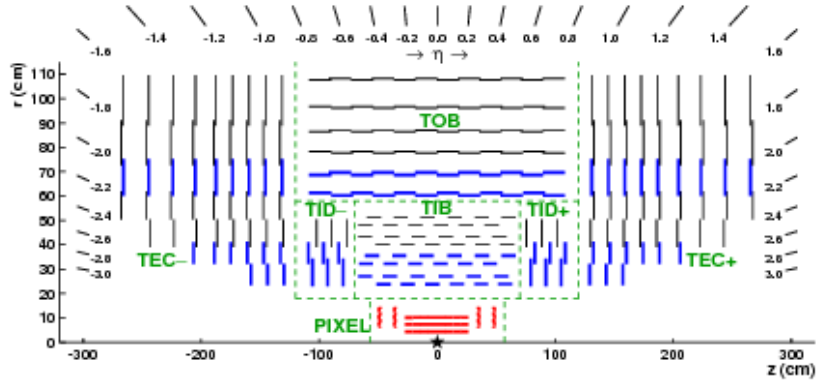


Figure 2. Diagram of CMS pixel and silicon strip detectors in the $r - z$ plane [12].

277 **3.4 Calorimeters in the CMS detector**

278 This analysis relies on electromagnetic and hadronic calorimeters for the energy measurements
279 used as inputs for the reconstruction of high- p_T jets. The ECAL, which measures the energy of
280 charged particles, consists of 75 848 lead tungstate (PbWO_4) crystal scintillators, organized in 5
281 arrays, covering $|\eta| < 1.48$ in a barrel region and $1.48 < |\eta| < 3.0$ in the endcap region. Light
282 from the scintillators is captured with avalanche photodiodes in the barrel region, and vacuum
283 phototriodes in the endcap region. A preshower detector system in front of the ECAL is used to
284 assist in the identification of neutral pions and electrons [5]. ECAL energy resolution ranges from
285 about 1-2.5% (depending $|\eta|$ and photon conversion) in the barrel region, and from 2.5-4% in the
286 endcap region. [18].

287 Hadrons pass through the ECAL and are stopped by the HCAL, a hermetic detector which
288 records their energy using a system of scintillator tiles embedded with wavelength-shifting fibers.
289 The HCAL has three regions, as shown in Fig. 3: barrel (HB), endcap (HE), and an outer region
290 (HO) outside of the solenoid, necessitated by the fact that the HB is volume-limited by the solenoid
291 diameter. In the barrel region $|\eta| < 1.74$, the HCAL cells have widths of 0.087 in pseudorapidity
292 and 0.087 in ϕ , while for $|\eta| > 1.74$ the coverage of the towers increases progressively to a maximum
293 of 0.174 in $\Delta\eta$ and $\Delta\phi$. HCAL towers are mapped onto ECAL towers within the barrel region, and
294 their summed energies are used to determine the location, energy, and axis of jets, as described
295 below in Sec. 5. The HCAL is complimented in the forward region by the HF calorimeters, which
296 each consist quartz fibers in the $\pm z$ directions organized in 432 readout towers in the region $3.0 <$
297 $|\eta| < 5.2$ [5]. In this analysis, only jets from the barrel region of the calorimeters will be included,
298 while the HF detector is used for the determination of PbPb event centrality as described in Sec. 6.2.

299 **3.5 The CMS trigger system**

300 The collision rate at in the LHC is so high that it is impossible to store and process every event
301 that occurs in the CMS detector. A two-level online trigger system is therefore used to select events
302 of interest. Furthermore, data selected with loose trigger requirements (for example “zero bias”
303 data with no selection criteria and “minimum bias” criteria consisting of minimal requirements to
304 demonstrate the presence of a collision event) may also need to be further “prescaled” to limit

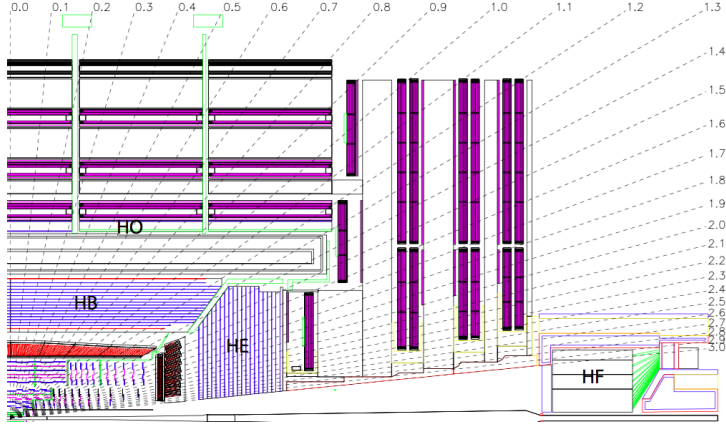


Figure 3. Diagram of the HCAL [5].

305 the rate of recorded events by a specified factor. The trigger system consists of a first (L1) trigger
 306 consisting of programmable electronics that use information from the calorimeter and muon systems
 307 of the detector to select events to record. The L1 trigger operates with an interval of approximately
 308 $4\mu\text{s}$, with a maximum rate of 100 kHz. The next trigger level, the High Level Trigger (HLT), consists
 309 of a processor farm that allows for more sophisticated event selection based on the reconstruction of
 310 physics objects. Reconstruction is performed in a series of steps, or a “HLT path,” chosen to apply
 311 selection in order of increasing reconstruction complexity, so as to minimize processing time [20].
 312 This analysis will rely primarily on two kinds of triggers: minimum bias data, and jet-triggered
 313 data samples selected by requiring the presence of an online reconstructed jet with $p_{\text{T}} > 80 \text{ GeV}$
 314 ($p_{\text{T}} > 100 \text{ GeV}$ for 5.02 TeV PbPb data). No prescale is applied for the jet-triggered data samples
 315 used in this analysis.

4 TRACK RECONSTRUCTION AND CORRECTION

317 4.1 Track reconstruction in pp collisions

318 Standard track reconstruction in CMS occurs in the following steps, summarized here and described
 319 in detail in Ref. [12]:

- 320 • **Hit reconstruction** – In the pixel tracker, zero-suppression is performed by setting an ad-
 321 justable threshold, equivalent charge to 3200 for each pixel. Pixel hits are reconstructed as
 322 clusters of adjacent pixels, requiring a minimum charge equivalent of 4000 electrons (compared
 323 to at least 21,000 electrons deposited by a typical ionizing particle). In the strip detector,
 324 zero-suppression is performed by subtracting the baseline pedestal and noise from the signal,
 325 and clusters are seeded with channels which contain charge at least three times that of the
 326 pedestal. Adjacent strips are added to the cluster if their charge is more than twice that of
 327 the pedestal, and the cluster is kept if its total charge is at least five times larger than the
 328 combined strip noise. Cluster position in the strip detector is determined from the charge-
 329 weighted average of strip positions, corrected for Lorentz drift. The average efficiency for hit
 330 reconstruction in both the pixel and strip detectors (excluding 2.4% of pixel modules and
 331 2.3% of strip modules known to be defective) is > 99 %.
- 332 • **Track seed generation** – Track reconstruction begins by first running a fast track and
 333 vertex reconstruction using the pixel tracker only to reconstruct the beamspot position and
 334 the location of primary vertices in the event. After this, track reconstruction is carried out in
 335 six iterations, each of which begins with “seeds” that define the trajectories and uncertainties
 336 of potential tracks. The first set of seeds are pixel triplets, produced from corresponding sets
 337 of three pixel hits (on a helical track trajectory) with weak constraints on compatibility with
 338 the beam spot to require that the tracks correspond to promptly produced particles. In later
 339 iterations, additional information from vertex reconstruction and the silicon strip detector is
 340 incorporated in seed generation.
- 341 • **Track finding** – The seeds generated in the step above are used as starting points for
 342 track-finding based on the Kalman filter method, implemented in four steps for each tracker
 343 layer. First, track parameters at the starting level are extrapolated, assuming a perfectly

344 helical track trajectory (neglecting multiple scatterings, energy loss, and non-uniformity in
345 the magnetic field), to determine the locations of interception in other pixel layers. The second
346 step is a search for tracker modules consistent with the interception locations determined in
347 the previous step. In the third step, hits from mutually exclusive module groups (i.e. groups
348 of modules for which it is not possible that one track could pass through more than one of
349 the grouped modules) are used to update and refine hit locations (including the possibility of
350 adding “ghost” hits where a particle failed to produce a hit due to module inefficiency) and to
351 calculate the Lorentz drift in the silicon bulk. Finally, in the fourth and last step, new track
352 candidates are formed by adding one compatible hit from each of the module groupings, and
353 trajectories are updated combining this added hit with the original track path extrapolation.
354 All track candidates at a given level are then extrapolated to the next compatible layer and
355 the procedure repeated through five iterations.

- 356 • **Track fitting** – Finally, the track trajectory is refitted to reduce possible biases (due, for
357 example, to the beam spot constraint introduced in initial seed finding), and to remove
358 outlying hits falsely associated to a track.

359 After tracks are reconstructed according to this procedure, the track sample both includes a contri-
360 bution from “fake” tracks (that do not correspond to the trajectory of an ionizing particle), which
361 is reduced by requiring certain selection criteria as discussed in Sec. 4.3. The collection also suffers
362 from detector and reconstruction inefficiencies, which are corrected in this analysis according to
363 the procedure described in Sec. 4.4.

364 4.2 Track reconstruction in PbPb collisions

365 In PbPb collision data, dedicated track reconstruction is necessary due to the dramatically greater
366 multiplicity in PbPb compared to pp collisions. This heavy ion tracking occurs in the following
367 steps, and is detailed in Refs. [15] and [17]:

- 368 • **Hit reconstruction** – Tracker hits are reconstructed following the same basic procedure
369 applied in pp collisions.
- 370 • **Track seed generation** – First, primary vertex positions are reconstructed using only a
371 collection of pixel hits, extrapolated to the region near the beam spot. In PbPb data pileup

372 is negligible, so there is generally only one primary vertex reconstructed in each event. Initial
373 track seeds are then constructed from pixel triplets only. To reduce combinatorial back-
374 grounds, seeds are restricted to those pointing to a region within 2 mm of the primary vertex,
375 and further selections are applied on track p_T , goodness-of-fit (χ^2), and compatibility between
376 the seed trajectory and the primary vertex.

377 • **Track finding** – Track trajectories are propagated through the tracker following a procedure
378 similar to that outlined above for pp data. The track seeding and finding procedure is repeated
379 through three iterations. In the second and third iterations, hits belonging unambiguously to
380 a previously identified tracks are first removed, and then reconstruction is repeated using pixel
381 triplet and pixel pair seeds (in the 2nd and 3rd iterations, respectively). Tracks identified in
382 these later iterations are merged into first-iteration tracks, with duplicates removed based on
383 hit matching.

384

4.3 High purity tracks

385 The track reconstruction procedures described above for pp and PbPb collision data give track
386 collections with significant “fake rates,” or fraction of reconstructed tracks that cannot be associated
387 with a particle. This fake rate is reduced with a series of quality selections, defined in three levels:
388 “loose” criteria define the minimum to keep tracks in track collections, “tight” criteria are somewhat
389 more stringent (sacrificing some lost efficiency for a lower fake rate), and finally “high purity”
390 criteria are most strict and are those applied for most CMS analyses, including those reported
391 here. Track quality in each case is set with flags for each track, and criteria in each case are
392 applied separately at each iterative tracking step. The precise criteria for high purity tracks at
393 each iterative pass are defined in Refs. [12, 15, 17], and include the following types of selections,
394 imposed as a function of p_T and η :

- 395 • Requirements on the number of hits on the track trajectory (N_{hit})
396 • Requirements on the minimum layers in which the track has an associated hit (N_{layers} , and
397 on the maximum intercepted layers in which the track has no assigned hits
398 • A minimum imposed on the goodness-of-fit of the track ($\chi^2/\text{Ndof}/N_{\text{layers}}$ or χ^2/N_{hit})

- 399 • A maximum on relative track- p_T uncertainty
 400 • Maxima on longitudinal and transverse impact parameters (d_z and d_{xy}) with respect to the
 401 primary vertex position and beam spot

402 In pp data, criteria are optimized by the quality metric $Q(\rho) = s/\sqrt{s + \rho b}$, where s = selected
 403 (“real”) tracks, b = selected fake tracks, and parameter $\rho \approx 10$ weights the metric toward min-
 404 imizing the fake rate. In PbPb data from Run 2, optimization is performed via the output of a
 405 multivariate analysis tool (MVA), as detailed in Ref. [17].

406 **4.4 Tracking efficiency and fake rate evaluation and correction**

407 Tracking efficiency for charged particles in pp collisions ranges from approximately 80% at $p_T \approx 0.5$ GeV
 408 to 90% or better at $p_T \approx 10$ GeV and higher. Track reconstruction is more difficult in the heavy-ion
 409 environment due to the high track multiplicity, and tracking efficiency for PbPb collisions ranges
 410 from approximately 30% at 0.5 GeV to about 70% at 10 GeV. Tracking efficiencies are evaluated
 411 using PYTHIA and PYTHIA+HYDJET Monte Carlo simulation, by comparing track distributions as
 412 generated to those after MC samples are passed through GEANT detector simulation and recon-
 413 structed with the algorithms used to reconstruct data. Corrections are derived as a function of
 414 centrality, p_T , η , ϕ , and local charged particle density. Tracking efficiency closure and systematic
 415 uncertainty is evaluated in pythia and pythia+hydjet, comparing generated track p_T , η , and ϕ
 416 distributions to reconstructed distributions before and after correction. For illustration, examples
 417 of these closure checks for 5.02 TeV PYTHIA simulation are shown in Fig. 4. Additional 5% residual
 418 systematic uncertainty is conservatively assigned for possible differences between MC and data that
 419 might affect tracking performance.

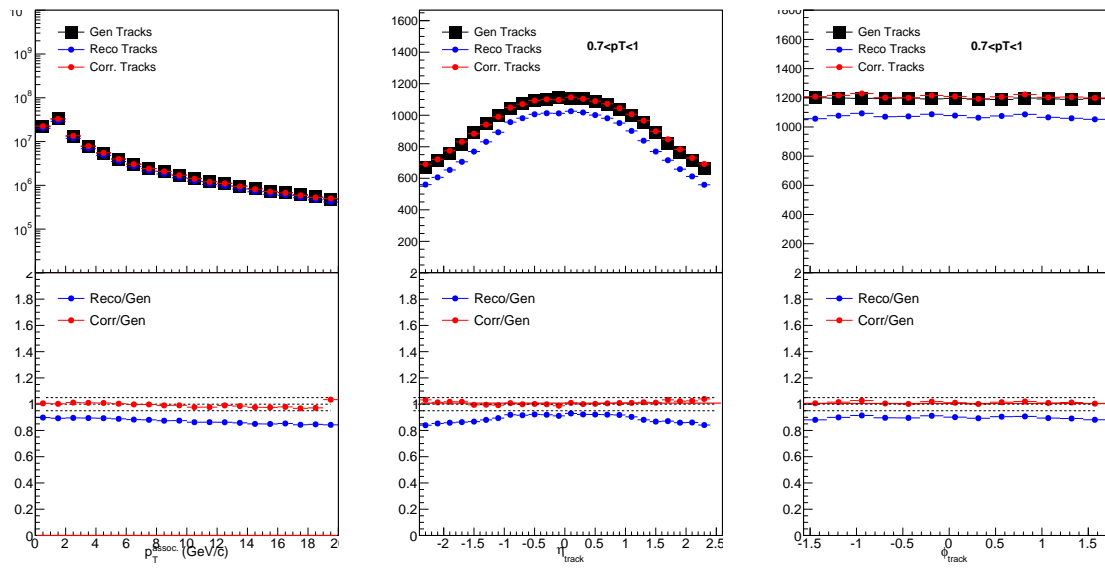


Figure 4. Tracking efficiency correction closure for PYTHIA simulation at 5.02 TeV, comparing tracking generated tracks to uncorrected and corrected reconstructed tracks, as a function of track p_T and of pseudorapidity, and azimuth for the lowest p_T^{trk} bin.

5 JET RECONSTRUCTION AND CORRECTION

421 5.1 Jet reconstruction with the anti- k_t algorithm

422 The goal in jet reconstruction is to identify clusters of hadrons originating from a fragmenting high-
 423 energy parton. In high- p_T jet studies in pp collisions, the general locations of jets in an event may
 424 be qualitatively obvious via large energy deposits in calorimeters; however, there is no clear single
 425 standard of how jet boundaries should be drawn. In practice, jets are defined by the algorithms
 426 used to find and determine their direction. These algorithms fall in two primary categories: “cone
 427 algorithms,” which define jets within specific conical regions (based on the fact that hadronization
 428 has little effect total momentum flow), and “sequential recombination algorithms,” which iteratively
 429 identify and cluster pairs of closest particles to form jets that are not necessarily conical. [23, 3, 4].
 430 Several properties are desireable, from theoretical and experimental perspectives, in jet finding:

- 431 • Straightforward implementation for both theoretical calculations and jet-finding and recon-
 432 struction in experimental measurements
- 433 • Cross-sections that are finite in perturbation theory
- 434 • Infrared and collinear (IRC) safety – the property that a soft collinear emission in a parton
 435 splitting should not modify the overall collection of hard (high- p_T) jets in the event, in
 436 particular avoiding the possibility of non-cancelling divergences in perturbation calculations
- 437 • Soft resilience – clustering jets that are reasonably regular and not overly sensitive to soft
 438 particles, a property motivated by the finite resolution of experimental detectors.

439 Heavy ion jet studies in CMS use the anti- k_t algorithm, a soft-resilient, IRC safe, and straightforward
 440 sequential recombination algorithm [3], implemented in the FastJet framework [4]. The anti- k_t
 441 algorithm clusters entities (calorimeter towers, particles, or partially clustered pseudo-jets) i and
 442 j based on the distance measures d_{ij} between the two particles and d_{iB} between the particle and
 443 beam, with the measures defined as:

$$d_{ij} = \min(k_{ti}^{-2}, k_{tj}^{-2}) \frac{(\Delta R_{ij})^2}{R^2}, \quad (1)$$

$$d_{iB} = k_{ti}^{-2}, \quad (2)$$

444 where k_{ti} refers to the transverse momentum of particle i , ΔR_{ij} refers to the spatial distance
 445 (in rapidity and azimuth) between the two particles, and radius parameter R is a reconstruction
 446 parameter. The name anti- k_t derives from the negative exponent for k_t (in contrast to other
 447 sequential recombination algorithms), which enables IRC safety and soft resilience by making jet
 448 shape sensitivity to a particle inversely correlated to the particle's transverse momentum. With
 449 this low sensitivity to soft particles, the anti- k_t algorithm results in a collection of mostly circular
 450 jets (except in the case of jets separated by less than $2R$, in which each jet has a radius of πR^2).
 451 The choice of parameter R is a trade-off between capturing more fragmentation products (as can
 452 extend as far as $\Delta R_{ij} = 0.8$ in pp collisions), and limiting the influence of background particles
 453 in jet reconstruction. In heavy ion experimental studies, where background levels are very high,
 454 typical choices of R range from 0.2 to 0.5.

455 With the CMS detector, jets may be clustered from ECAL and HCAL information only
 456 (“calorimeter jets”) or from information from the full detector, using the particle flow (PF) algo-
 457 rithm. The PF algorithm improves jet energy resolution (JER) substantially at low- p_T (at 10 GeV
 458 JER is 15% for PF jets versus 40% for calorimeter jets) with improvements decreasing for higher- p_T
 459 jets (at 100 GeV PF jet JER is 8% versus 12% for calorimeter jets, falling to a difference of 4%
 460 versus 5% at 1 TeV). For jet-track correlation studies, however, the resolution improvements that
 461 the particle flow algorithm offers come at the cost of enhancing sensitivity to tracking biases in the
 462 jet-track correlation signal, since low- p_T tracks are included in jet reconstruction. In this analysis,
 463 calorimeter jets are used to avoid these auto-correlation effects, and because we will consider jets
 464 with $p_T > 120$ GeV for which calorimeter jet energy resolution is adequate. Jets are reconstructed
 465 with anti- k_t radius $R = 0.3$ for 2.76 TeV data (“ak3Calo” jets), and with radius $R = 0.4$ for 5.02
 466 TeV data (“ak4Calo” jets). In pp data at 2.76 TeV and 5.02 TeV the contribution to the jet energy
 467 from the underlying event (UE) is negligible (less than 1 GeV), so no underlying event subtraction
 468 is employed.

469 **5.2 Underlying event subtraction in PbPb data**

470 In PbPb collisions it is necessary to subtract contributions from the large underlying event in order
471 to recover the true jet energy. There are a variety of methods used for underlying event subtraction,
472 of which the following two are relevant for this analysis.

473 **5.2.1 Noise/pedestal subtraction**

474 In most CMS high- p_T jet analyses, including 5.02 TeV PbPb data studies here, underlying event
475 subtraction is performed using a variant of an iterative noise/pedestal subtraction technique [21].
476 This algorithm occurs in the following steps:

- 477 • First, the mean “pedestal” energy in calorimeter cells as a function of energy η ($P(\eta)$) is
478 calculated along with its dispersion.
- 479 • The pedestal function $P(\eta)$ is subtracted from all cells.
- 480 • Cells with non-physical negative energy entries are then set to zero.
- 481 • $\langle E_{\text{cell}} \rangle + \langle \sigma(E_{\text{cell}}) \rangle$ is subtracted from each cell to compensate for the elimination of negative
482 energy cells.
- 483 • Jets are clustered from the pedestal-subtracted cells using the anti- k_t algorithm.
- 484 • The pedestal function $P(\eta)$ is then re-derived using only cells that are not a part of clustered
485 jets, and the algorithm is repeated.

486 After this underlying event subtraction is applied, the anti- k_t algorithm with radius parameter
487 $R = 0.4$ is then employed for jet reconstruction (“akPu4Calo jets”).

488 **5.2.2 HF/Voronoi subtraction**

489 For 2.76 TeV PbPb data a different algorithm, designed to eliminate the threshold and possible
490 resulting bias from the noise/pedestal technique, is employed [15]. This algorithm uses information
491 from the HF detector to model and subtract the underlying event using Voronoi decomposition
492 (“HF/Voronoi” algorithm) in the following steps:

- The distribution of underlying E_T as a function of η and ϕ is modeled using singular value decomposition (SVD) training ($dE_T/d\eta/\phi$ with Voronoi parameters $v_1 \dots v_4$) to extrapolate the UE distribution from the HF calorimeter at large η to the central analysis region ($|\eta| < 1.6$).
- The modeled UE distribution is subtracted from all calorimeter cells.
- Each calorimeter cell is associated with its nearest neighbors, and energy is redistributed between neighboring in an “equalization” procedure used to eliminate non-physical negative E_T entries (optimized to minimize energy transfers).

After Voronoi subtraction and equalization, the anti- k_t algorithm is employed with radius parameter $R = 0.3$ to cluster (“akVs3Calo”) jets.

5.3 Jet energy corrections

Jet reconstruction as described above gives spatial coordinates and p_T for each jet as measured by the detector. Our goal in jet studies, however, is to reconstruct the true total parton or particle energy. This is achieved through jet energy corrections (JEC) that establish a mapping between measured energy (which does not, for example, include neutrinos produced in jet fragmentation) and “true” jet energies. This mapping is complicated by nonlinearity in detector response. Initial corrections are derived as a function of p_T and η using dijet QCD samples of PYTHIA and PYTHIA+HYDJET Monte Carlo, spatially matching reconstructed jets to generated particles, and comparing generated versus reconstructed jet energy for these matched jets. These “MC truth” corrections are applied to measured jet energies to return a collection of jets that, on average, capture the kinematic distribution of the partons before fragmentation.

These corrections do not, however, fully account for the non-linearity of calorimeter response. In particular, in an effect particularly relevant for jet-track correlation studies, the jet energy scale depends on jet fragmentation. Given two jets with identical parton energy, the jet with softer fragmentation (i.e. jets with a higher fraction low- p_T particles) will be on average reconstructed with lower energy than the jet with harder fragmentation. When combined with a jet selection threshold, this non-linearity results in a bias that systematically underestimates the jets with soft fragmentation in the analysis sample. An additional fragmentation-function dependent jet energy correction (JFF-JEC) is therefore applied after initial jet energy corrections in order to

521 reduce this bias (detailed in Ref. [15]). These JFF-JEC are derived using the number of particle flow
 522 candidates (N_{PF}) in the jet with $p_T > 2$ GeV, with this threshold chosen to reduce the influence
 523 of soft fluctuations in the underlying event. Correction tables are derived as a function of N_{PF} , jet
 524 p_T , and PbPb event centrality in PYTHIA and PYTHIA+HYDJET simulation, and are applied to jets
 525 after the JECs described above. Finally, iterative residual corrections are applied as a function of
 526 jet p_T . The application of JFF-JECs reduces the overall quark/gluon non-closure, as illustrated for
 527 PbPb data in Fig. 5, and slightly improves jet energy resolution overall.

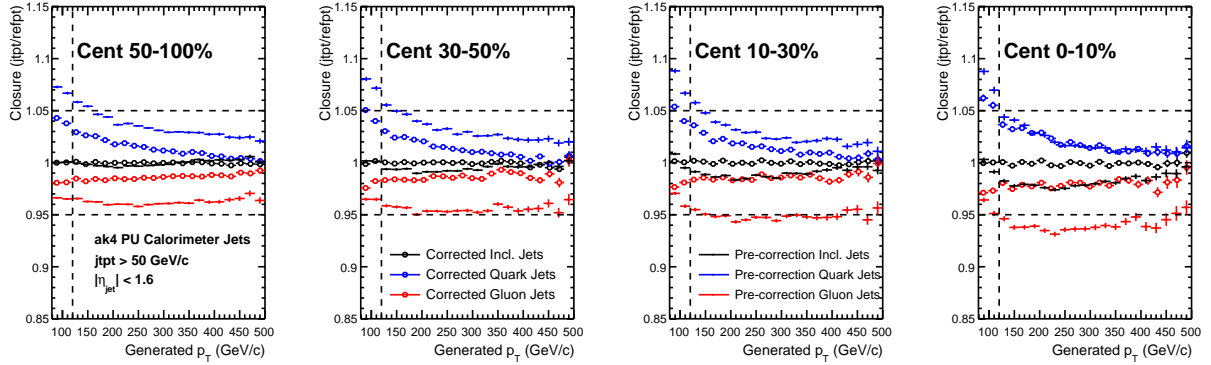


Figure 5. Closure with and without JFF-JEC for quark and gluon jets.

6 DATA AND MONTE CARLO SAMPLES

529 6.1 Data samples and event selection

530 This analysis is based on PbPb and pp data collected with the CMS detector at 2.76 TeV and 5.02
 531 TeV during Run 1 and Run 2 of the CERN LHC. Studies at 2.76 TeV use $166 \mu\text{b}^{-1}$ of PbPb data
 532 collected in 2011, and 5.3 pb^{-1} of pp data collected in 2013. Studies at 5.02 TeV use $404 \mu\text{b}^{-1}$ of
 533 PbPb data and 25 pb^{-1} of pp data, both collected in 2015. Online collision selection was performed
 534 using the CMS HLT described in Sec. 3.5 to obtain a minimum bias sample of PbPb collision events,
 535 and to obtain samples of PbPb and pp data with the requirement that events contain at least one
 536 high- p_{T} jet (with $p_{\text{T}} > 80 \text{ GeV}$ for pp data and 2.76 TeV PbPb data, $p_{\text{T}} > 100 \text{ GeV}$ for 5.02 TeV
 537 PbPb data). These jet triggers are fully efficient for offline-reconstructed jets with $p_{\text{T}} > 120 \text{ GeV}$.
 538 Total numbers of selected events are summarized in Table I.

TABLE I. Summary of data samples and number of selected events

Dataset	Number of selected events
2.76 TeV PbPb MinimumBias	1.01 M
2.76 TeV PbPb Jet-triggered ($p_{\text{T}} > 80 \text{ GeV}$)	1.25 M
2.76 TeV pp Jet-triggered ($p_{\text{T}} > 80 \text{ GeV}$)	1.27 M
5.02 TeV PbPb MinimumBias	764 k
5.02 TeV PbPb Jet-triggered ($p_{\text{T}} > 100 \text{ GeV}$)	3.35 M
5.02 TeV pp Jet-triggered ($p_{\text{T}} > 80 \text{ GeV}$)	2.66 M

539 A number of quality cuts are applied, as is standard for CMS analyses to remove detector
 540 noise backgrounds, ultra-peripheral collisions, beam gas, and events with exceptionally large pixel
 541 occupancy. These selection criteria have shown to have negligible impact on dijet analyses [11, 10],
 542 and are as follows in PbPb and pp collisions:

- 543 • Vertex-z position within 15 cm of the center of the detector ($|v_z| < 15$)

- 544 • Primary vertex filter – a requirement that events include a reconstructed primary vertex filter
 545 with at least two tracks, requiring the presence of inelastic hadronic scattering and removing
 546 beam-gas events and ultra-peripheral collisions
- 547 • Beam-scraping filter – a requirement of pixel clusters compatible with the primary vertex.
 548 In pp, this requires that if there are more than 10 tracks, at least 25% of tracks must be
 549 highPurity (see Sec. 4)
- 550 • HB/HE noise filter – a filter to exclude events exhibiting uncharacteristic calorimeter noise [14]
- 551 • PbPb data only: HF coincidence filter – at least 3 GeV recorded in at least each of at least
 552 three hadronic forward calorimeter towers on each side of the interaction point
- 553 These cleaning cuts are applied to both minimum bias and jet-triggered data samples. Additional
 554 event selection will later be applied to obtain samples of high- p_T jets and dijet events, as discussed
 555 in Sec. 6.4 below.

556 **6.2 Collision centrality determination and classes**

557 The variable centrality is used to parameterize the degree of overlap of the colliding nuclei. In
 558 CMS, centrality is determined using total transverse energy (E_T) in the HF calorimeter towers, in
 559 the region $4.0 < |\eta| < 5.2$. The distribution of total E_T in all events is used to divide the total
 560 minimum bias event sample into centrality bins, each containing 0.5% of the total events. The
 561 resulting centrality distribution is flat in minimum bias data by construction. In jet-triggered, data,
 562 however, requiring the presence of a high- p_T jet results in a larger fraction of more central collisions
 563 (in which hard-scatterings are more likely). The collisions defined as “most central” (centrality =
 564 0%) are those with the greatest E_T , corresponding to collisions in which the nuclei collided head-on.
 565 In contrast, the collisions defined as “least central” or “most peripheral” (centrality = 100%) are
 566 those in which the nuclei barely overlapped at all. To observe how jet modifications evolve with
 567 changing centrality, this analysis considers four centrality classes: 0-10% (most central), 10-30%,
 568 30-50%, and 50-100%.

569 **6.3 Monte Carlo simulation**

570 Monte Carlo (MC) simulation is used in this analysis to evaluate and correct for jet reconstruction
571 performance and tracking efficiency for both pp and PbPb data. Simulation of pp data and of
572 the hard processes in PbPb data are performed using the PYTHIA (version 6, tune Z2 [24]) event
573 generator. In order to have reasonable event samples in all jet p_T ranges, different samples are
574 produced with various cut-off values of \hat{p}_T , which are then combined using their respective cross-
575 sections as weights. To simulate CMS detector output for MC events, GEANT4 detector simulation
576 is used [2]. Jet and track reconstruction performance and efficiency for pp data is evaluated by
577 comparing observables in PYTHIA samples as generated to the same observables after they have
578 been passed through the detector simulation and the same reconstruction procedures applied to
579 pp data. For the relevant jet kinematics observables relevant to this analysis, PYTHIA reasonably
580 reproduces pp data.

581 For PbPb data, the underlying event is simulated using HYDJET (Drum5 tune) [22], which
582 combines hydrodynamics with “mini-jets” produced with quenched pythia input. Hard processes
583 are generated using PYTHIA, and are directly embedded in this HYDJET sample (refered to as
584 PYTHIA+HYDJET simulation), with no medium quenching effects applied to the embedded jets.
585 This PYTHIA+HYDJET sample is used to evaluate the reconstruction effects of the presence of
586 the QGP medium, *other* than the jet-medium interactions that are our objects of study. As for
587 PYTHIA simulation of pp data, comparing PYTHIA+HYDJET samples that have been passed through
588 the detector and reconstructed chain to the generated Monte Carlo allows for the evaluation of jet
589 and track reconstruction performance.

590 **6.3.1 Monte Carlo centrality and vertex-z reweighting**

591 Simulated PYTHIA+HYDJET samples are generated minimum bias, and therefore must be reweighted
592 to match the bias toward more central events induced by requiring the presence of a high- p_T
593 jets discussed in Sec. 6.2. Reweighting factors are calculated for each 0.5%-wide centrality bin,
594 and applied to the PYTHIA+HYDJET sample overall to match the PbPb centrality distribution.
595 Similarly, another reweighting procedure is performed to match the distributions of the position of

596 the primary interaction along the beam direction in MC and data for both pp and PbPb collisions.
 597 Figures 6–8 illustrate the necessity and effects of these reweighting procedures.

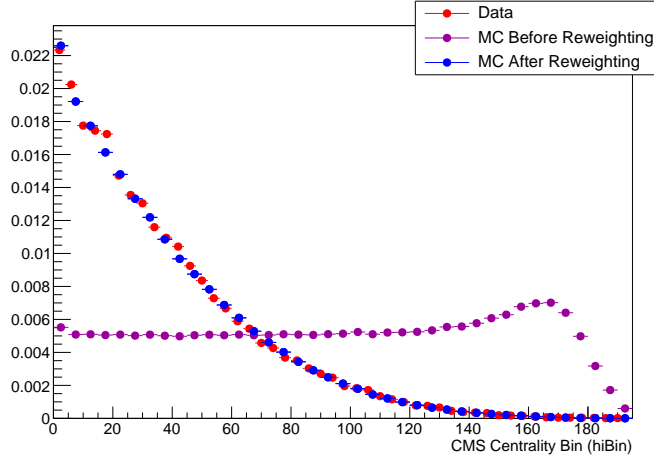


Figure 6. Centrality distribution for PYTHIA+HYDJET reweighted to match centrality distribution of PbPb data.

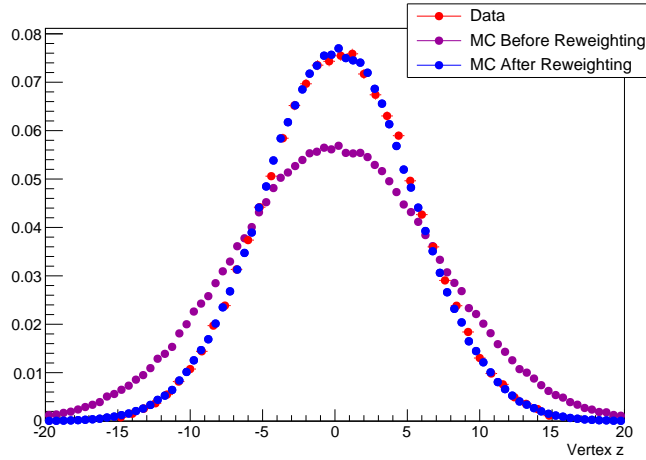


Figure 7. Vertex z distribution for PYTHIA+HYDJET reweighted to match centrality distribution of PbPb data.

598 6.3.2 Monte Carlo samples at 2.76 TeV

599 Tables II and III summarize the PYTHIA and PYTHIA+HYDJET samples used in this analysis by \hat{p}_T ,
 600 with respective numbers of generated events and cross-sections used for combining samples.

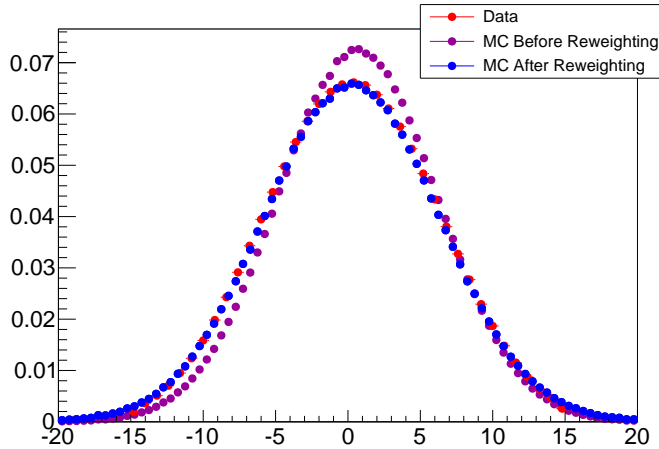


Figure 8. Vertex z distribution for PYTHIA reweighted to match centrality distribution of pp data.

TABLE II. Summary of Monte Carlo samples and generated events at 2.76 TeV

Generator	Process	Cross section (mb)	Number of events
PYTHIA+HYDJET	$\hat{p}_T > 50 \text{ GeV}$	1.025×10^{-3}	395k
PYTHIA+HYDJET	$\hat{p}_T > 80 \text{ GeV}$	9.865×10^{-5}	368k
PYTHIA+HYDJET	$\hat{p}_T > 120 \text{ GeV}$	1.129×10^{-5}	367k
PYTHIA+HYDJET	$\hat{p}_T > 170 \text{ GeV}$	1.465×10^{-6}	392k
PYTHIA+HYDJET	$\hat{p}_T > 220 \text{ GeV}$	2.837×10^{-7}	181k
PYTHIA+HYDJET	$\hat{p}_T > 280 \text{ GeV}$	2.837×10^{-7}	50k
PYTHIA	$\hat{p}_T > 80 \text{ GeV}$	9.865×10^{-5}	104k
PYTHIA	$\hat{p}_T > 120 \text{ GeV}$	1.129×10^{-5}	975k
PYTHIA	$\hat{p}_T > 170 \text{ GeV}$	1.465×10^{-6}	69k

601 **6.3.3 Summary of Monte Carlo samples at 5.02 TeV**

TABLE III. Summary of Monte Carlo samples and generated events at 5.02 TeV

Generator	Process	Cross section (mb)	Number of events
PYTHIA+HYDJET	$\hat{p}_T > 80 \text{ GeV}/c$	4.412×10^{-4}	499k
PYTHIA+HYDJET	$\hat{p}_T > 120 \text{ GeV}/c$	6.147×10^{-5}	496k
PYTHIA+HYDJET	$\hat{p}_T > 170 \text{ GeV}/c$	1.018×10^{-5}	498k
PYTHIA+HYDJET	$\hat{p}_T > 220 \text{ GeV}/c$	2.477×10^{-6}	200k
PYTHIA+HYDJET	$\hat{p}_T > 280 \text{ GeV}/c$	6.160×10^{-7}	200k
<hr/>			
PYTHIA	$\hat{p}_T > 80 \text{ GeV}/c$	4.412×10^{-4}	500k
PYTHIA	$\hat{p}_T > 120 \text{ GeV}/c$	6.147×10^{-5}	500k
PYTHIA	$\hat{p}_T > 170 \text{ GeV}/c$	1.018×10^{-5}	499k
PYTHIA	$\hat{p}_T > 220 \text{ GeV}/c$	2.477×10^{-6}	200k
PYTHIA	$\hat{p}_T > 280 \text{ GeV}/c$	6.160×10^{-7}	200k

602 **6.4 Jet selection and dijet asymmetry classes**

603 Jet selection in this analysis is restricted to the pseudorapidity region $|\eta_{\text{jet}}| < 1.6$ to ensure stable
604 reconstruction performance in the calorimeter barrel region. A requirement is also imposed that
605 the highest- p_T track contains no less than 1% and no more than 98% of the total jet p_T . In the
606 jet selection referred to as “inclusive jets” for analysis at both 2.76 TeV and 5.02 TeV, all jets with
607 $p_{T,\text{jet}} > 120$ GeV are considered. In this selection, it is possible to select more than one jet from
608 the same event, provided that each jet satisfies the inclusive selection criteria.

609 In addition to the inclusive jet selection, a “dijet” selection of events containing two back-to-
610 back high- p_T jets is also analyzed for the 2.76 TeV data sample. Events are included in this sample
611 based on the criteria that they contain highest- p_T “leading” jet with $p_{T,1} > 120$ GeV and a second-
612 highest- p_T “subleading” jet with $p_{T,2} > 50$ GeV with relative azimuthal separation $\Delta\phi > \frac{5\pi}{6}$. This
613 dijet sample is subdivided into a sample of relatively “balanced” dijets, with similar $p_{T,1}$ and $p_{T,2}$
614 and a sample of relatively “unbalanced” dijets in which the leading jet has a much larger p_T than
615 the subleading jet based on asymmetry parameter A_J :

$$A_J = \frac{p_{T,1} - p_{T,2}}{p_{T,1} + p_{T,2}} \quad (3)$$

616 The balanced’ selection is defined as those events for which $A_J < 0.22$, while the unbalanced
617 selection as defined as those events for which $A_J > 0.22$. The dividing value $A_J = 0.22$ is chosen
618 for consistency with previous CMS analyses [7, 19]. In this analysis, 52% of central PbPb events
619 are balanced, while 67% of pp events are balanced. Jet kinematics for all jet samples (broken
620 down by asymmetry for 2.76 TeV dijet data) are shown in Appendix A.1 for 2.76 TeV data and in
621 Appendix A.2 for 5.02 TeV data.

622 **6.5 Track selection and classes**

623 Tracks, reconstructed as described in Sec. 4 are required to satisfy the following criteria:

- 624 • $|\eta_{\text{trk}}| < 2.4$ – restricts to the barrel region of the tracker
- 625 • $0.5 < p_{T}^{\text{trk}} < 300$ GeV – excludes very low- p_T tracks where reconstruction performance is not
626 stable

- 627 • High Purity criteria – see Sec. 4.3
- 628 • Distance of closest approach (DCA) in x-y plane and in z less than 3 times the DCA error –
629 reduces fraction of tracks not associated with a primary vertex
- 630 • Relative p_T^{trk} error less than 30% (10% for 5.02 TeV PbPb data) – removes tracks with very
631 poor resolution (has a negligible effect on efficiency as CMS resolution is generally good)
- 632 For 5.02 TeV PbPb data, the following additional criteria are also applied to reduce the contribution
633 from misidentified tracks [17]:
- 634 • Exclude tracks with fewer than 11 tracker hits
- 635 • Require that for each track the chi-squared over number of degrees of freedom (χ^2 / Ndof) of
636 the track fit, also divided by the number of tracker layers (nLayer) hit as the track passed
637 through the detector, is less than 0.15, i.e. $\chi^2 / \text{Ndof} / \text{nLayer} < 0.15$.
- 638 • For tracks with $p_T > 20$ GeV (the kinematic region in which misreconstruction is difficult to
639 access with Monte Carlo), calorimeter matching is applied: since high- p_T tracks eventually
640 deposit their energy in a calorimeter after passing through the tracker, tracks are required
641 to be associated with calorimeter transverse energy $E_T = (E_{\text{ECAL}} + E_{\text{HCAL}}) / \cosh(\eta_{\text{trk}})$, such
642 that $E_T > 0.5p_T^{\text{trk}}$
- 643 After these selection criteria are applied, tracking efficiency corrections are applied as described
644 in Sec. 4.4. Tracks in this analysis are considered in the following classes: 0.5–1 GeV, 1–2 GeV,
645 2–3 GeV, 3–4 GeV, 4–8 GeV, 8–12 GeV, 12–16 GeV, 16–20 GeV, and above 20 GeV. Not all bins
646 are considered in every analysis, and for 5.02 TeV studies the lowest- p_T^{trk} bin is 0.7–1 GeV.

647 **6.6 Summary of analysis bins**

648 Table IV summarizes the key kinematic selections and bins for the three components to this analysis.

649 In all cases, identical selection is applied to PbPb and pp data. Event, jet, and track quality cuts

650 are not included in this table.

TABLE IV. Summary of data selections and analysis bins

Variable	2.76 TeV Inclusive	5.02 TeV Inclusive	2.76 TeV Dijets
PbPb Centrality	0-10%, 10-30%, 30-50%, 50-100%	0-10%, 10-30%, 30-50%, 50-100%	0-10%, 10-30%, 30-50%, 50-100%
Jet Selection	$ \eta_{\text{jet}} < 1.6$ $p_T > 120 \text{ GeV}$	$ \eta_{\text{jet}} < 1.6$ $p_T > 120 \text{ GeV}$	$ \eta_{\text{jet}} < 1.6$ $p_{T,1} > 120 \text{ GeV}$ $p_{T,2} > 50 \text{ GeV}$ $\Delta\phi_{1,2} > \frac{5\pi}{6}$
A_J Bins	–	–	$A_J < 0.22$, $A_J > 0.22$
Track η	$ \eta_{\text{trk}} < 2.4$	$ \eta_{\text{trk}} < 2.4$	$ \eta_{\text{trk}} < 2.4$
p_T^{trk} Bins	1-2 GeV, 2-3 GeV, 3-4 GeV, 4-8 GeV	0.7-1 GeV, 1-2 GeV, 2-3 GeV, 3-4 GeV, 4-8 GeV	0.5-1 GeV, 1-2 GeV, 2-3 GeV, 3-4 GeV, 4-8 GeV, 8-300 GeV

651

7 JET-TRACK CORRELATION MEASUREMENTS

652

7.1 Analysis procedure

653 Measurements in this analysis are carried out by considering correlations between high- p_T jets and
 654 tracks in PbPb and pp collisions. Jets are selected within $\eta < 1.6$ and p_T above a particular
 655 threshold. For each jet, the relative separation in pseudorapidity ($\Delta\eta = \eta_{\text{track}} - \eta_{\text{jet}}$) and azimuth
 656 ($\Delta\phi = \phi_{\text{track}} - \phi_{\text{jet}}$) is measured between the jet and all charged-hadron tracks within $\eta < 2.4$. For
 657 each jet-track pair, these measurements are recorded in a two-dimensional $\Delta\eta - \Delta\phi$ correlation in
 658 a particular track transverse momentum (p_T^{trk}) and centrality class. Each correlation is normalized
 659 by dividing by the number of jets in the sample (N_{jets}), resulting in a signal pair distribution,
 660 $S(\Delta\eta, \Delta\phi)$, that gives the per-jet yield of tracks and their relative distance from the jet:

$$661 S(\Delta\eta, \Delta\phi) = \frac{1}{N_{\text{jets}}} \frac{d^2N^{\text{same}}}{d\Delta\eta d\Delta\phi}. \quad (4)$$

662 This procedure results in a two dimensional measurement of the distribution of charged
 663 tracks with respect to the jet axis. The same procedure may also be repeated, weighting each track
 664 by its p_T^{trk} , in order to obtain a distribution of p_T^{trk} with respect to the jet axis. These particle
 665 density and p_T^{trk} correlations form the basis for all results discussed in this analysis. From this
 666 point, several additional corrections and other steps are necessary to isolate jet-related effects from
 long range and uncorrelated backgrounds. These additional steps are as follows:

- 667 • A correction for jet-track pair acceptance events;
- 668 • Separation of correlations into short-range jet peaks and and long range components;
- 669 • Monte Carlo-based corrections for biases related to jet reconstruction.

670 After these steps, a range of different observables may be extracted to characterize the multiplicity
 671 and distribution of tracks and p_T^{trk} at both small and large angles from the jet axis.

672 **7.2 Jet-track correlation pair-acceptance correction**

673 This analysis considers $\Delta\eta$ jet-track separations as large as $\Delta\eta = 2.5$. With finite η acceptance for
 674 both jets and tracks ($\eta_{\text{jet}} < 1.6$ and $\eta_{\text{track}} < 2.4$, tracks that fall within $\Delta\eta = 2.5$ of a jet may be
 675 outside the tracking acceptance. This pair acceptance effect results in trapezoidal correlations that
 676 fall with rising $|\Delta\eta|$ as tracks are “lost” outside of the acceptance. This effect is purely geometric,
 677 and may be corrected by reproducing this pair acceptance geometry. This is done by creating a
 678 “mixed event” correlation in which jets in the sample are correlated to tracks within $\eta < 2.4$ from
 679 randomly selected events in a minimum bias PbPb sample, matched in vertex- z position (within 0.5
 680 cm) and centrality (within 2.5%). This reproduces the pair acceptance geometry from the signal
 681 correlations:

$$ME(\Delta\eta, \Delta\phi) = \frac{1}{N_{\text{jets}}} \frac{d^2N^{\text{mix}}}{d\Delta\eta d\Delta\phi}, \quad (5)$$

682 is constructed to account for pair-acceptance effects, with N^{mix} denoting the number of mixed-
 683 event jet-track pairs. Dividing the signal correlation $S(\Delta\eta, \Delta\phi)$, defined in Equation 4, by this
 684 mixed event correlation $ME(\Delta\eta, \Delta\phi)$ yields the corrected per-jet correlated yield distribution, as
 685 illustrated in Figure 9:

$$\frac{1}{N_{\text{jets}}} \frac{d^2N}{d\Delta\eta d\Delta\phi} = \frac{ME(0, 0)}{ME(\Delta\eta, \Delta\phi)} \times S(\Delta\eta, \Delta\phi). \quad (6)$$

686 **7.3 Separation of correlations into long range and short-range components**

687 After correlations are corrected for pair-acceptance effects, in each correlation we are left with a
 688 well-defined jet peak sitting at $\Delta\eta = 0$, $\Delta\phi = 0$ on top of a large combinatoric and long range
 689 correlated background. For most measurements, it is necessary to isolate this jet peak in order to
 690 distinguish jet-related effects from eventwise correlations. In order to achieve this, we note that
 691 the long range correlation is independent of $\Delta\eta$ at distances larger than $\Delta\eta = 1.5$ from the jet.
 692 This “sideband” region ($1.5 < |\Delta\eta| < 3.0$) is used to model the underlying event, capturing both
 693 the level of the combinatoric background in the event, and also the long range “flow” correlations
 694 in the event. The assumption of rapidity-independence of the flow harmonics is based on the

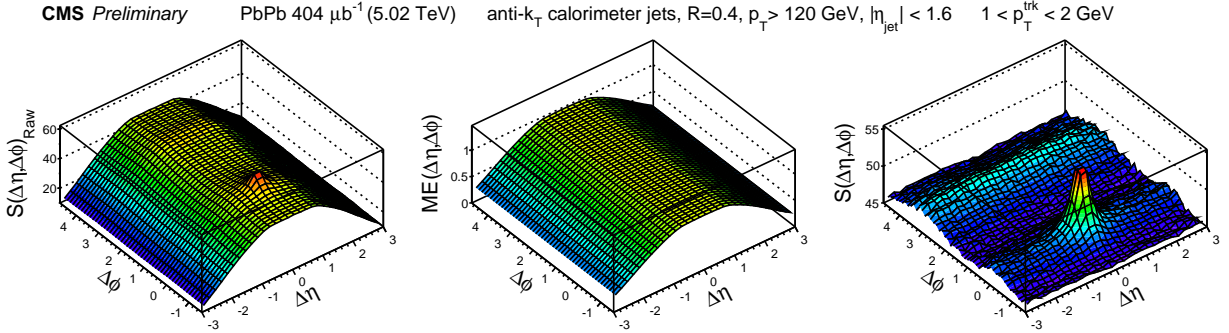


Figure 9. Illustration of the pair-acceptance correction procedure: left panel shows signal correlation $S(\Delta\eta, \Delta\phi)$, and center panel shows mixed event correlation $ME(\Delta\eta, \Delta\phi)$. Dividing the signal correlation by the mixed event correlation yields the corrected per-jet correlated yield distribution shown in the right panel.

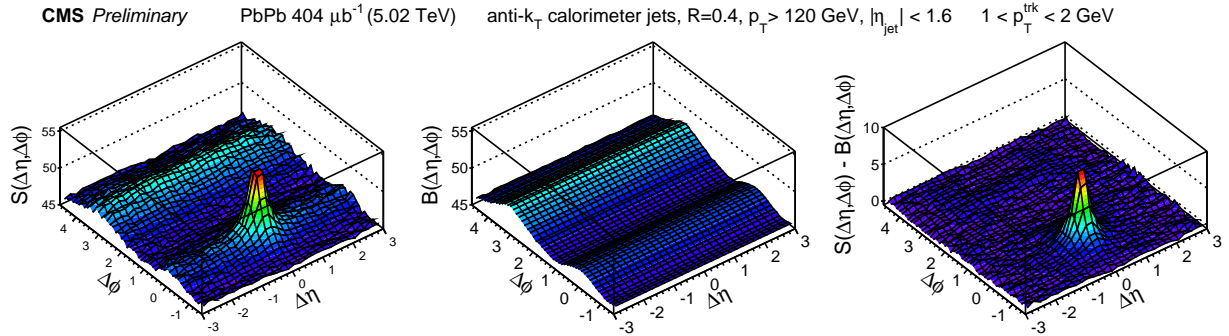


Figure 10. Illustration of the event decomposition procedure without $\Delta\phi$ fitting: left panel shows the acceptance-corrected correlation, middle panel shows the projected and re-propagated long range distribution, and right panel shows the background-subtracted jet peak.

695 CMS study [8], which shows no appreciable variation of the elliptic flow for charged particles above
 696 1 GeV in the pseudorapidity interval of $\Delta\eta < 3.0$ relevant for this study. As long range correlations
 697 depend only on $\Delta\phi$, the sideband region is projected into $\Delta\phi$ to obtain a one-dimensional model of
 698 the underlying event. To subtract this long range correlation in 2D, this distribution may be either
 699 directly re-propagated into $\Delta\phi$ (as shown in Figure 10), or may be fit in $\Delta\phi$ before repropagation
 700 in a smoothing procedure as shown in Fig. 11.

701 The long range correlations in this distribution are in themselves interesting objects of study,
 702 as these contain information about the collective behavior of particles in the event as a whole, and

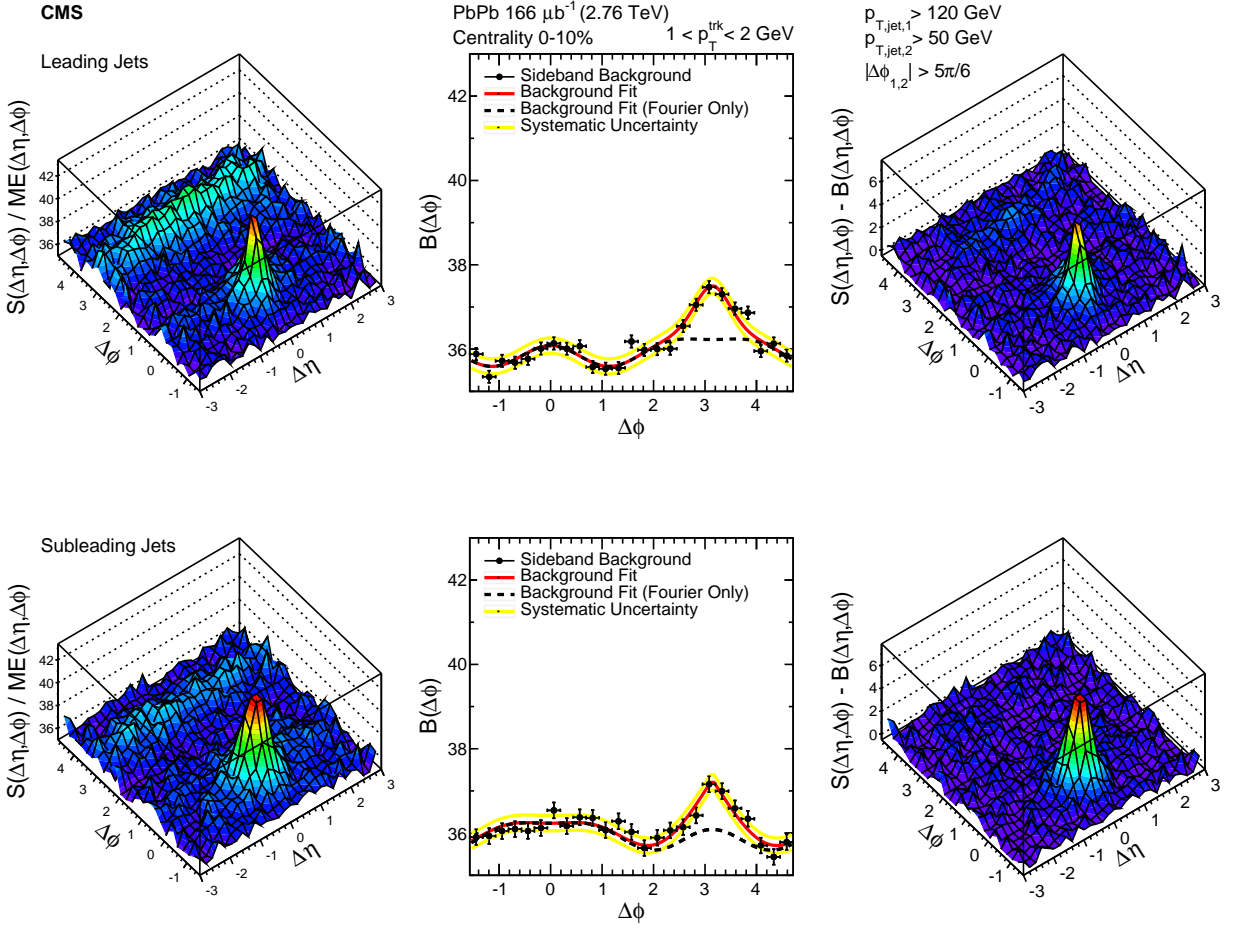


Figure 11. Illustration of the event decomposition procedure with $\Delta\phi$ fitting: left panel shows the acceptance-corrected correlation, middle panel shows the projected and fit long range distribution, and right panel shows the background-subtracted jet peak.

the extent to which the distribution of high- p_T jets in the event couples to this collective flow. To achieve this, we may apply the well-established method used to study two-particle correlations [9] to correlations between jets and tracks. In correlations to high- p_T jets, however, there is the additional kinematically required contribution to the correlation from the “away-side” peak opposite the jet at $\Delta\phi = \pi$). We therefore fit long range correlations function modeling harmonic flow plus a term to capture the (Gaussian or sharper) peak opposite the jet in relative azimuth:

$$B(\Delta\phi) = B_0(1 + 2V_1 \cos(\Delta\phi) + 2V_2 \cos(2\Delta\phi) + 2V_3 \cos(3\Delta\phi)) + A_{AS} \exp\left(-\left(\frac{|\Delta\phi - \pi|}{\alpha}\right)^\beta\right), \quad (7)$$

709 For dijet studies, two iterations of fit are performed for each centrality class. In the first
 710 iteration, we make use of the fact that for our dijet selection and a given value of $\Delta\eta$ the region
 711 $-\frac{\pi}{2} < \Delta\phi < \frac{\pi}{2}$ of the leading correlation is by definition equivalent to the region $\frac{\pi}{2} < \Delta\phi < 3\frac{\pi}{2}$ of
 712 the subleading correlation. We therefore perform a single fit to the combined background. Here we
 713 fit with harmonic flow terms only:

$$B(\Delta\phi)^{\text{Dijet}} = B_0(1 + 2V_1 \cos(\Delta\phi) + 2V_2 \cos(2\Delta\phi) + 2V_3 \cos(3\Delta\phi)), \quad (8)$$

714 In this fit, we find that terms through V_3 are necessary to describe the low- p_T , central
 715 background, while at higher- p_T only V_1 , V_2 . From this combined fit, we extract parameters V_1 ,
 716 V_2 , and V_3 . Then, to better constrain the background under the signal and minimize the effects
 717 of random background fluctuations, we apply the factorization relation of overall Fourier harmonic
 718 $V_2 = v_2^{\text{jet}} \times v_2^{\text{trk}}$ [1, 6]. The values of v_2^{trk} for charged particles are determined in Ref. [9], while
 719 the fit parameter v_2 is expected to be independent of p_T^{trk} ranges for a given centrality class. The
 720 average value of v_2^{jet} from each p_T^{trk} range is calculated, and used to fix the V_2 parameter on the
 721 second iteration of the fit. Both the combined dijet fit with $B(\Delta\phi)^{\text{Dijet}}$ and the final $B(\Delta\phi)$ fits are
 722 shown in Appendix B. Through this process, we characterize the underlying event and note that
 723 the distribution of jets as well as tracks couples to the flow modulation of the underlying event.
 724 This has immediate consequences for studies of momentum balance between leading and subleading
 725 hemispheres of the event: as there are non-zero contributions from odd harmonics to the long-range
 726 correlated backgrounds, we cannot expect flow cancellation when directly subtracting hemishpere
 727 p_T^{trk} distributions.

728 For jet peak studies the underlying event is a background to subtracted to isolate jet peaks.
 729 After this is done, either by direct subtraction or by subtracting the fit and re-propagated back-
 730 ground, we are left with isolated 2D jet peaks. Before extracting observables, we must carefully
 731 consider and correct for reconstruction biases affecting these correlated yields. Before correlations
 732 are constructed, both tracks and jets are corrected for detector efficiencies and other reconstruction
 733 effects, as discussed in detail in Sec. 4 and Sec. 5, respectively. There are two effects, however, in
 734 which jet biases are coupled to the multiplicity of low- p_T tracks, that must be corrected after corre-
 735 lations are constructed and jet peaks are isolated. In the first, although fragmentation-dependent

736 jet energy corrections are applied to reduce the bias toward selecting jets with harder fragmentation,
737 these corrections cannot take into count the softest particles and a residual correction is needed.
738 The second arises due to the bias toward selecting jets that sit on upward (soft) fluctuations in
739 the background resulting in excess low- p_T yields around the jet axis. Both effects are studied and
740 corrections obtained by carrying out the full analysis in Monte Carlo simulation.

741 7.4 Residual Jet Fragmentation Function correction

742 Jets with harder fragmentation are more likely to be successfully reconstructed than jets with softer
743 fragmentation, resulting in a bias toward the selection of jets with fewer associated tracks in both
744 pp and PbPb data for all track- p_T selections studied. This bias is partially by the jet fragmentation
745 function-dependent jet energy corrections described in Sec. 5. Following the method used in [19],
746 corrections are derived for this bias and for the related possible effect of "jet swapping" between
747 leading, subleading, and additional jets by comparing correlated per-trigger particle yields for all
748 reconstructed jets versus all generated jets. This correction is derived for each jet selection in
749 PYTHIA-only simulation, and also in PYTHIA embedded and reconstructed in a HYDJET underlying
750 event, excluding HYDJET tracks from the correction determination. As expected considering the
751 exclusion of HYDJET tracks, the correction is very similar for pure PYTHIA and for all centralities of
752 PYTHIA+HYDJET. For illustration, the derivation and magnitude of these corrections for inclusive
753 jets at 2.76 TeV are shown in Figs. 12–15.

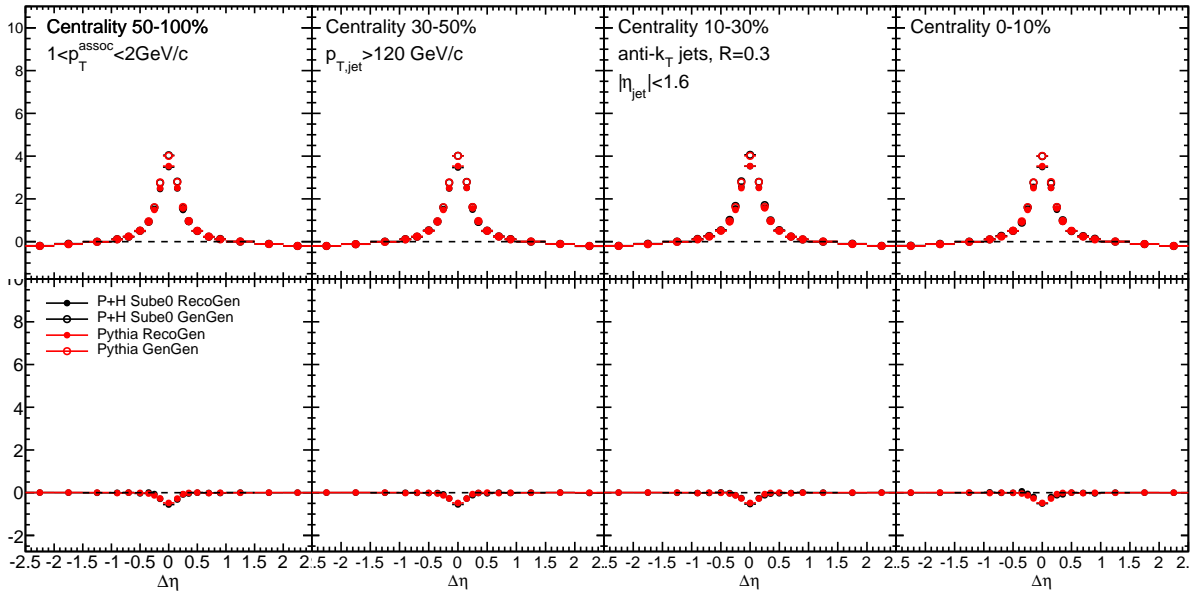


Figure 12. $\Delta\eta$ jet fragmentation function bias corrections derived by comparing correlations between reconstructed vs. generated jets and generated PYTHIA events, with and without embedding into the HYDJET heavy ion environment, for particles $1 < p_T^{\text{trk}} < 2 \text{ GeV}$.

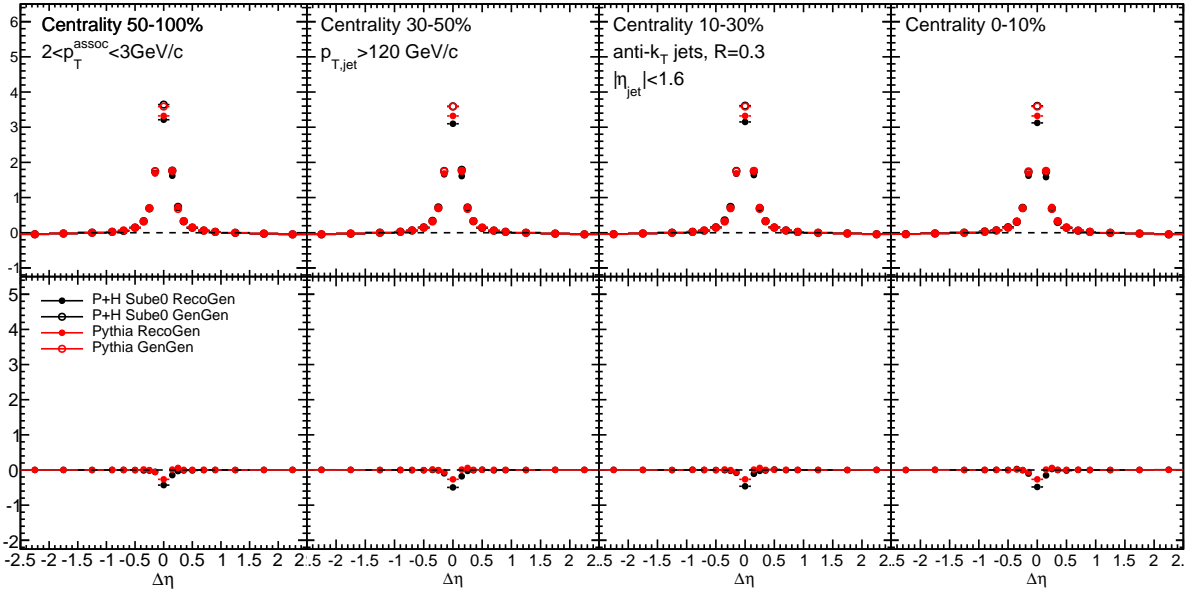


Figure 13. $\Delta\eta$ jet fragmentation function bias corrections derived by comparing correlations between reconstructed vs. generated jets and generated PYTHIA events, with and without embedding into the HYDJET heavy ion environment, for particles $2 < p_T^{\text{trk}} < 3 \text{ GeV}$.

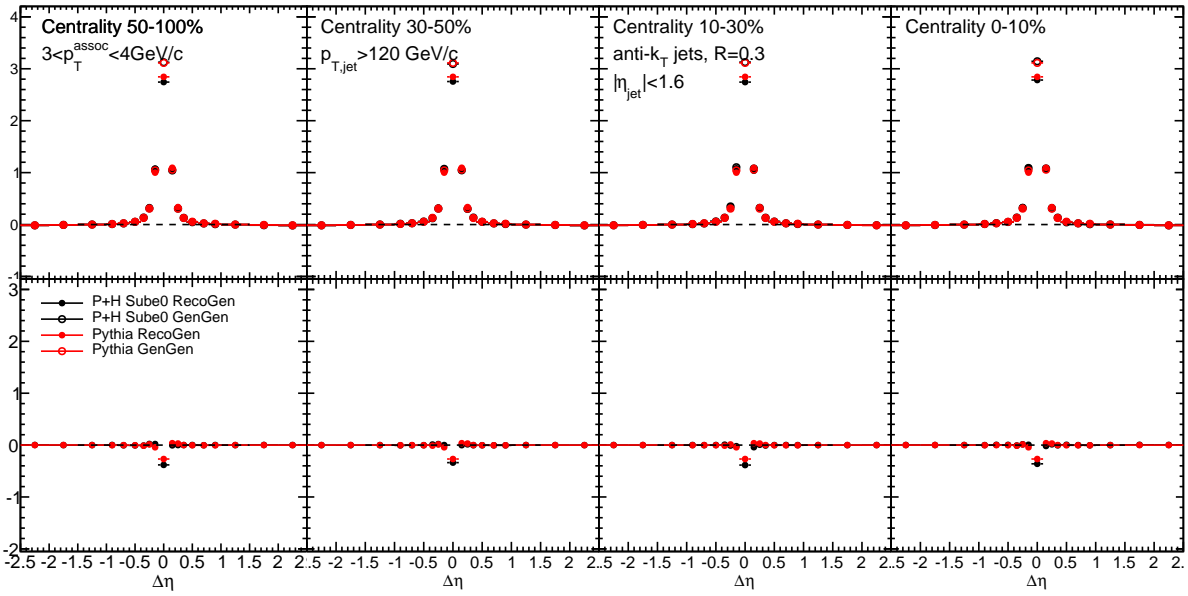


Figure 14. $\Delta\eta$ jet fragmentation function bias corrections derived by comparing correlations between reconstructed vs. generated jets and generated PYTHIA events, with and without embedding into the HYDJET heavy ion environment, for particles $3 < p_T^{\text{trk}} < 4 \text{ GeV}$.

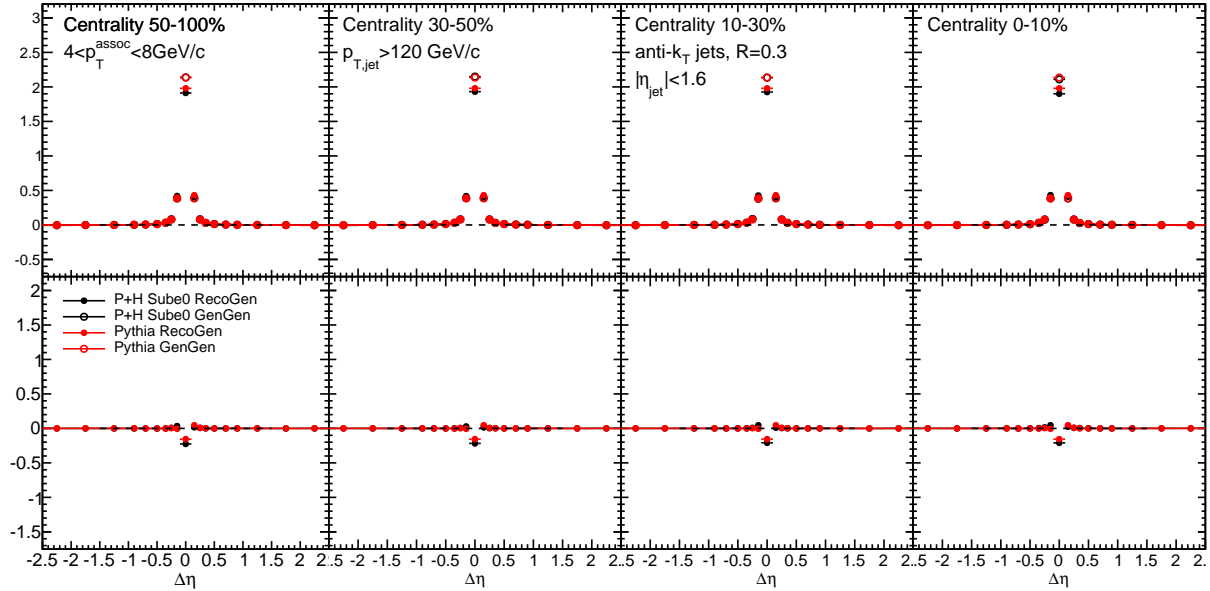


Figure 15. $\Delta\eta$ jet fragmentation function bias corrections derived by comparing correlations between reconstructed vs. generated jets and generated PYTHIA events, with and without embedding into the HYDJET heavy ion environment, for particles $4 < p_T^{\text{trk}} < 8 \text{ GeV}$.

To assess the overall effect of these corrections, the integrated yield of these corrections is shown as a function of transverse momentum and centrality is shown for inclusive, leading, and subleading jets as a function of p_T^{trk} in Fig. 16 and as a function of PbPb centrality in Fig. 17. The correction magnitude shows little centrality dependence, and is very similar for pure PYTHIA simulation and PYTHIA embedded into HYDJET.

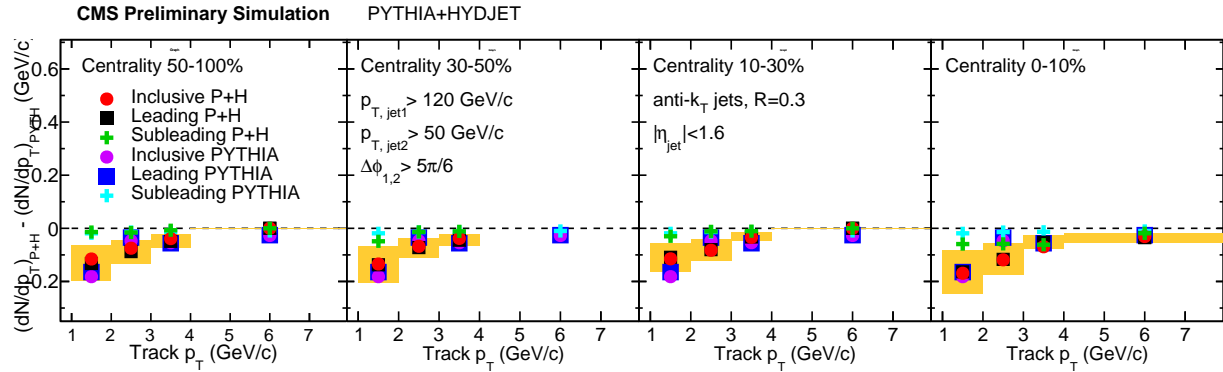


Figure 16. Integrated yield attributed to jet fragmentation function bias in jet reconstruction for PYTHIA alone and embedded into HYDDET, shown as a function of p_T^{trk} for each centrality class.

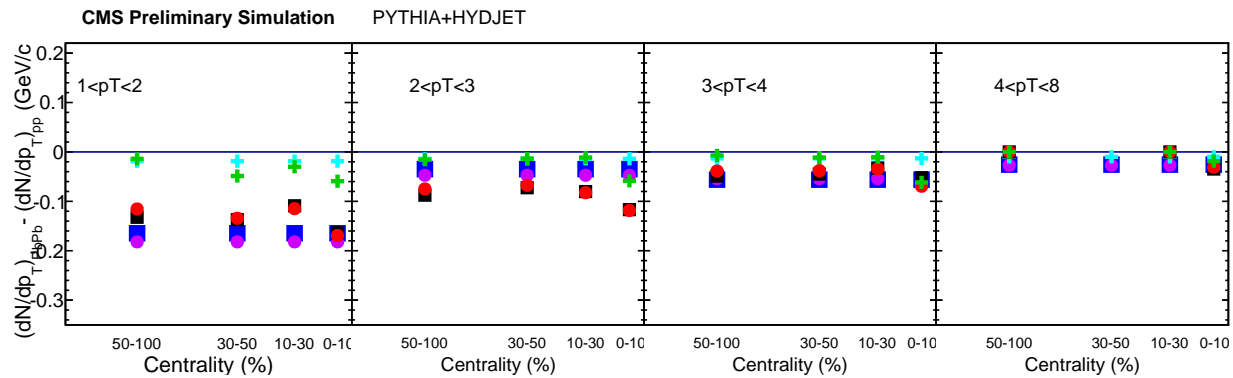


Figure 17. Integrated yield attributed to jet fragmentation function bias in jet reconstruction for PYTHIA alone and embedded into HYDDET, shown as a function of centrality for each associate track p_T range.

759 **7.5 Background fluctuation bias correction**

760 In central PbPb collisions background levels are very high, and naturally fluctuate throughout
761 the event. As discussed in Section 5, the process of jet reconstruction in PbPb collisions includes
762 background subtraction that accounts for the general distribution of energy in the event. However,
763 small, local variations in background levels remain (on the order of 5 GeV within a radius of $R =$
764 0.3). These are reconstructed into the jet, raising or lowering the measured jet energy depending
765 on whether the jet sits on an upward or a downward fluctuation in the background. As a result,
766 jets with “true” p_T slightly below the 120 GeV selection threshold that sit on upward background
767 fluctuations will be included in the sample, while jets sit on downward will be excluded. Because
768 the jet spectrum is steeply falling, it is much more common for a lower- p_T jet (on an upward
769 fluctuation) to be included in the sample than for a higher- p_T jet to be excluded. This results in
770 the systematic inclusion of tracks from background fluctuations in the peak of tracks observed about
771 the jet axis, resulting in a contribution to the initially measured jet peak that must be accurately
772 quantified and subtracted.

773 To estimate and subtract the contribution to the excess yield due to background fluctuation
774 bias in jet reconstruction to the measured excess yield, we perform simulations in PYTHIA+HYDJET
775 samples with reconstructed jets (but generated tracks, as the tracking efficiency uncertainty is
776 analyzed separately), and construct correlations excluding particles generated with the embedded
777 PYTHIA hard-scattering process. As the PYTHIA+HYDJET simulation does not include interactions
778 between the PYTHIA hard process and the medium, this procedure by construction isolates the
779 contribution to the jet peak that is attributable to the background fluctuation bias. The resulting
780 corrections are illustrated in Fig. 18 - Fig. 21 for inclusive jets at 2.76 TeV. These correlations show
781 a diminishing effect with increasing particle transverse momentum. We subtract the gaussian fit
782 to these correlations bin-by-bin from the data results, and also assign the half its magnitude as
783 systematic uncertainty to the final measurements. To assess the overall effect of these corrections,
784 the integrated yield of these corrections is shown in Fig. 22 as a function of transverse momentum
785 and centrality is shown for inclusive, leading, and subleading jets at 2.76 TeV.

786 Considering that the background fluctuation bias effect in many ways mimics the jet peak
787 signal, it is particularly important to validate this correction and confirm both that its origin

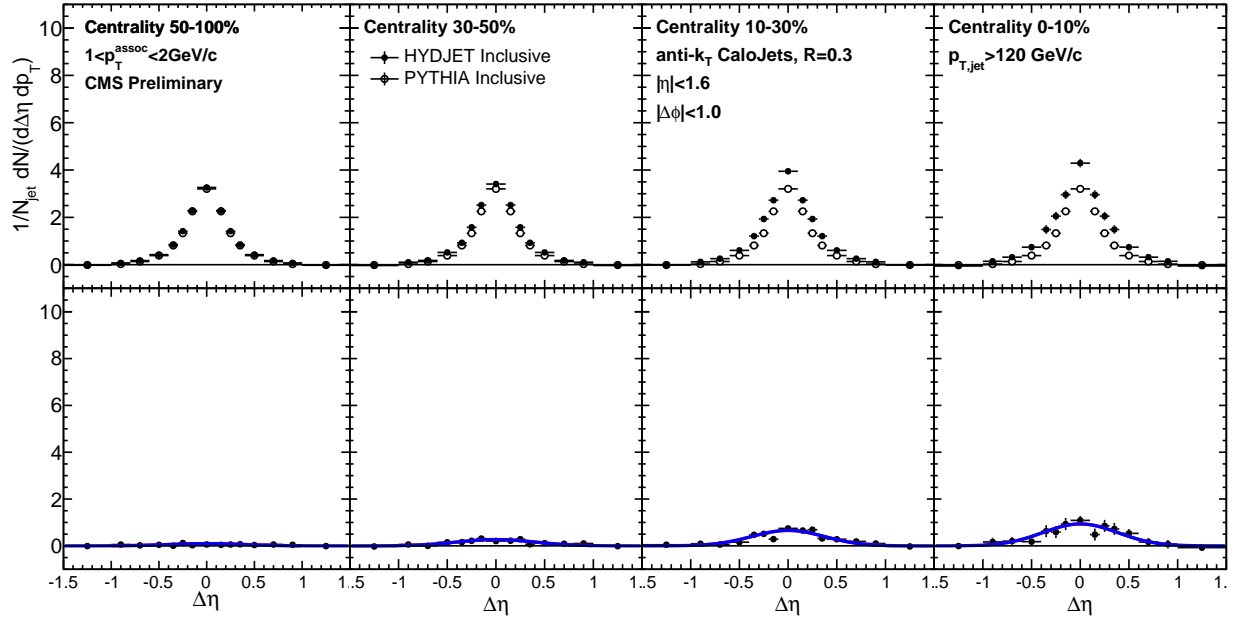


Figure 18. $\Delta\eta$ background fluctuation bias correction for inclusive jets derived by constructing correlations in PYTHIA+HYDJET between reconstructed jets and only those tracks simulated as part of the heavy ion underlying event rather than the embedded PYTHIA hard process, for particles $1 < p_T^{\text{trk}} < 2 \text{ GeV}$

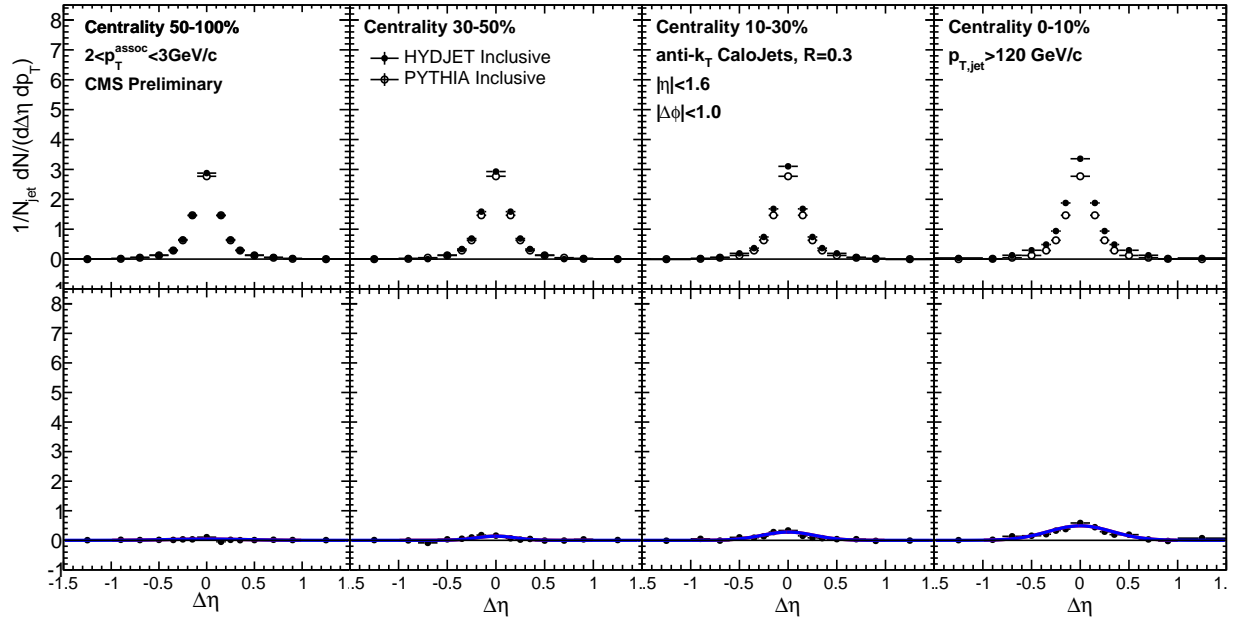


Figure 19. $\Delta\eta$ background fluctuation bias correction for inclusive jets derived by constructing correlations in PYTHIA+HYDJET between reconstructed jets and only those tracks simulated as part of the heavy ion underlying event rather than the embedded PYTHIA hard process, for particles $2 < p_T^{\text{trk}} < 3 \text{ GeV}$

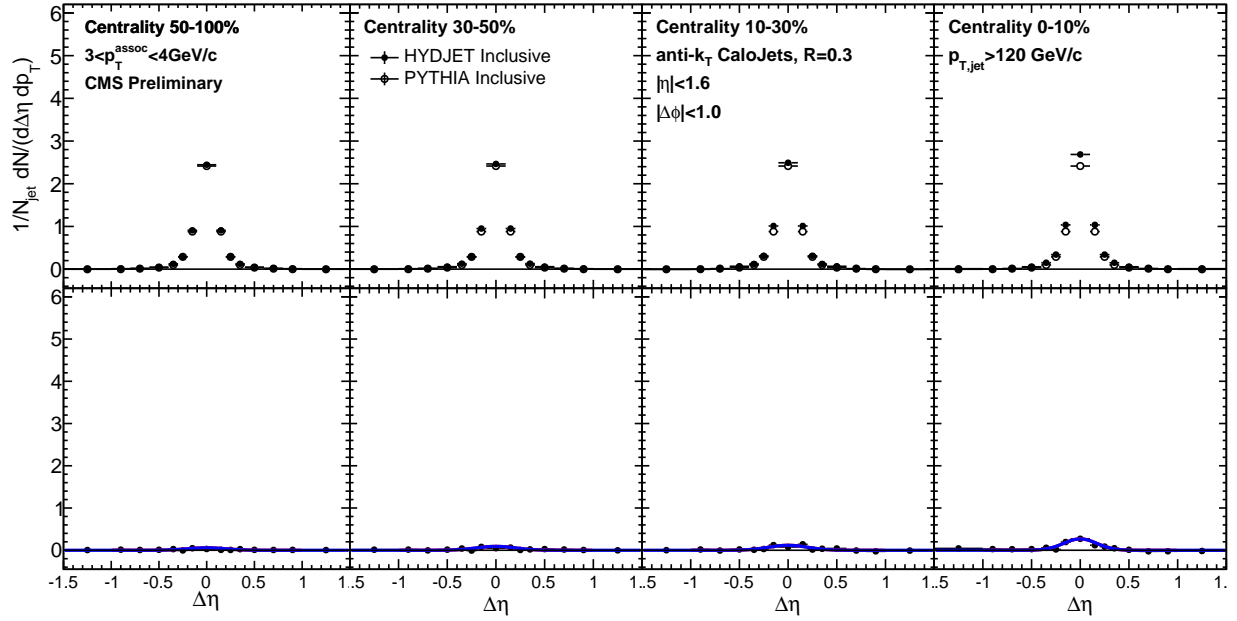


Figure 20. $\Delta\eta$ background fluctuation bias correction for inclusive jets derived by constructing correlations in PYTHIA+HYDJET between reconstructed jets and only those tracks simulated as part of the heavy ion underlying event rather than the embedded PYTHIA hard process, for particles $3 < p_T^{\text{trk}} < 4 \text{ GeV}$

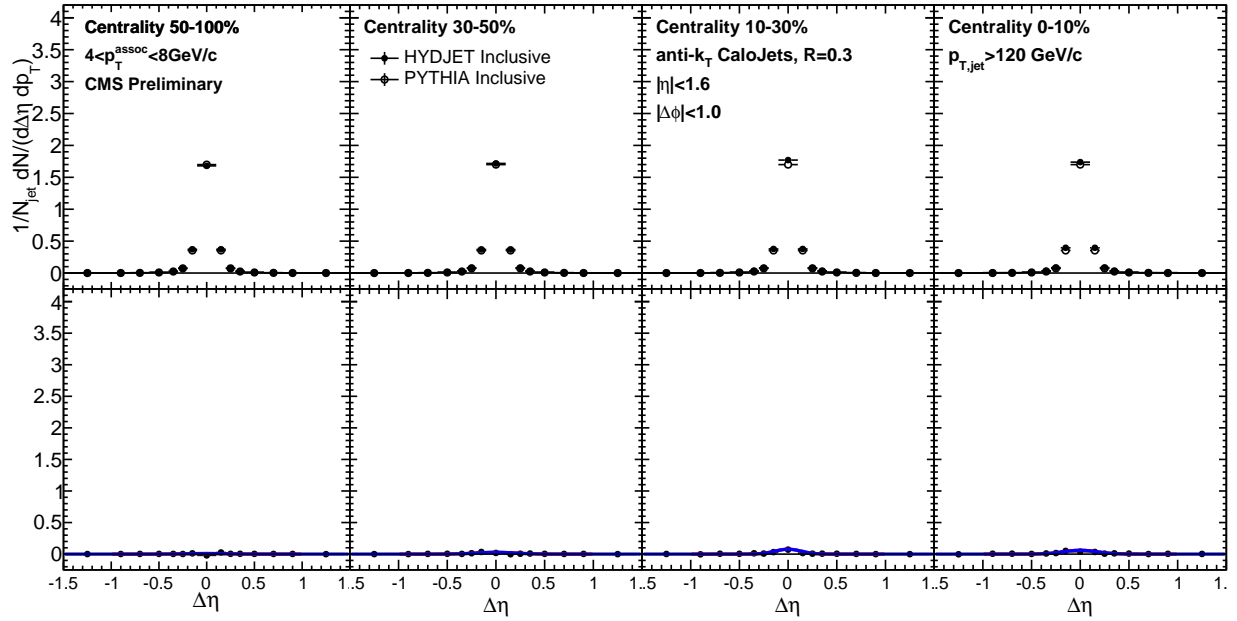


Figure 21. $\Delta\eta$ background fluctuation bias correction for inclusive jets derived by constructing correlations in PYTHIA+HYDJET between reconstructed jets and only those tracks simulated as part of the heavy ion underlying event rather than the embedded PYTHIA hard process, for particles $4 < p_T^{\text{trk}} < 8 \text{ GeV}$ and $p_{T,\text{jet}} > 120 \text{ GeV}/c$

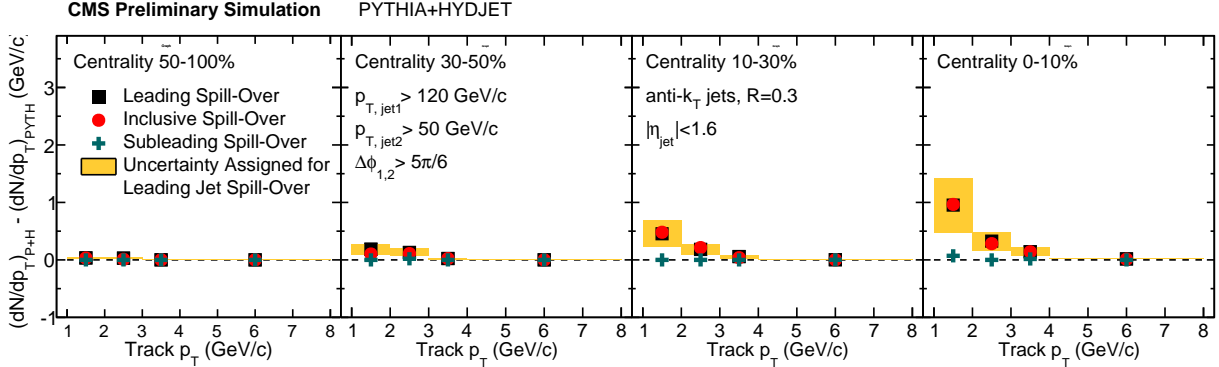


Figure 22. Integrated yield attributed to background fluctuation bias in the selection of inclusive and leading jets, shown as a function of associate track p_T for each centrality class.

is well-understood and that the HYDJET simulation used to derive it reproduces the background fluctuations in data closely enough to accurately obtain corrections. To check this, we extract a direct estimate of the effect from data using a “pseudo-embedding” of pp jets into a minimum bias PbPb data sample. The goal of this study is to verify that we recover a similar magnitude of excess yield as we attribute based on our more detailed PYTHIA+HYDJET simulations. Here we approximate the effect by adding the total transverse momentum in a circle of radius $r = 0.3$ around all jets with $p_T > 90$ GeV, and considering the total deviation up or down of this $(\Sigma p_T)_{\text{cone}}$ from the average total transverse momentum $\langle (\Sigma p_T)_{\text{cone}} \rangle$. First, we may directly compare the average p_T and fluctuations in p_T in these random cones between data and Monte Carlo. We find that our Monte Carlo approximately reproduces the data: in data $\langle (\Sigma p_T)_{\text{cone,data}} \rangle = 10.0$ GeV, with $\sigma((\Sigma p_T)_{\text{cone,data}}) = 4.9$ GeV, while in Monte Carlo $\langle (\Sigma p_T)_{\text{cone,MC}} \rangle = 11.9$ GeV, with $\sigma((\Sigma p_T)_{\text{cone,data}}) = 5.6$ GeV.

We then use these random cones to adjust jet energy and re-select jets: we add the deviation up or down of this $(\Sigma p_T)_{\text{cone}}$ to each embedded pp jets with this adjusted p_T . We then fill $\Delta\eta - \Delta\phi$ correlations to all jets that pass our nominal $p_T > 120$ GeV jet selection cut. We apply this technique to both our PYTHIA+HYDJET sample and a minimum-bias PbPb data sample to measure the charged particle yield associated with the embedded jet axis as a result of the jet fluctuation bias. As Fig. 23–24 show, this data pseudo-embedding recovers the same magnitude of excess yield due to background fluctuation bias as our nominal Monte Carlo studies, but artificially confines

807 this effect to a $r = 0.3$ cone due to the artificially simple jet reconstruction procedure. This gives
 808 confidence that the origin and magnitude of the effect are well-understood.

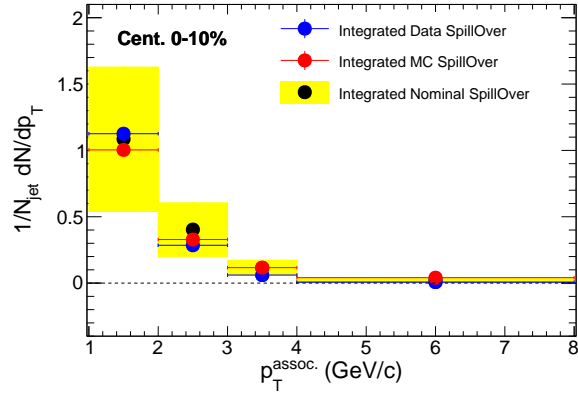


Figure 23. Total integrated magnitude of background fluctuation bias as simulated with pp jets embedded in Minimum Bias events (blue points) compared to the effect as simulated with PYTHIA jets into minimum bias HYDJET and to nominal corrections obtained with full PYTHIA+HYDJET simulation. Nominal systematic errors of $\pm 50\%$ as assigned in this analysis are shown as yellow systematic error bars on nominal (full MC simulation) points.

809 The background fluctuation bias could also be sensitive to the same calorimeter nonlinearity
 810 bias that necessitates fragmentation-jet energy corrections. To study this question and validate the
 811 uncertainty associated with this correction, we separately study the effect for quark jets and gluon
 812 jets, as shown in Figure 25. We find that this bias affects gluon jets slightly more than quark jets,
 813 consistent with deterioration of jet reconstruction performance for broader/softer jets, but that
 814 these deviations are within the 50% systematic uncertainty assigned.

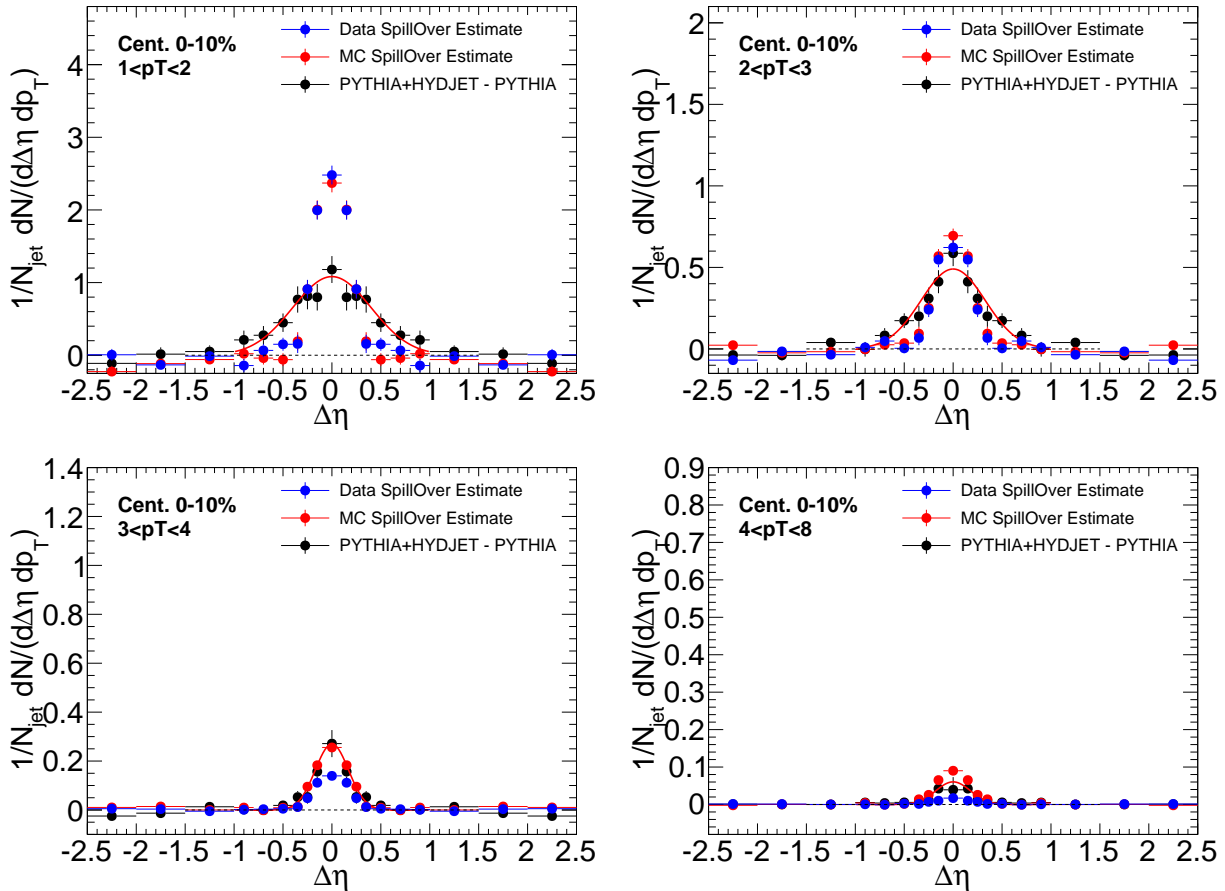


Figure 24. Correlated yield $\Delta\eta$ due to background fluctuation bias as simulated with pp jets embedded in Minimum Bias events (blue points) compared to the effect applying the same technique with PYTHIA jets in HYDJET minimum bias events, as well as in full PYTHIA+HYDJET simulation (black points with red fit line).

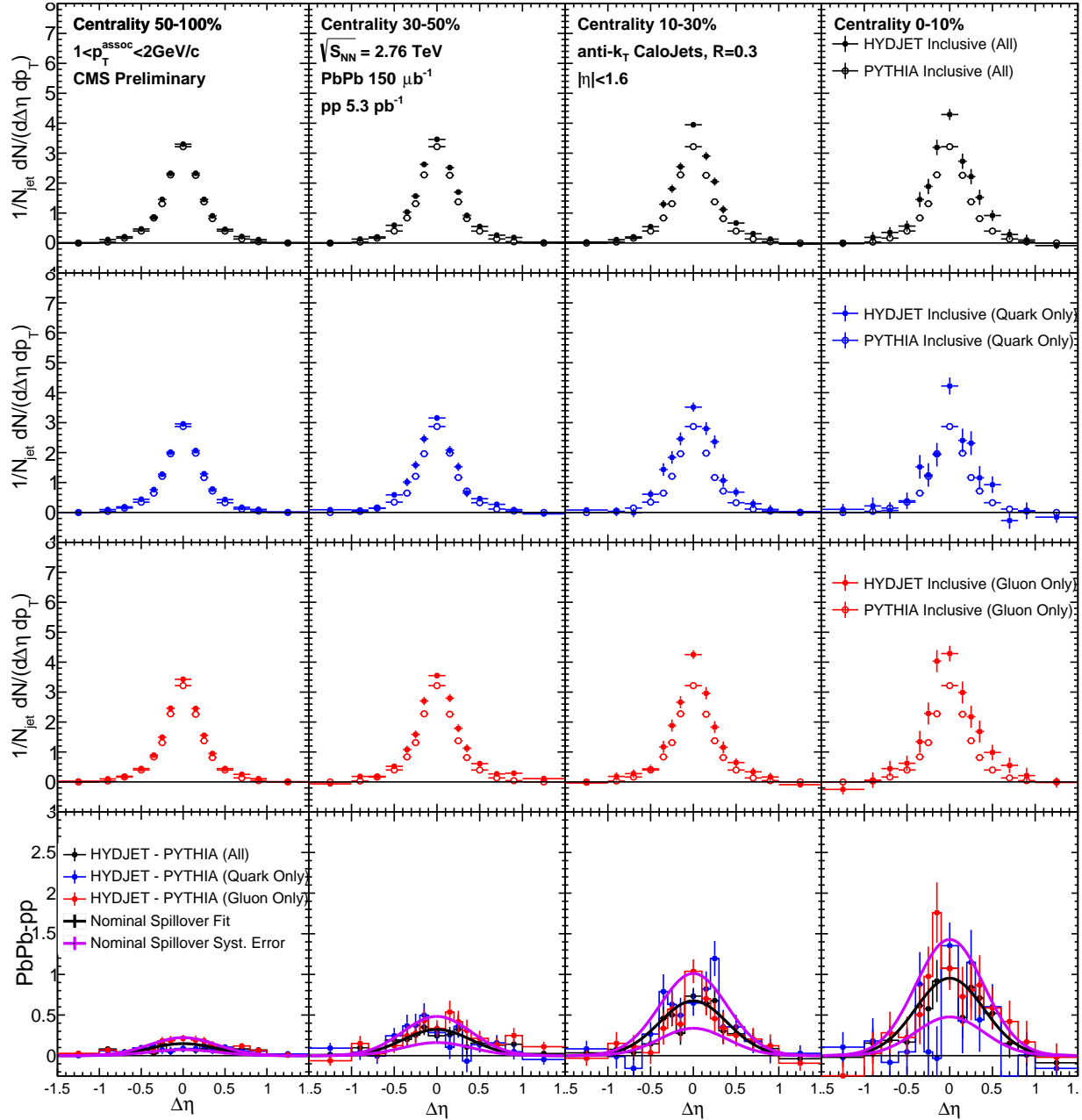


Figure 25. Comparison of magnitude of background selection bias effect for quark and gluon jets versus our nominal sample. Jet selection is inclusive in all cases.

815 **7.6 Evaluation of systematic uncertainties**

816 A number of sources of systematic uncertainty have been discussed in presenting jet and track
817 reconstruction and the jet-track correlation analysis procedure. To estimate the total systematic
818 uncertainty in these measurements, these contributions are added in quadrature. A brief summary
819 of all systematic uncertainty contributions, together with the procedure used to estimate their
820 magnitude follows. The contributions from each source (relative to jet peak signal) are summarized
821 in Tables [V](#)–[VII](#).

822 **7.6.1 Systematic uncertainties related to jet reconstruction**

823 Jet reconstruction-related sources of systematic uncertainty in this analysis include the two recon-
824 struction biases as discussed above, as well uncertainty associated with the jet energy scale (JES)
825 evaluation. We consider three sources of uncertainty on the JES: (1) differences in calorimeter
826 response for quark versus gluon jets, meaning that medium-induced changes in jet flavor could
827 result in either over-correction or under-correction of jet energy and a resulting bias in jet selection
828 (evaluated via Monte Carlo non-closure for quark and gluon jets); (2) possible differences between
829 data and simulation; (3) uncertainty due to quenching effects not included in our HYDJET simula-
830 tion. To evaluate how each of these sources of JES uncertainty affects final correlations, we vary jet
831 selection threshold by the combined uncertainty, and then quantify the resulting differences in the
832 final correlations as a measure of the combined residual JES uncertainty. Since all the measured
833 correlations are studied per-reconstructed jets, the jet reconstruction efficiency does not contribute
834 to the systematic uncertainty of this measurement.

835 **7.6.2 Systematic uncertainties related to tracking and tracking efficiency corrections**

836 The tracking efficiency correction uncertainty is estimated from the ratio of corrected reconstructed
837 yields and generated yields by using generator level charged particles as a “truth” reference. To ac-
838 count for the possible track reconstruction differences in data and simulation, a residual uncertainty
839 in track reconstruction efficiency and fake rate corrections is also estimated.

840 **7.6.3 Systematic uncertainty associated with pair acceptance correction and event
841 decomposition**

842 Uncertainty arising from pair-acceptance effects is estimated by considering the sideband asymme-
843 try after dividing by the mixed-event background. Each sideband region of the final $\Delta\eta$ distribution
844 ($-2.5 < \Delta\eta < -1.5$ and $1.5 < \Delta\eta < 2.5$) is separately fit with a horizontal line after background
845 subtraction. The greater of these two deviations from zero is assigned as systematic error. Un-
846 certainties resulting from the background subtraction are determined by considering the average
847 point-to-point deviation in two parts of the sideband region ($1.5 < |\Delta\eta| < 2.0$ and $2.0 < |\Delta\eta| < 2.5$)
848 after background subtraction. The derivations of both of these sources of uncertainty are illustrated
849 in Appendix C. In PbPb data this background subtraction uncertainty is greatest for the most cen-
850 tral events (0–10%) and the lowest track p_T bin where the background is most significant compared
851 to the signal level, and decreases for less central collisions and for higher p_T tracks ($p_T^{\text{trk}} > 2$ GeV).

852 **7.6.4 Summary of systematic uncertainties**

853 The contributions to total systematic uncertainty from each of the sources described above are given
854 in Tables V–VII. Table V gives uncertainty evaluations for correlation studies at 2.76 TeV, while
855 Table VI gives the same for studies at 5.02 TeV. Finally, Table VII gives uncertainty evaluations
856 for balanced ($A_J < 0.22$) and unbalanced ($A_J > 0.22$) dijet events in momentum balance studies
857 at 2.76 TeV.

TABLE V. Systematic uncertainties in the measurement of the jet-track correlations in PbPb and pp collisions at 2.76 TeV, as percentage of the total measured correlated yield. The numbers presented in this table summarize the range of values of systematic uncertainty (as a function of p_T^{trk}) for different centrality bins.

Source	0–10%	10–30%	30–50%	50–100%	pp
Background fluctuation bias	3–12%	2–7%	1–5%	0–1%	–
Jet fragmentation function bias	0–2%	0–2%	0–2%	0–2%	0–2%
Residual jet energy scale	3%	3%	3%	3%	3%
Tracking efficiency uncertainty	4%	4%	4%	4%	3 %
Residual track efficiency corr.	5%	5%	5%	5%	5%
Pair acceptance corrections	5–9%	5–9%	4–8%	2–6%	2–3%
Background subtraction	2–5%	2–5%	2–5%	2–5%	1–2%
Total	9–17%	9–14%	8–13%	8–10%	7–8%

TABLE VI. Systematic uncertainties in the measurement of the jet track correlations in PbPb and pp collisions at 5.02 TeV. The numbers presented in this table summarize typical range of systematic uncertainty as a function of collision centrality. The upper limits of the cited values correspond to uncertainties at lowest p_T^{trk} , and uncertainties decrease with rising p_T^{trk} .

Source	0–10%	10–30%	30–50%	50–100%	ppRef
Background fluctuation bias	0–10%	0–5%	0–2%	0–1%	–
Background fluctuation bias residual	0–2%	0–3%	0–1%	0–1%	–
JFF bias	3–5%	3–4%	3–4%	3–4%	3%
Residual JES	4%	4%	4%	4%	4%
Tracking efficiency uncertainty	1%	1%	1%	1%	1%
Residual tracking efficiency	5%	5%	5%	5%	5%
Pair-acceptance corrections	1–5%	1–4%	1–4%	1–4%	1–2%
Event decomposition	1–9%	0–4%	0–4%	0–3%	0–3%
Total	7–16%	7–11%	7–9%	7–9%	7–8%

TABLE VII. This table summarizes the systematic uncertainties in the measurement of the p_T^{trk} correlations in PbPb and pp collisions at 2.76 TeV. Upper and lower limits are shown as a function of collision centrality. Upper values correspond to the uncertainties at lowest p_T^{trk} .

Source	0–30%	30–50%	50–100%	pp
Balanced jet selection ($A_J < 0.22$):				
Background fluctuations	1–8%	1–3%	0–1%	–
JFF bias and jet swapping	0–2%	0–2%	0–2%	0–2%
Residual JES	3%	3%	3%	3%
Tracking efficiency	4%	4%	4%	3 %
Residual track efficiency corr.	5%	5%	5%	5%
Pair acceptance corrections	5–9%	4–8%	2–6%	2–3%
Event decomposition	2–5%	2–5%	2–5%	1–2%
Total	9–15%	8–13%	8–10%	7–8%
Unbalanced jet selection ($A_J > 0.22$):				
Background fluctuations	1–10%	1–5%	0–2%	–
JFF bias and jet swapping	0–2%	0–2%	0–2%	0–2%
Residual JES	3%	3%	3%	3%
Tracking efficiency	4%	4%	4%	3 %
Residual track efficiency corr.	5%	5%	5%	5%
Pair acceptance corrections	5–9%	4–8%	2–6%	2–3%
Event decomposition	2–5%	2–5%	2–5%	1–2%
Total	9–16%	8–13%	8–10%	7–8%

8 DISCUSSION OF RESULTS

859 Jet-track correlation studies can produce measurements the density of particles (in each p_T^{trk} class)
 860 with respect to the jet axis and can also, by creating correlations weighted per-track by its p_T^{trk} , pro-
 861 duce measurements of the distribution of p_T^{trk} in the event as a whole. Both types of measurements
 862 are presented here, for inclusive selections of jets with $p_T > 120$ GeV and for high- p_T dijet events
 863 at 2.76 TeV and 5.02 TeV. First, particle density correlation results are presented in Secs. 8.1- 8.2.
 864 Next, p_T^{trk} distributions are used to extract measurements of jet shapes (the transverse momentum
 865 profiles of jets) in Sec. 8.3. Finally, in Sec. 8.4, p_T^{trk} distributions are used to decompose and analyze
 866 the hemisphere momentum balance in dijet events.

867 8.1 Inclusive jet particle density correlation results

868 Particle density correlation studies allow for the detailed characterization of jet fragmentation,
 869 and of medium-induced modifications to jet fragmentation in PbPb data (as a function of collision
 870 centrality) compared to pp data. The analysis procedure described in Sec. 7 results in fully-corrected
 871 2D jet peaks in $\Delta\eta - \Delta\phi$, which may then be projected to obtain the distribution of particles in
 872 each p_T^{trk} class as a function of $\Delta\eta$ and $\Delta\phi$. The top panels of Figs. 26-33 show these $\Delta\eta$ and
 873 $\Delta\phi$ distributions (projected over $|\Delta\phi| < 1$ and $|\Delta\eta| < 1$, respectively) for 2.76 TeV pp data and
 874 PbPb data in each p_T^{trk} range from 1–2 GeV (Fig. 26-27) up to 4–8 GeV (Fig. 32-33). The bottom
 875 panels of these figures show the differences PbPb–pp for illustration of medium modifications to jet
 876 fragmentation patterns. In both the $\Delta\eta$ and $\Delta\phi$ dimensions, centrality-dependent excesses of soft
 877 (low- p_T^{trk}) particles are evident. These exhibit the greatest modifications in the most central PbPb
 878 collisions, decreasing with centrality until the most peripheral collisions show little modification
 879 when compared to pp data. These excesses decrease with increasing p_T^{trk} , until in the 4–8 GeV
 880 range the enhancements evident at lowest- p_T^{trk} reverse to possible slight depletion. In both $\Delta\eta$ and
 881 $\Delta\phi$ dimensions, the soft excesses exhibit a gaussian-like distribution around the jet axis, while also
 882 extending to large angles $\Delta\eta = 1$ and $\Delta\phi = 1$ at lowest p_T^{trk} .

883 Figures 34 and 35 show the corresponding $\Delta\eta$ and $\Delta\phi$ distributions at 5.02 TeV. Here,
 884 the distribution of particles in each p_T^{trk} class are stacked (with lowest- p_T^{trk} particles on top), and
 885 pp data shown separately at left. Again the differences PbPb–pp are shown in bottom panels to

illustrate the medium modifications, and exhibit similar qualitative trends to those described above
 for 2.76 TeV results. Results may also be presented as a function of radial distance from the jet axis
 $\Delta r = \sqrt{\Delta\eta^2 + \Delta\phi^2}$. Figure 36 presents charged particle yields, differentially in p_T^{trk} , as a function
 of Δr . For comparison, the bottom row of each plot shows the difference, PbPb minus pp. This
 shows the particles contributing to a jet fragmentation function measurement within a given radius
 from a jet, and illustrates the radial dependence of modifications extending to at least $\Delta r = 1$.

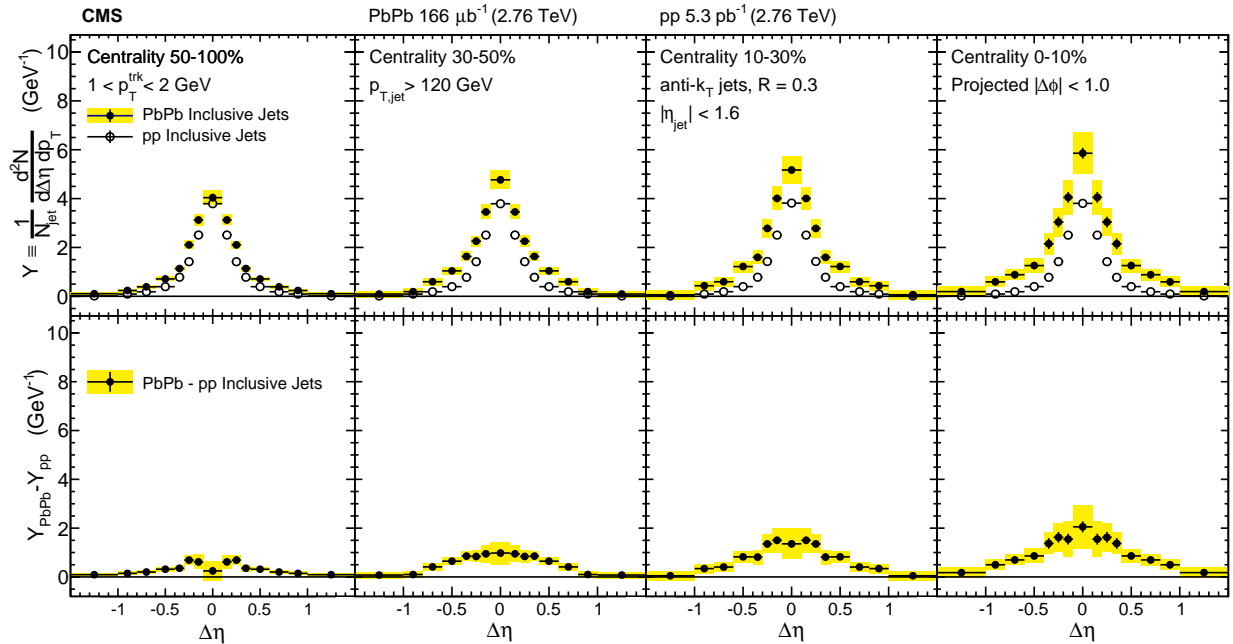


Figure 26. Symmetrized $\Delta\eta$ distributions (projected over $|\Delta\phi| < 1$) of background-subtracted particle yields correlated to PbPb and pp inclusive jets with $p_T > 120$ GeV are shown in the top panels for tracks with $1 < p_T^{\text{trk}} < 2$ GeV. The difference in PbPb and pp per-jet yields is shown in the bottom panels. The total systematic uncertainties are shown as shaded boxes, and statistical uncertainties are shown as vertical bars (often smaller than the symbol size).

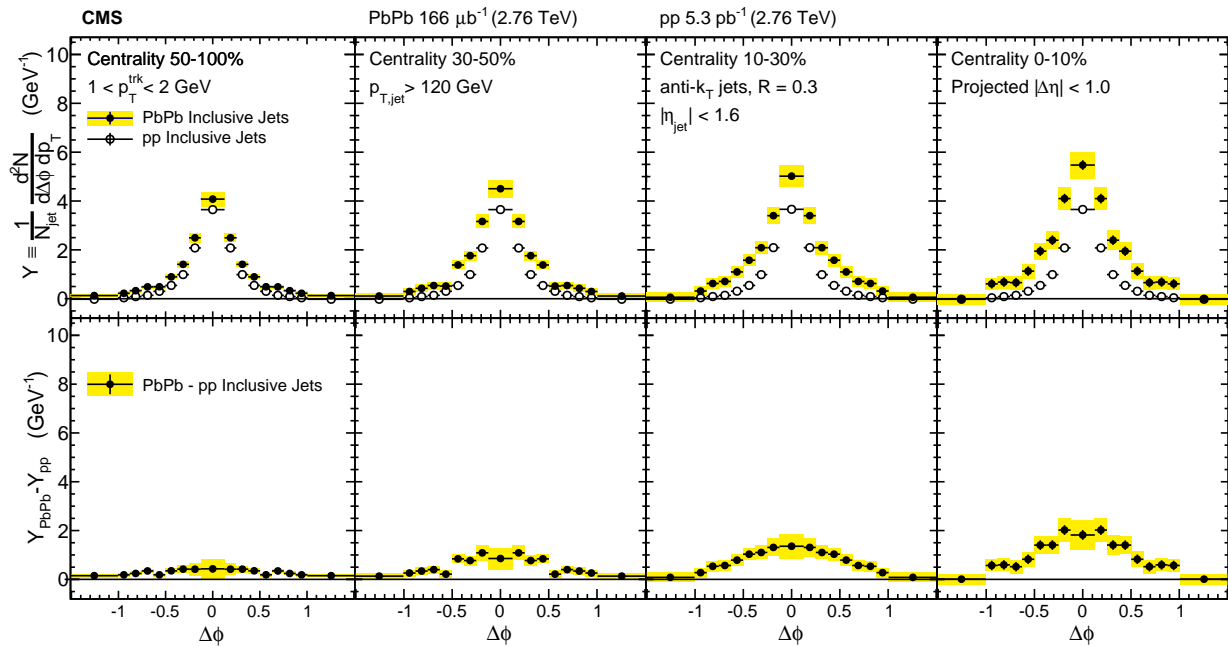


Figure 27. Symmetrized $\Delta\phi$ distributions (projected over $|\Delta\eta| < 1$) of background-subtracted particle yields correlated to PbPb and pp inclusive jets with $p_T > 120$ GeV are shown in the top panels for tracks with $1 < p_T^{\text{trk}} < 2$ GeV. The difference in PbPb and pp per-jet yields is shown in the bottom panels. The total systematic uncertainties are shown as shaded boxes, and statistical uncertainties are shown as vertical bars (often smaller than the symbol size).

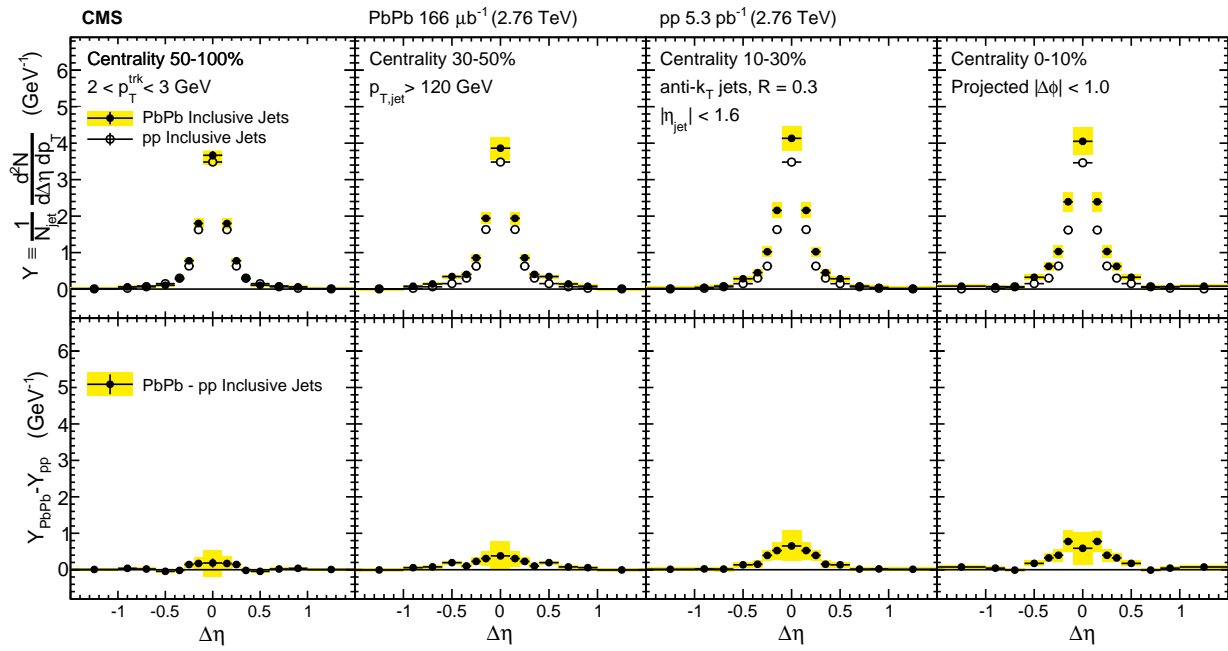


Figure 28. Symmetrized $\Delta\eta$ distributions (projected over $|\Delta\phi| < 1$) of background-subtracted particle yields correlated to PbPb and pp inclusive jets with $p_T > 120 \text{ GeV}$ are shown in the top panels for tracks with $2 < p_T^{\text{trk}} < 3 \text{ GeV}$. The difference in PbPb and pp per-jet yields is shown in the bottom panels. The total systematic uncertainties are shown as shaded boxes, and statistical uncertainties are shown as vertical bars (often smaller than the symbol size).

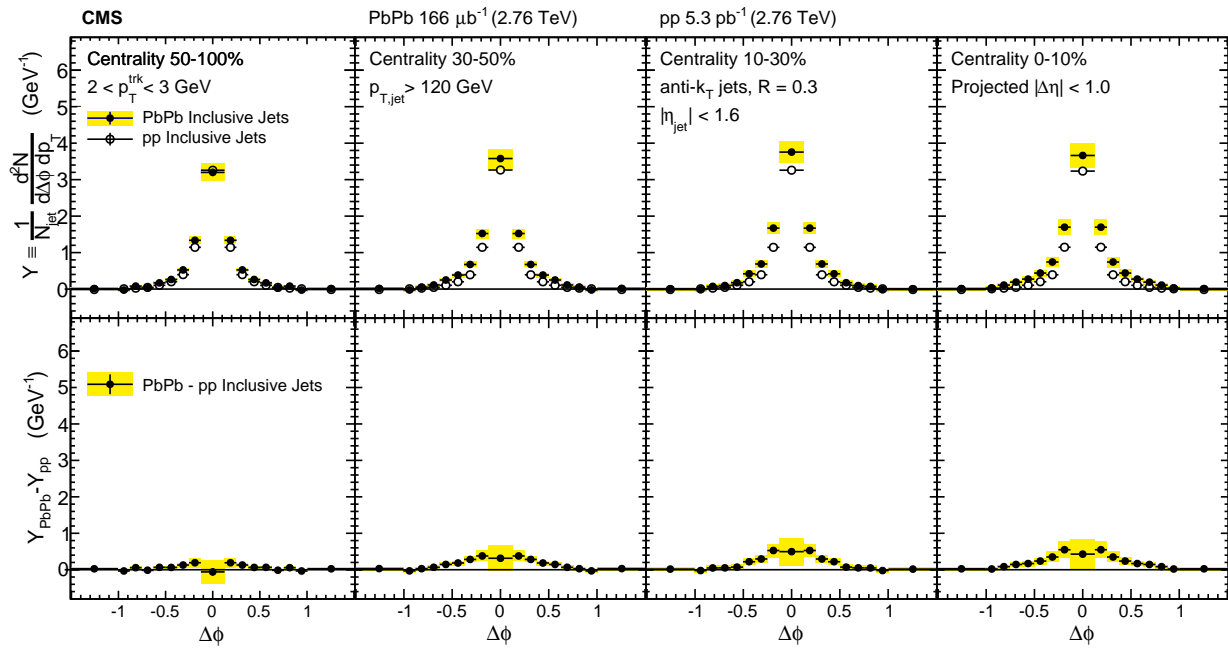


Figure 29. Symmetrized $\Delta\phi$ distributions (projected over $|\Delta\eta| < 1$) of background-subtracted particle yields correlated to PbPb and pp inclusive jets with $p_T > 120$ GeV are shown in the top panels for tracks with $2 < p_T^{\text{trk}} < 3$ GeV. The difference in PbPb and pp per-jet yields is shown in the bottom panels. The total systematic uncertainties are shown as shaded boxes, and statistical uncertainties are shown as vertical bars (often smaller than the symbol size).

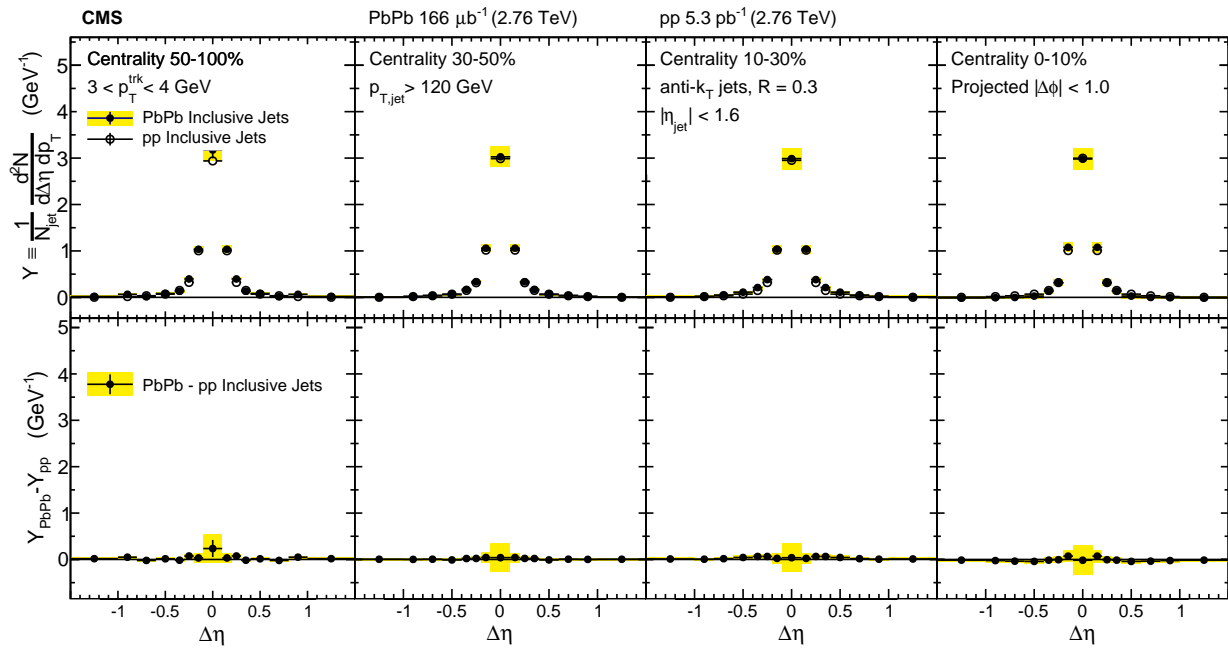


Figure 30. Symmetrized $\Delta\eta$ distributions (projected over $|\Delta\phi| < 1$) of background-subtracted particle yields correlated to PbPb and pp inclusive jets with $p_{\text{T}} > 120 \text{ GeV}$ are shown in the top panels for tracks with $3 < p_{\text{T}}^{\text{trk}} < 4 \text{ GeV}$. The difference in PbPb and pp per-jet yields is shown in the bottom panels. The total systematic uncertainties are shown as shaded boxes, and statistical uncertainties are shown as vertical bars (often smaller than the symbol size).

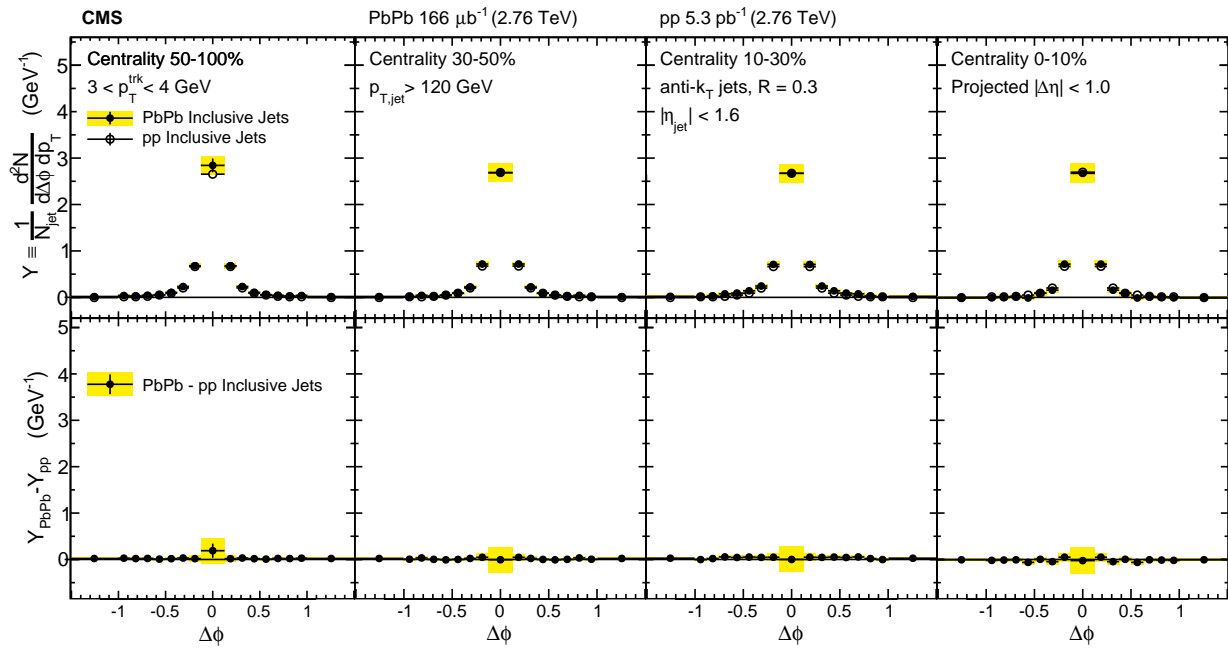


Figure 31. Symmetrized $\Delta\phi$ distributions (projected over $|\Delta\eta| < 1$) of background-subtracted particle yields correlated to PbPb and pp inclusive jets with $p_{\text{T}} > 120 \text{ GeV}$ are shown in the top panels for tracks with $3 < p_{\text{T}}^{\text{trk}} < 4 \text{ GeV}$. The difference in PbPb and pp per-jet yields is shown in the bottom panels. The total systematic uncertainties are shown as shaded boxes, and statistical uncertainties are shown as vertical bars (often smaller than the symbol size).

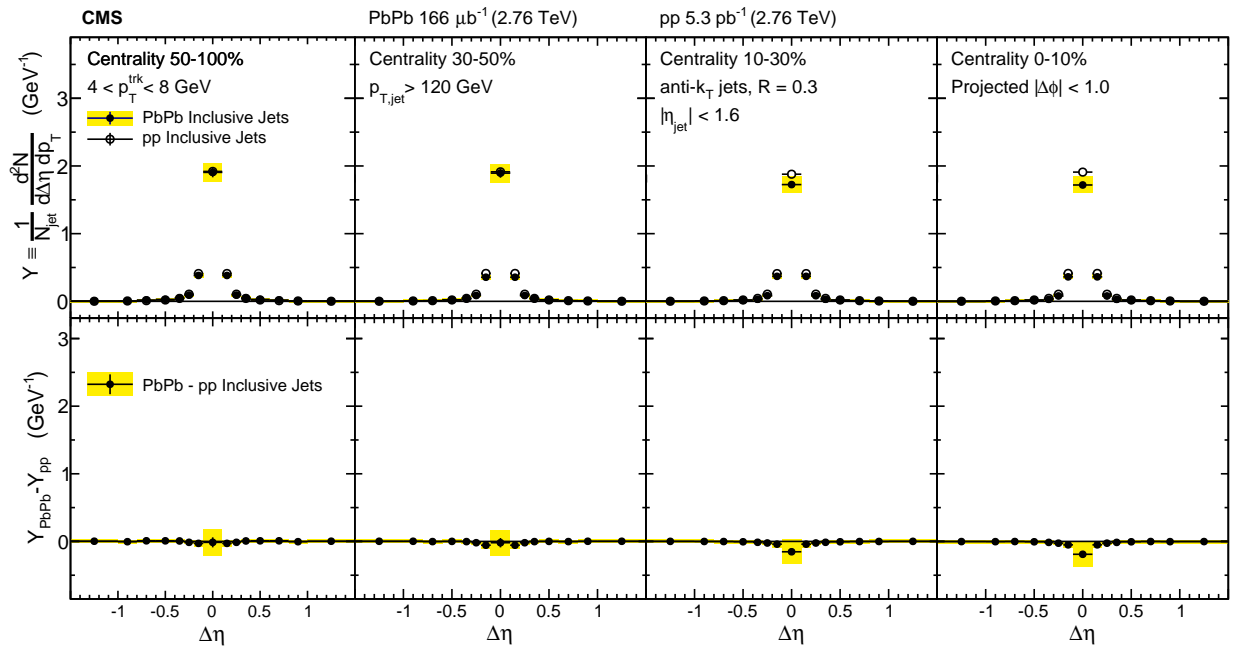


Figure 32. Symmetrized $\Delta\eta$ distributions (projected over $|\Delta\phi| < 1$) of background-subtracted particle yields correlated to PbPb and pp inclusive jets with $p_T > 120 \text{ GeV}$ are shown in the top panels for tracks with $4 < p_T^{\text{trk}} < 8 \text{ GeV}$. The difference in PbPb and pp per-jet yields is shown in the bottom panels. The total systematic uncertainties are shown as shaded boxes, and statistical uncertainties are shown as vertical bars (often smaller than the symbol size).

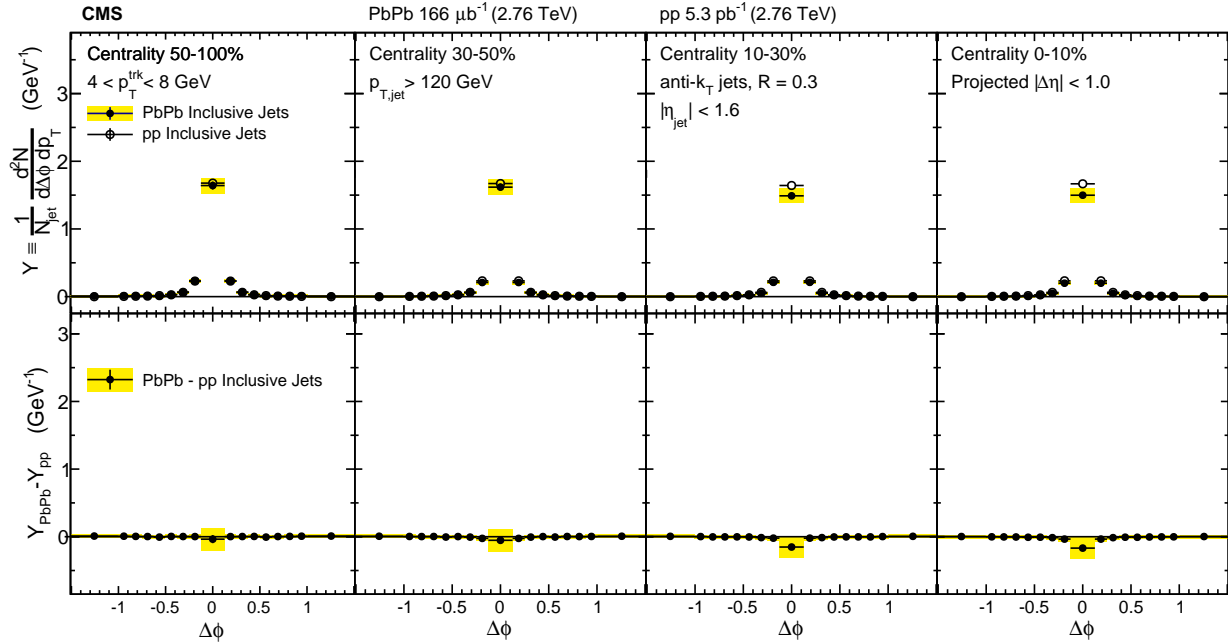


Figure 33. Symmetrized $\Delta\phi$ distributions (projected over $|\Delta\eta| < 1$) of background-subtracted particle yields correlated to PbPb and pp inclusive jets with $p_T > 120$ GeV are shown in the top panels for tracks with $4 < p_T^{\text{trk}} < 8$ GeV. The difference in PbPb and pp per-jet yields is shown in the bottom panels. The total systematic uncertainties are shown as shaded boxes, and statistical uncertainties are shown as vertical bars (often smaller than the symbol size).

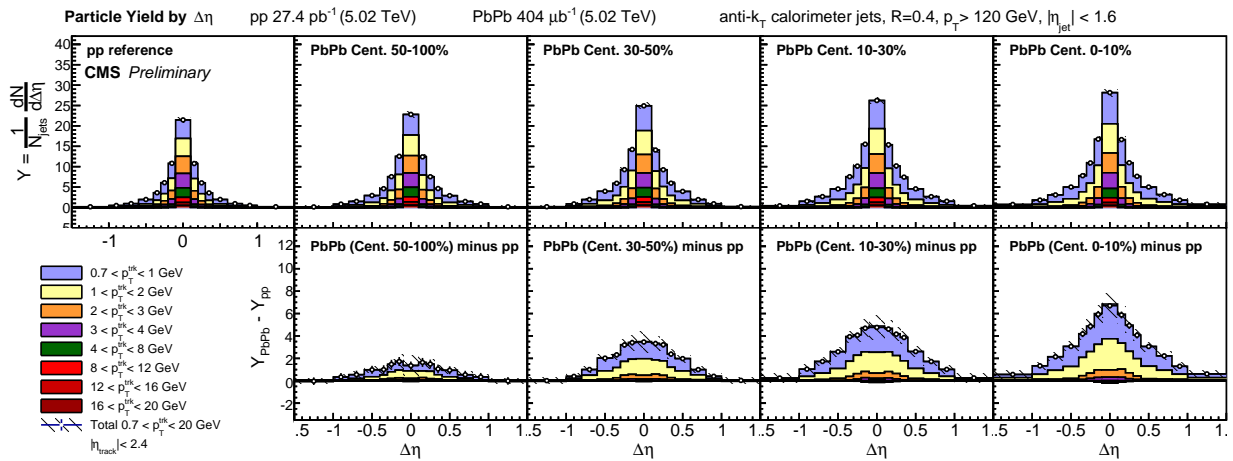


Figure 34. Top row: distributions of charged particle yields correlated to jets with $p_T > 120$ GeV as a function of $\Delta\eta$ (projected over $|\Delta\phi| < 1$), shown differentially for all p_T^{trk} bins for pp, peripheral PbPb, and central PbPb data. Bottom row: PbPb minus pp difference in these distributions. Hatched lines on p_T^{trk} -inclusive points show total systematic uncertainties.

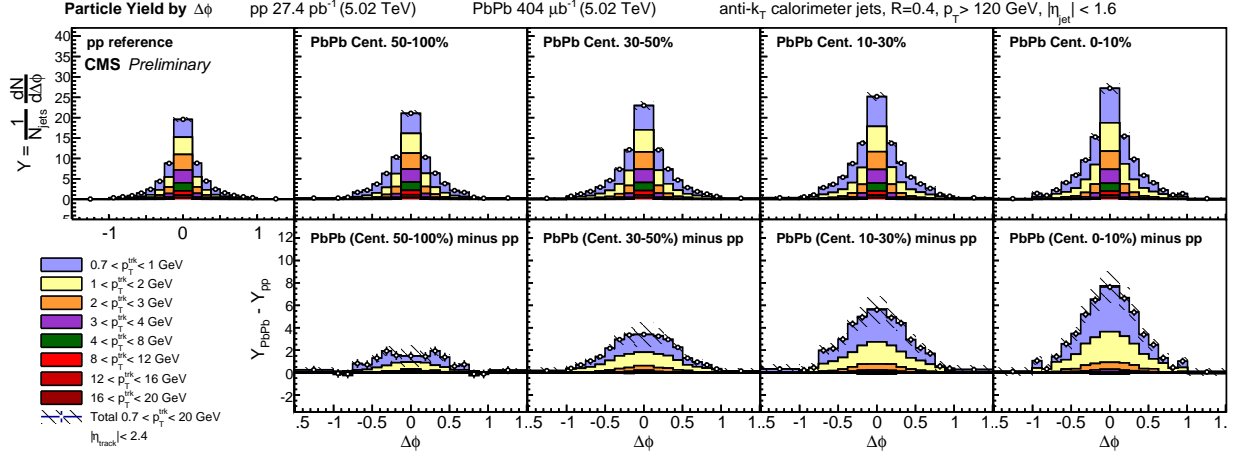


Figure 35. Top row: distributions of charged particle yields correlated to jets with $p_T > 120$ GeV as a function of $\Delta\phi$ (projected over $|\Delta\eta| < 1$), shown differentially for all p_T^{trk} bins for pp, peripheral PbPb, and central PbPb data. Bottom row: PbPb minus pp difference in these distributions. Hatched lines on p_T^{trk} -inclusive points show total systematic uncertainties.

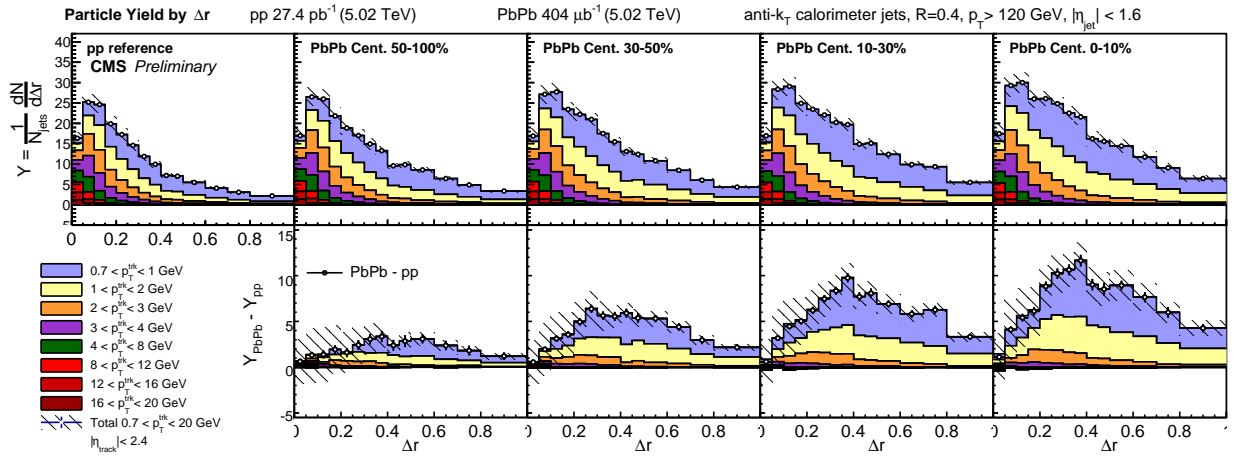


Figure 36. Top row: distributions of charged particle yields correlated to jets with $p_T > 120$ GeV as a function of Δr , shown differentially for all p_T^{trk} bins. Bottom row: PbPb minus pp difference in these distributions. Hatched lines on p_T^{trk} -inclusive points show total systematic uncertainties.

To summarize the magnitude of the modifications to particle yields in PbPb relative to pp collisions, integrated yields as a function of p_T^{trk} are presented in the top panel of Fig. 37. The bottom panel of Fig. 37 shows differences PbPb–pp in total integrated particle yields in each p_T^{trk} class for results at 5.02 TeV compared to 2.76 TeV results. This quantifies the low- p_T excess in central PbPb collisions to as many as 4 additional particles (in central PbPb relative to pp reference) per unit of p_T^{trk} in the lowest p_T^{trk} bin. This excess decreases smoothly with p_T^{trk} in each centrality bin, until the 4–8 GeV central PbPb bin is consistent with or slightly depleted relative to pp reference. For tracks with $p_T^{\text{trk}} > 8$ GeV, there is no evident modification in PbPb compared to pp. Excess yields do not exhibit significant dependence on collision energies; particle yields at low- p_T^{trk} are consistently larger at 5.02 TeV than at 2.76 TeV, but within the systematic uncertainties of the two measurements.

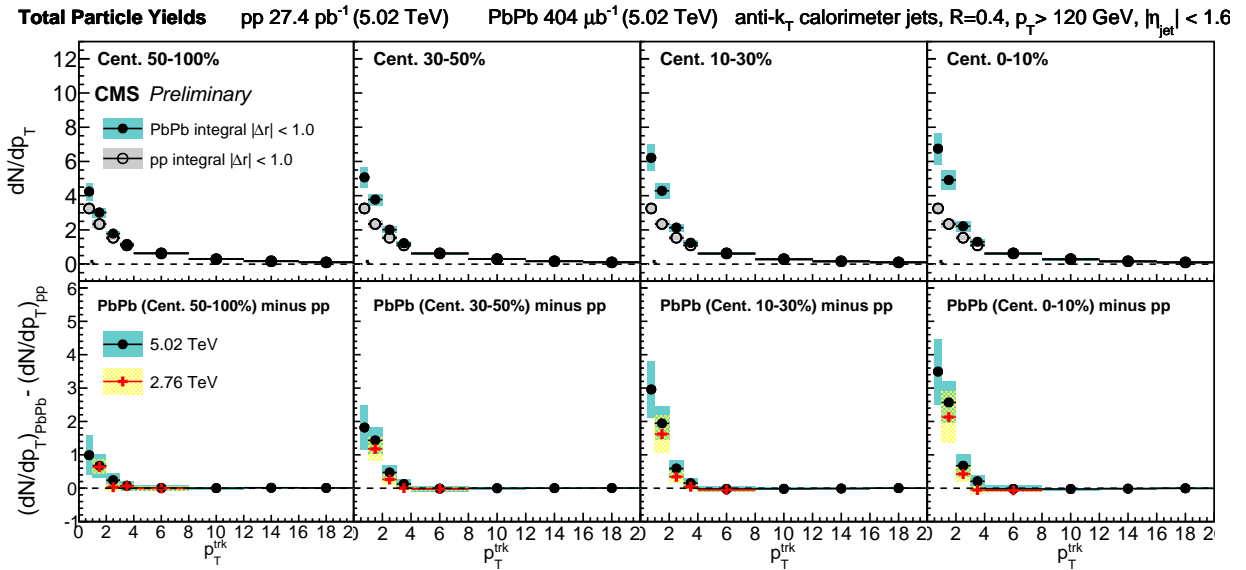


Figure 37. Top row: integrated yields of charged particle yields correlated to jets with $p_T > 120$ GeV as a function of p_T^{trk} bins for PbPb data, compared to pp reference. Bottom row: integrated excess yield, PbPb minus pp. New measurements of excess yields at 5.02 TeV are compared to those measured at 2.76 TeV.

903 **8.2 Dijet correlation results**

904 In the studies of charged-particle yields correlated to an inclusive sample of jets with $p_T > 120$
905 GeV presented above, jet quenching is evident in the redistribution of p_T^{trk} from harder to softer
906 particles, and particularly in the observed centrality-dependent excess of low- p_T^{trk} particle yields. Jet
907 quenching effects may be further probed by considering charged-particle yields correlated to each
908 jet axis in dijet events. Requiring events with two back-to-back jets (leading jet $p_{T,1} > 120$ GeV,
909 subleading jet $p_{T,2} > 50$ GeV, $\Delta\phi_{1,2} > \frac{5\pi}{6}$), we construct separate correlations to the leading and
910 the subleading jet axes. In pp data, most dijets are balanced while in central PbPb a greater fraction
911 of dijet pairs are unbalanced (as discussed in Sec. 6.4), suggesting that central PbPb data contains
912 a significant fraction of dijet pairs in which the highest- and second-highest- p_T hard-scattering
913 products had similar transverse momenta, but in which one jet experienced a greater path-length
914 through the medium and correspondingly greater quenching. This is expected to correspond to a
915 “surface-bias” toward leading jets with very short path-lengths through the medium, that might be
916 expected to correspond to minimal quenching in the leading jet sample. It is therefore interesting
917 to separately compare charged-particle distributions with respect to the leading and subleading jet
918 axes in PbPb and pp data to look for evidence of path-length dependence in jet quenching.

919 Figures 38 and 39 show these correlation patterns in $\Delta\eta$ and $\Delta\phi$, respectively, for the
920 $1 < p_T^{\text{trk}}$ GeV range in which the greatest quenching was evident in the 2.76 TeV inclusive jet
921 studies. As expected, quenching effects are greater for subleading than leading jets, as evident in
922 larger excesses of soft particles in subleading jet correlations (while retaining the same centrality
923 trends and gaussian-like distributions observed for the inclusive jet sample). However, leading jets
924 exhibit evidence of quenching as well, showing similar soft-particle excesses to those observed in
925 the inclusive sample. To quantitatively compare subleading and leading jet modifications to those
926 in the inclusive jet sample, Fig. 40 shows integrated particle yields for all three jet samples at 2.76
927 TeV. Here it is clear that leading jets show similar PbPb–pp modifications to those observed in the
928 inclusive sample, with approximately 2 excess particles in PbPb compared to pp data at lowest- p_T^{trk} ,
929 while the subleading jet sample shows as many as 4 excess particles in PbPb compared to pp data
930 at lowest- p_T^{trk} .

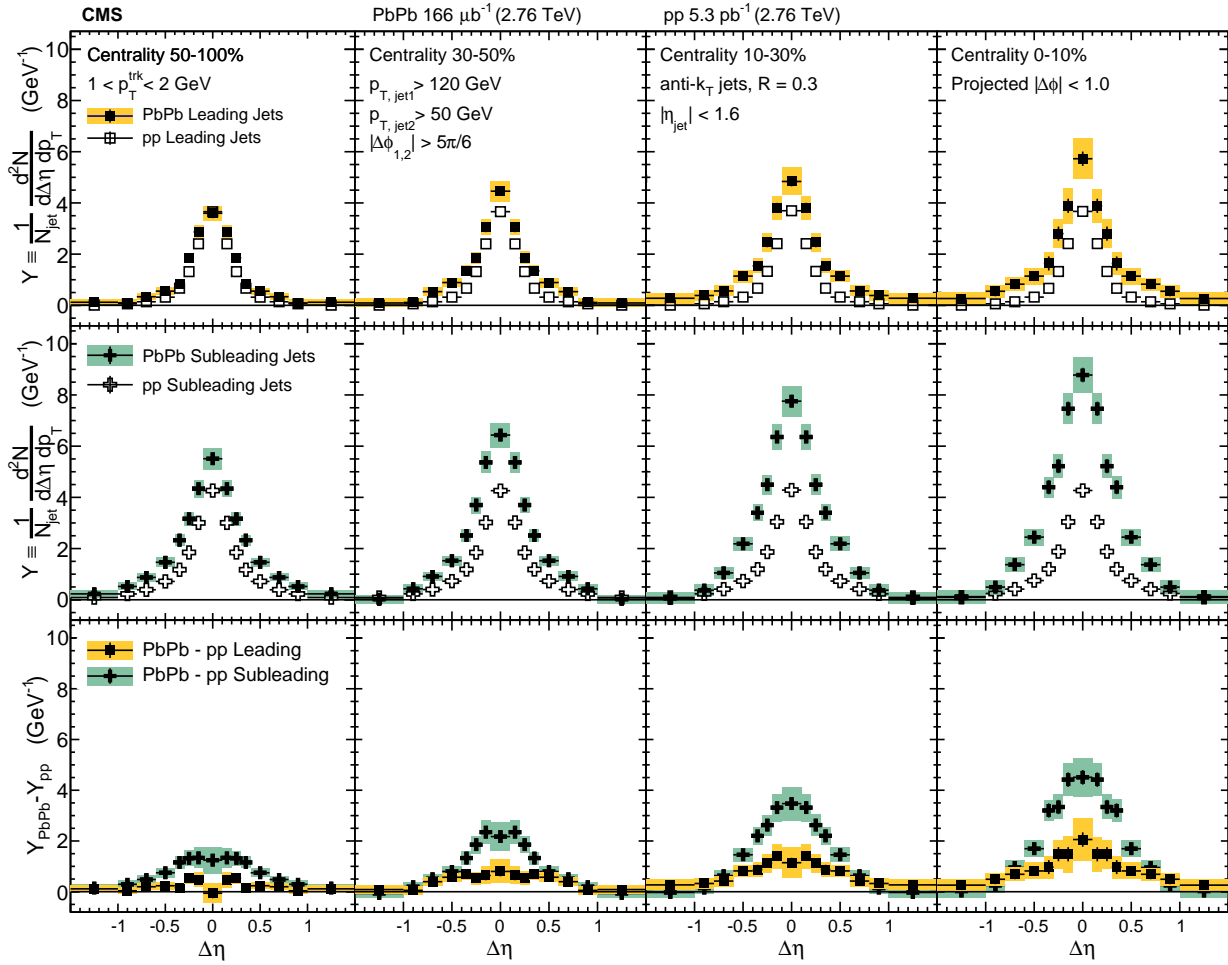


Figure 38. The top panels show the $\Delta\eta$ distributions (projected over $|\Delta\phi| < 1$) of charged-particle background-subtracted yields correlated to PbPb and pp leading jets with $p_{T,\text{jet}1} > 120$ GeV. The middle panels show the same distributions for subleading jets with $p_{T,\text{jet}2} > 50$ GeV, and the bottom panels show the difference PbPb minus pp for both leading and subleading jets. The total systematic uncertainties are shown as shaded boxes, and statistical uncertainties are shown as vertical bars (often smaller than the symbol size).

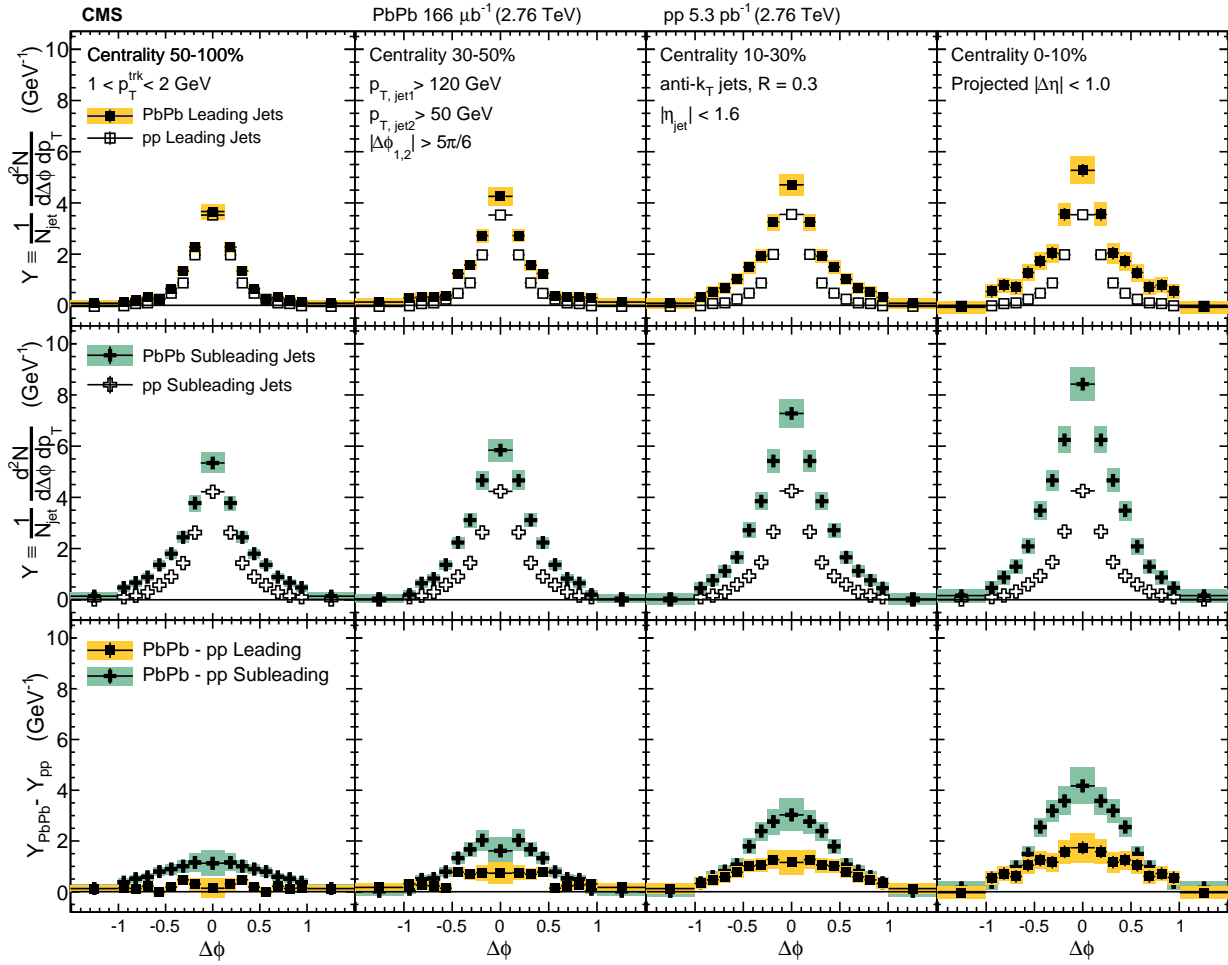


Figure 39. The top panels show the $\Delta\phi$ distributions (projected over $|\Delta\eta| < 1$) of charged-particle background-subtracted yields correlated to PbPb and pp leading jets with $p_{T,\text{jet}1} > 120$ GeV. The middle panels show the same distributions for subleading jets with $p_{T,\text{jet}2} > 50$ GeV, and the bottom panels show the difference PbPb minus pp for both leading and subleading jets. The total systematic uncertainties are shown as shaded boxes, and statistical uncertainties are shown as vertical bars (often smaller than the symbol size).

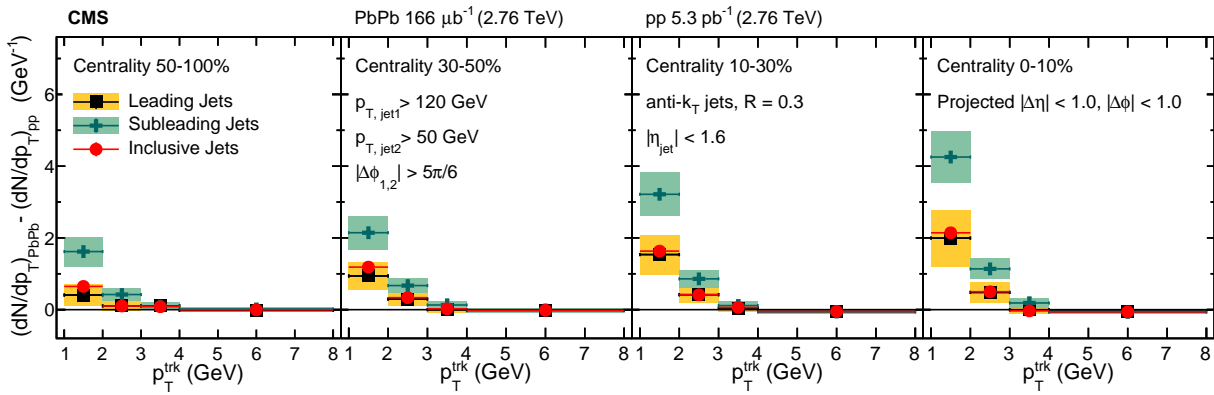


Figure 40. Total excess correlated yield observed in the PbPb data with respect to the reference measured in pp collisions, shown as a function of track p_{T} in four different centrality intervals (0–10%, 10–30%, 30–50%, 50–100%) for both leading jets with $p_{\text{T},\text{jet}1} > 120 \text{ GeV}$ and subleading jets with $p_{\text{T},\text{jet}2} > 50 \text{ GeV}$. The total systematic uncertainties are shown as shaded boxes, and statistical uncertainties are shown as vertical bars (often smaller than the symbol size).

In addition to characterizing the magnitude of jet quenching products (via the centrality-dependent excess of low- p_T^{trk} tracks greatest in correlations to subleading jets but also present in leading jet correlations), modifications to charged-particle correlated yields may also be characterized by their widths. These studies are relevant to look for the presence and extent of jet peak broadening due to medium interactions, and can be used to distinguish between different models for jet-medium interaction and medium-modified jet radiation. In order to characterize correlation widths, correlations are fit to double-gaussian functions (all $\Delta\eta$ fits are shown in Appendix D for illustration), and the width (σ) of these fits is obtained as the range in $|\Delta\eta|$ or $|\Delta\phi|$ containing 67% of the total yield under the fit curve. To obtain systematic uncertainties on these fits, points are varied up and down by their systematic uncertainties, and widths are re-calculated from these varied distributions.

Figures 41 and 42 show correlation widths in $\Delta\eta$ and $\Delta\phi$ for leading jets in PbPb and pp data at 2.76 TeV. At low- p_T^{trk} there is a significant broadening evident in central PbPb data when compared to pp data, with this broadening decreasing in more peripheral collisions and with increasing p_T^{trk} (with similar trends to those exhibited by correlated yield magnitudes). Widths and width modifications are similar in $\Delta\eta$ and $\Delta\phi$, but slightly broader in $\Delta\phi$ for PbPb data. These leading jet correlation widths and width modifications may also be compared to subleading jet correlation widths and width modifications, shown in Figs. 43 and 44. In peripheral PbPb data subleading and leading correlation widths are similar, but subleading jet PbPb correlation widths exhibiting less centrality dependence than leading jet correlation widths so that leading jet correlations in central PbPb data are slightly broader than subleading jet correlations (but not significantly so, when taking into account the systematic uncertainties on both measurements). Subleading jet peaks in pp data are, however, significantly broader than leading jet peaks in pp data—as is to be expected since the kinematic selection defining subleading jet as that with lower- p_T , also implies that subleading jets will on average have softer fragmentation than leading jets. Since subleading pp jets are broader than leading pp jets while subleading and leading jets have similar widths in PbPb, the jet peak broadening quantified as the PbPb–pp difference in widths is greater for leading jets than for subleading jets.

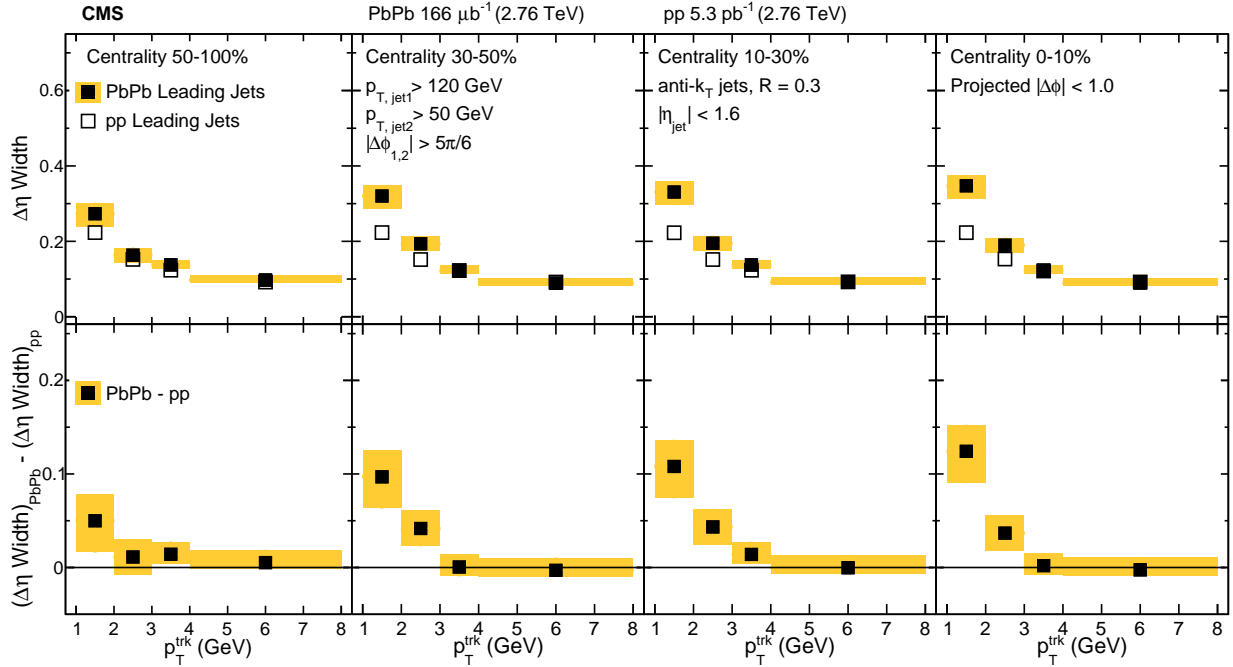


Figure 41. Comparison of the widths in PbPb and pp of the $\Delta\eta$ charged-particle distributions correlated to leading jets with $p_{T,\text{jet}1} > 120 \text{ GeV}$, as a function of p_T^{trk} . The bottom row shows the difference of the widths in PbPb and pp data. The shaded band corresponds to systematic uncertainty, and statistical uncertainties are smaller than symbol size.

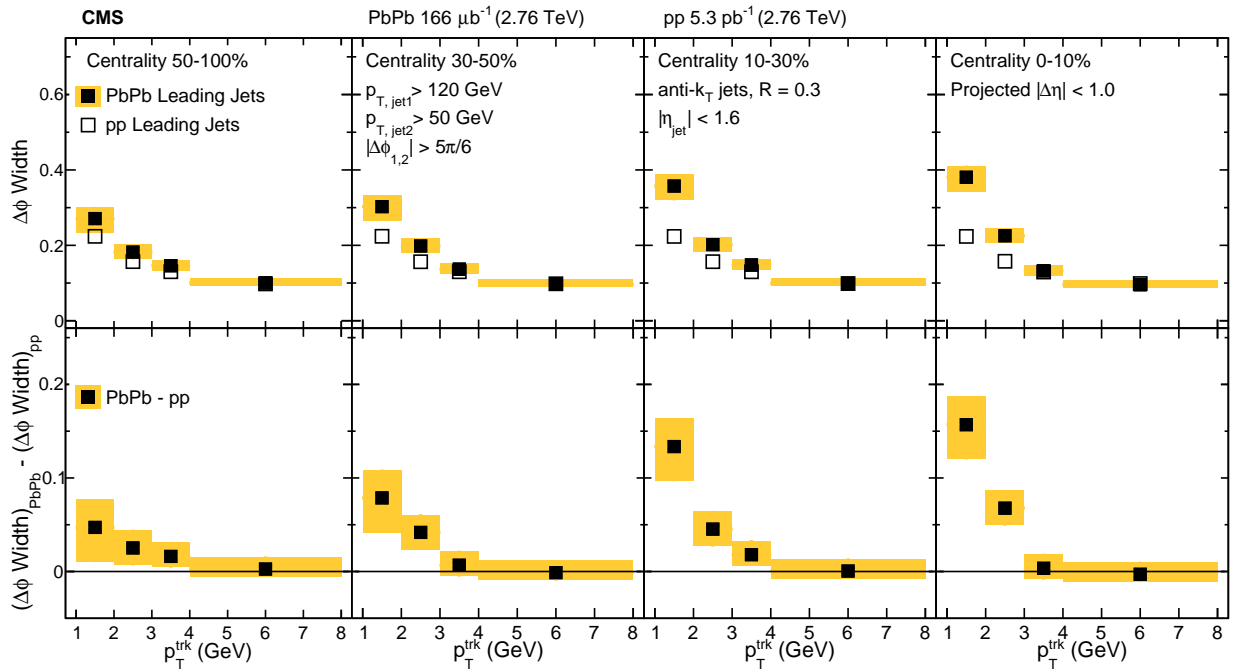


Figure 42. Comparison of the widths in PbPb and pp of the $\Delta\phi$ charged-particle distributions correlated to leading jets with $p_{T,\text{jet}1} > 120 \text{ GeV}$, as a function of p_T^{trk} . The bottom row shows the difference of the widths in PbPb and pp data. The shaded band corresponds to systematic uncertainty, and statistical uncertainties are smaller than symbol size.

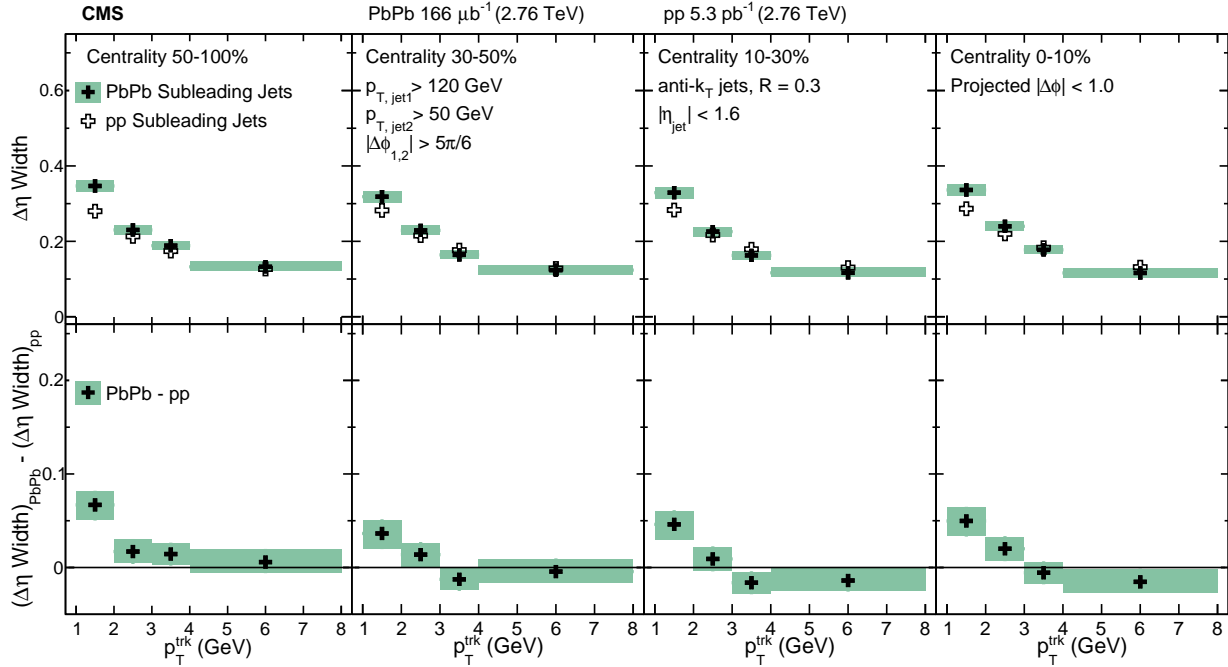


Figure 43. Comparison of the widths in PbPb and pp of the $\Delta\eta$ charged-particle distributions correlated to leading jets with $p_{T,\text{jet}2} > 50 \text{ GeV}$, as a function of p_T^{trk} . The bottom row shows the difference of the widths in PbPb and pp data. The shaded band corresponds to systematic uncertainty, and statistical uncertainties are smaller than symbol size.

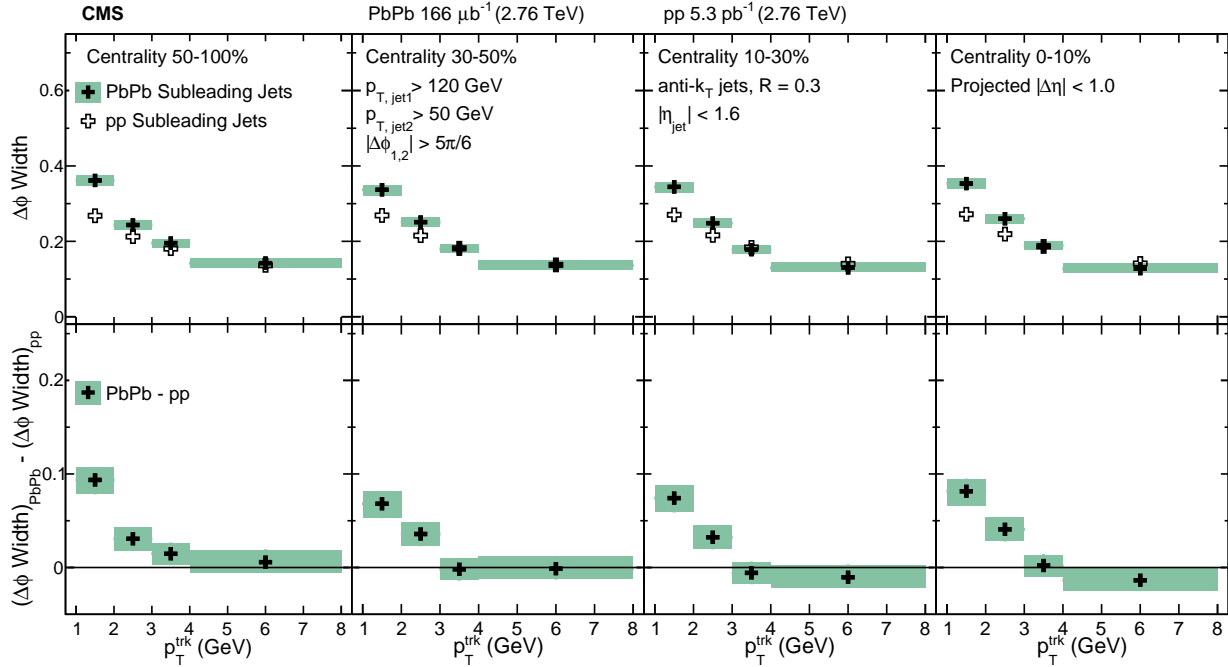


Figure 44. Comparison of the widths in PbPb and pp of the $\Delta\phi$ charged-particle distributions correlated to leading jets with $p_{T,\text{jet}2} > 50$ GeV, as a function of p_T^{trk} . The bottom row shows the difference of the widths in PbPb and pp data. The shaded band corresponds to systematic uncertainty, and statistical uncertainties are smaller than symbol size.

959 **8.3 Jet shapes**

960 A common observable to characterize and compare the widths of jet peaks is the jet shape $\rho_{\Delta r}$,
 961 measuring the fraction of total jet transverse momentum as a function of distance Δr from the jet
 962 axis. As discussed in Sec. 2.4, previous CMS measurements of jet shape [13] have gained particular
 963 attention from the theoretical community in efforts to constrain models of jet energy loss. Jet shape
 964 measurements to large angles ($\Delta r = 1$, compared to previous measurements to only $\Delta r = 0.3$) may
 965 be obtained from correlation studies, extending measurements to the full range of the jet peak
 966 and offering the capability of distinguishing between theoretical predictions based on earlier, more
 967 narrow, measurements.

968 In the correlation technique, jet shapes are obtained by weighting correlations by p_T^{trk} , and
 969 integrating the resulting (background-subtracted) 2D jet-peak momentum distributions in annuli
 970 with radial width $\Delta r = 0.05$, where each has an inner radius of $r_a = \Delta r - \delta r/2$ and an outer radius
 971 of $r_b = \Delta r + \delta r/2$. For this measurement, an inclusive high- p_T^{trk} bin is included to capture particles
 972 with $20 < p_T^{\text{trk}} < 300$ GeV. The resulting transverse momentum profile of the jet is defined as:

$$P(\Delta r) = \frac{1}{\delta r} \frac{1}{N_{\text{jets}}} \sum_{\text{jets}} \sum_{\text{tracks} \in (r_a, r_b)} p_T^{\text{trk}} \quad (9)$$

973 This profile is then normalized to unity within $\Delta r = 1$ to produce the jet shape $\rho(\Delta r)$:

$$\rho(\Delta r) = \frac{1}{\delta r} \frac{\sum_{\text{jets}} \sum_{\text{tracks} \in (r_a, r_b)} p_T^{\text{trk}}}{\sum_{\text{jets}} \sum_{\text{tracks}} p_T^{\text{trk}}} \quad (10)$$

974 The top row of Fig. 45 presents the inclusive jet transverse momentum profile $P(\Delta r)$ in pp
 975 and PbPb data at 5.02 TeV, while the middle row shows the jet shape $\rho(\Delta r)$, normalized to unity
 976 within $\Delta r = 1$. Here again redistribution of energy from small to large angles from the jet cone is
 977 evident in PbPb relative to pp reference, as seen in the dipping then rising trend in the jet shape
 978 ratio $\rho(\Delta r)_{\text{PbPb}}/\rho(\Delta r)_{\text{pp}}$ presented in the bottom row.

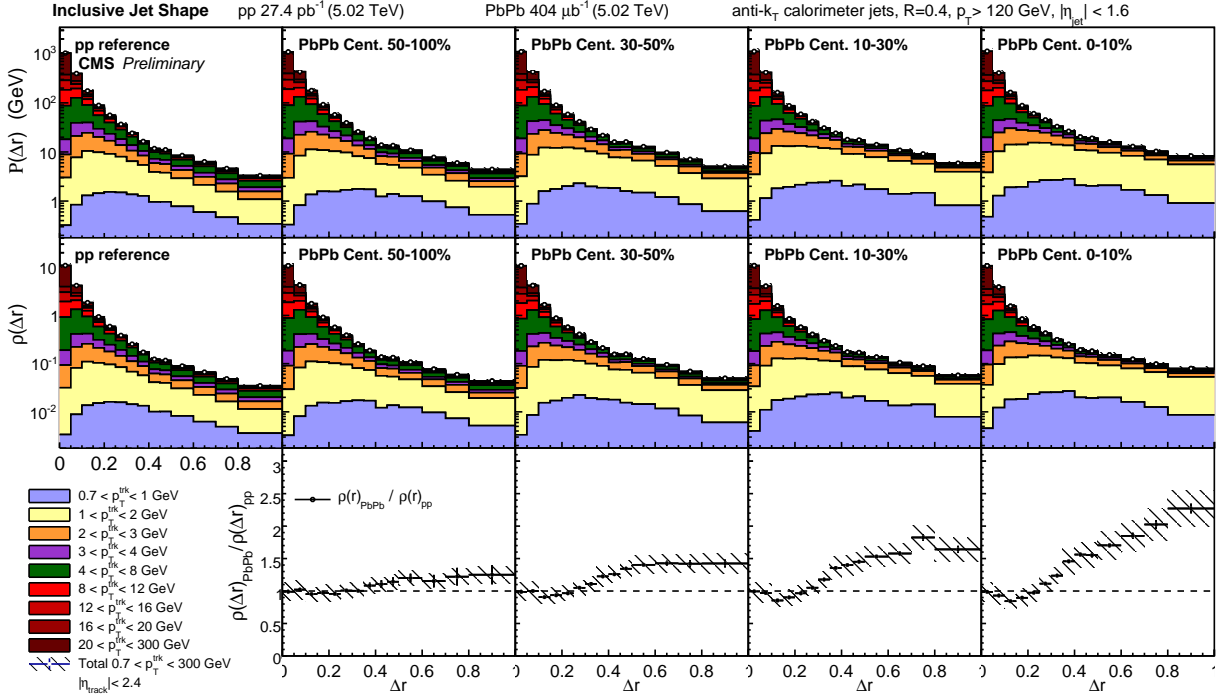


Figure 45. Top row: Transverse momentum profile of inclusive jets $P(\Delta r)$ in pp and PbPb data at 5.02 TeV, shown differentially in p_T^{trk} . Middle row: jet shapes $\rho(\Delta r)$ (normalized to unity over $\Delta r < 1$) in PbPb and pp. Bottom row: jet shape ratio $\rho(\Delta r)_{\text{PbPb}}/\rho(\Delta r)_{\text{pp}}$. Hatched lines on p_T^{trk} -inclusive points show total systematic uncertainties.

In addition to studies of inclusive jet shapes, it is also interesting to consider the jet shapes and jet shape modifications of leading and subleading jets in dijet events. These studies are carried out with the same selection of 2.76 TeV dijet events used for the correlation studies presented in 8.2. In this case, for consistency with a previous CMS study measured the jet shape $\rho(\Delta r)$ within the jet cone radius $\Delta r = 0.3$ [13] at 2.76 TeV, these leading and subleading jet shape measurements at 2.76 TeV are normalized to integrate to unity with in the radius $\Delta r < 0.3$. In Fig. 46, the leading jet shape measured with this correlation technique is compared to the published CMS reference and extend this measurement to $\Delta r = 1$, noting that the leading jet shape is consistent within uncertainties with the previous measurement for an inclusive jet selection of all jets with $p_T > 100$ GeV. A new measurement of subleading jet shape in Fig. 47 is then presented. As noted in the correlation width measurements discussed in Sec. 8.2, subleading jets in pp data are broader than leading jets in pp data. Therefore, although the PbPb-to-pp *modifications* are similar for leading and subleading jets, the more steeply falling pp leading jet shape results in a greater *relative*

modification shown in the jet shape ratio $\rho_{\text{PbPb}}(\Delta r)/\rho_{\text{pp}}(\Delta r)$ for leading than for subleading jets.
 Similarly, when comparing jet shape measurements at 2.76 TeV to those at 5.02 TeV, it is relevant
 to note that the pp reference is broader at 5.02 TeV than at 2.76 TeV, likely due to the greater
 fraction of gluon versus quark jets that pass the kinematic selections of the analysis at the higher
 center-of-mass energy.

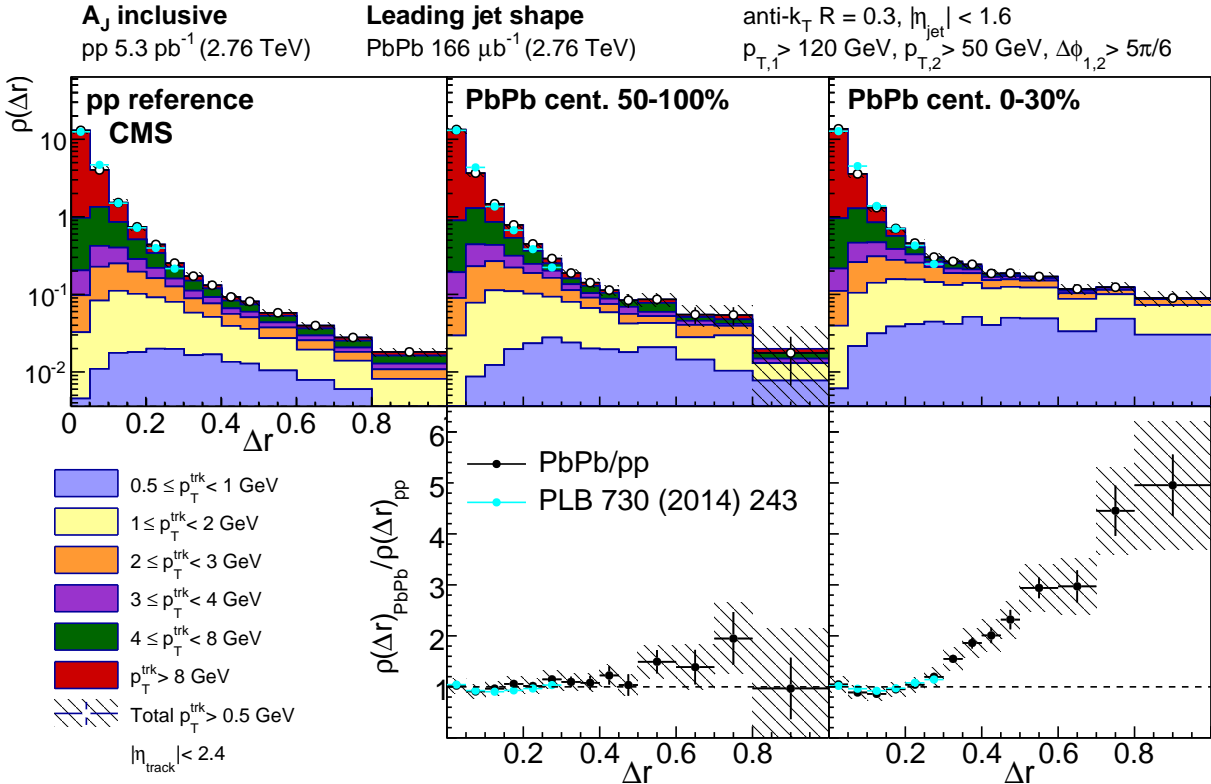


Figure 46. Top row: leading jet shape $\rho(\Delta r)$ for pp reference and central and peripheral PbPb data, shown for all tracks with $p_{T}^{\text{trk}} > 0.5 \text{ GeV}$ and decomposed by track transverse momentum. Shapes are normalized to unity over the region $r < 0.3$ for consistency with the published reference shown (Ref. [13]). Bottom row: leading jet shape ratio $\rho(\Delta r)_{\text{PbPb}}/\rho(\Delta r)_{\text{pp}}$, again with published reference.

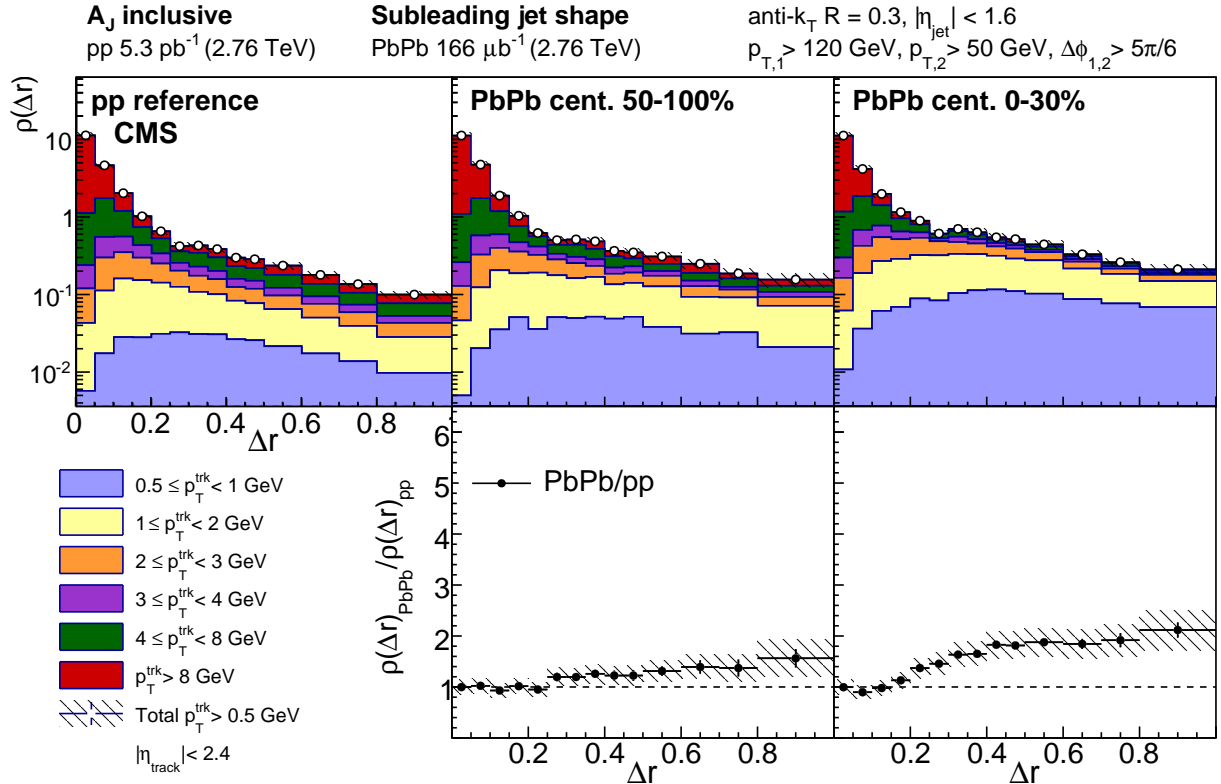


Figure 47. Top row: subleading jet shape $\rho(\Delta r)$ for pp reference and central and peripheral PbPb data, shown for all tracks with $p_T > 0.5$ GeV and decomposed by track transverse momentum, normalized to unity over the region $\Delta r < 0.3$. Bottom row: subleading jet shape ratio $\rho(\Delta r)_{\text{PbPb}} / \rho(\Delta r)_{\text{pp}}$.

997 **8.4 Decomposition of hemisphere momentum balance in dijet events**

998 The dijet results at 2.76 TeV presented in this analysis are complimented by other CMS measure-
999 ments conducted on the same data using the “missing- p_T ” hemisphere momentum balance method
1000 presented in Ref. [19] and discussed in Secs. 2.3 and 2.4. In this analysis, a “dijet” axis is con-
1001 structed by averaging the leading jet and subleading jet axes (these are separated by $\Delta\phi_{1,2} = \pi$ on
1002 average, but are not necessarily parallel in each event due to 3-jet events) to construct a dijet axis,
1003 dividing the event into leading and subleading hemispheres with respect to this axis, and comparing
1004 the hemisphere-wide distributions of p_T^{trk} (projected, in this case, onto the combined dijet axis) to
1005 obtain the subleading-to-leading balancing distribution as a function of distance from the dijet axis
1006 Δr . The jet track correlation technique may be used to obtain this same measurement (comparing
1007 subleading-to-leading distributions on average rather than event-by-event, and making use of the
1008 fact that the subleading and leading jet axes are *on average* perfectly back-to-back). When this
1009 cross-check is performed *without background subtraction*, the two techniques yield consistent results,
1010 despite methodological differences and differences in jet- η cuts. This hemisphere-wide missing- p_T
1011 technique is also used to extract differences in total particle yields between the leading and sublead-
1012 ing hemispheres, and shows an average excess of 4–5 particles with p_T^{trk} in the subleading hemisphere
1013 compared to the leading hemisphere [19]. In the dijet correlation studies presented in this analysis
1014 *with background subtraction*, however, only approximately 2 additional particles were found cor-
1015 related to the subleading jet peak compared to the leading jet peak, as shown in Sec. 8.2. This
1016 apparent difference motivates a detailed examination and decomposition of the distribution of p_T^{trk}
1017 in dijet events in order to consider contributions to the hemisphere-wide momentum balance from
1018 both the leading and subleading jet peaks, and from the long-range correlated underlying event.

1019 For this investigation, the dijet samples of 2.76 TeV PbPb and pp data are each divided
1020 based on asymmetry parameter A_J to further illuminate quenching effects and to decompose the
1021 contributions to the hemisphere p_T^{trk} balance studied in Ref. [19]: a balanced sample with $A_J < 0.22$,
1022 and an “unbalanced” sample with $A_J > 0.22$. Transverse momentum distributions for each sample
1023 are constructed in $\Delta\eta - \Delta\phi$ for each sample, and are corrected for pair-acceptance effects. Like all
1024 particle density and p_T^{trk} correlations studied in this analysis, these show jet peaks on an underlying
1025 event that shows significant $\Delta\phi$ correlations but is flat in $\Delta\eta$. Correlations are therefore projected

1026 into $\Delta\phi$ for further study in order to preserve this underlying event structure. Studies will begin
1027 by considering the hemisphere-wide “missing- p_T ” distribution as a function of $\Delta\phi$, and will then
1028 decompose this distribution into jet peak and underlying event contributions, and finally consider
1029 the relative contributions from jet peaks and from the underlying event to the overall hemisphere
1030 p_T^{trk} balance for balanced and unbalanced dijets.

1031 Figures 48 and 49 present the hemisphere-wide balancing distribution of transverse momen-
1032 tum around the subleading versus the leading jet for balanced and unbalanced dijets respectively.
1033 For both selections, a wide excess of soft particles in the subleading versus leading hemisphere in
1034 central PbPb collisions relative to pp reference is evident, reflecting the greater quenching of the
1035 subleading jet. In the unbalanced selection, as required by momentum conservation, the signal is
1036 enhanced in both pp and PbPb data: in pp a large excess of particles with $p_T > 3$ GeV long-range
1037 is present on the subleading side, compensating for the lower momentum of the highest- p_T particles
1038 in the jet itself. In peripheral PbPb data the distribution is quite similar to pp reference, while
1039 in central PbPb data this balancing distribution consists mostly of soft particles $p_T < 3$ GeV,
1040 consistent with the findings of a previous CMS study [19]. To better demonstrate these medium
1041 modifications, the difference in yield between PbPb and pp collisions is shown in the bottom panels
1042 of Fig. 48 and Fig. 49.

1043 To better understand the redistribution of transverse momentum within the QGP, the
1044 distributions are then separated into three components as discussed above: the gaussian-like peaks
1045 about the leading and subleading jet axes, plus a component accounting for overall subleading-
1046 to-leading asymmetry in the $\Delta\phi$ -correlated long-range underlying event (measured in the region
1047 $1.5 < |\Delta\eta| < 2.5$). In Fig. 50 and Fig. 51, the jet peak components are shown for balanced and
1048 unbalanced jets respectively, presenting subleading results positive and leading results negative (in
1049 line with the hemisphere difference measurements in Fig. 49 and Fig. 48). Jet peak distributions
1050 after decomposition are projected over the full range $|\Delta\eta| < 2.5$, again for consistency with the
1051 hemisphere difference measurements. The top row of each panel first shows the overall distribution
1052 of momentum carried by particles with $p_T < 8$ GeV on about the jet peak. The middle two panels
1053 then assess modifications to the subleading and leading jets respectively. Here there is evidence
1054 of quenching to both the subleading and the leading jet in central PbPb collisions relative to pp
1055 reference, with an excess of low- p_T^{trk} particles correlated to the jet axis in both the balanced and

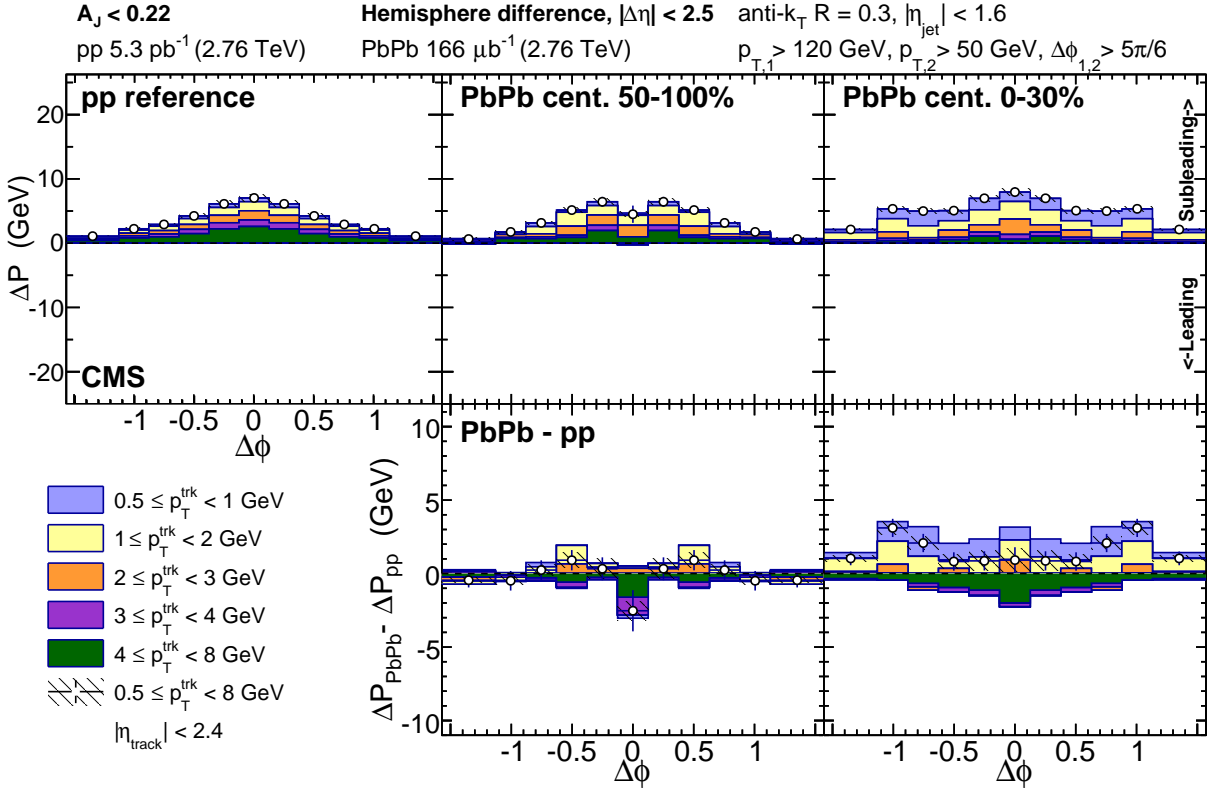


Figure 48. Top row: total hemisphere distribution in $\Delta\phi$ of excess transverse momentum about the subleading relative to the leading jet for balanced dijets with $A_J < 0.22$, shown differentially by track transverse momentum for pp reference, peripheral PbPb, and central PbPb data. Bottom row: PbPb–pp difference in these $\Delta\phi$ momentum distributions.

1056 unbalanced dijet selections, as observed in the charged particle density studies presented in Sec. 8.2.
 1057 In unbalanced dijets this enhancement of soft- p_T^{trk} particles turns into a depletion at higher- p_T^{trk} , and
 1058 is greater on the subleading than the leading side. To compare between hemispheres and assess the
 1059 jet peak contribution to the overall hemisphere momentum balance, the double difference PbPb–pp,
 1060 subleading–leading is presented in the bottom panel. Here it is evident that the low- p_T^{trk} excess
 1061 in central PbPb collisions is larger on the subleading than the leading side of the dijet system,
 1062 but larger subleading-to-leading excess only accounts for only a portion of the total momentum
 1063 redistribution in unbalanced dijet events.

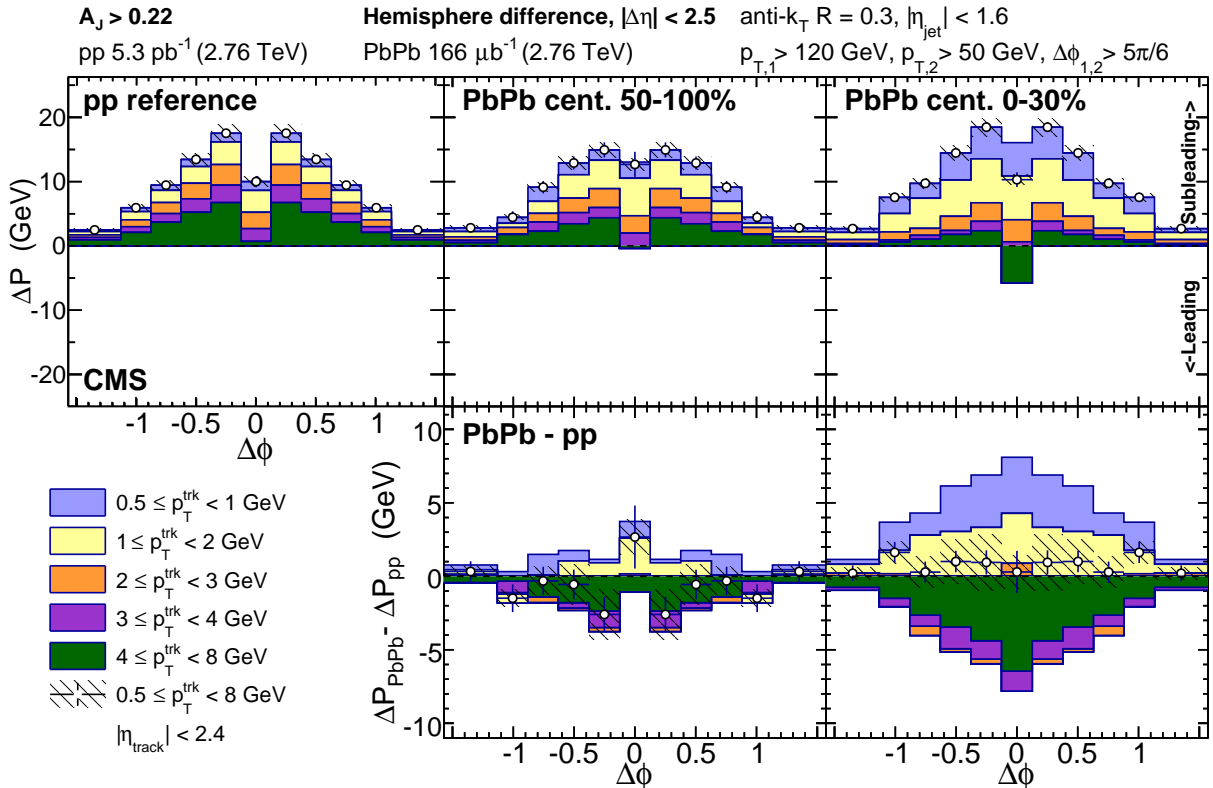


Figure 49. Top row: total hemisphere distribution in $\Delta\phi$ of excess transverse momentum about the subleading relative to the leading jet for balanced dijets with $A_J > 0.22$, shown differentially by track transverse momentum for pp reference, peripheral PbPb, and central PbPb data. Bottom row: PbPb-pp difference in these $\Delta\phi$ momentum distributions.

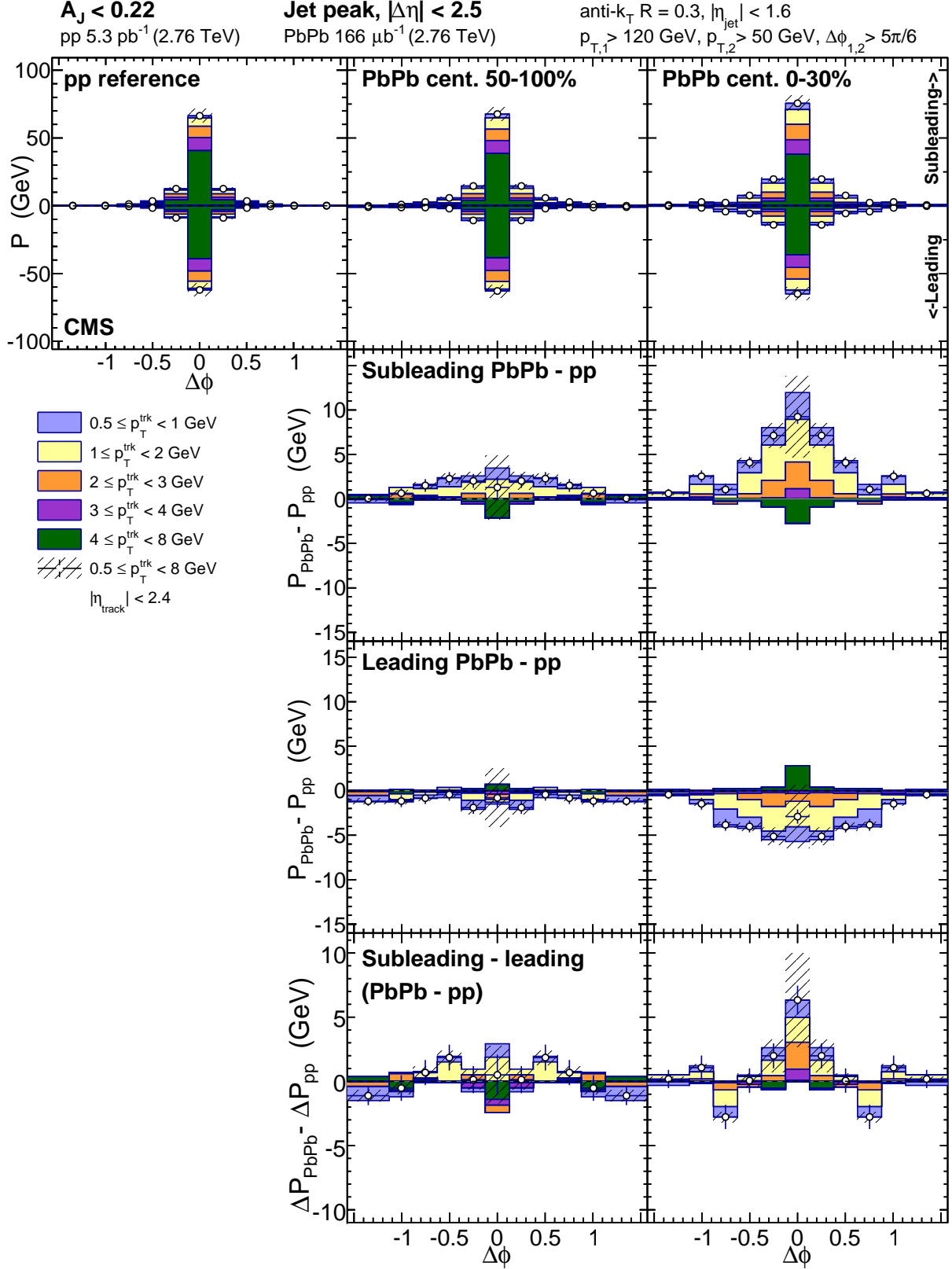


Figure 50. Top row: jet-peak (long-range subtracted) distribution in $\Delta\phi$ of transverse momentum about the subleading (plotted positive) and leading (plotted negative) jets for balanced dijets with $A_J < 0.22$. Middle rows: PbPb–pp momentum distribution differences for subleading and leading jets. Bottom row: PbPb–pp, subleading–leading double difference in these $\Delta\phi$ momentum distributions.

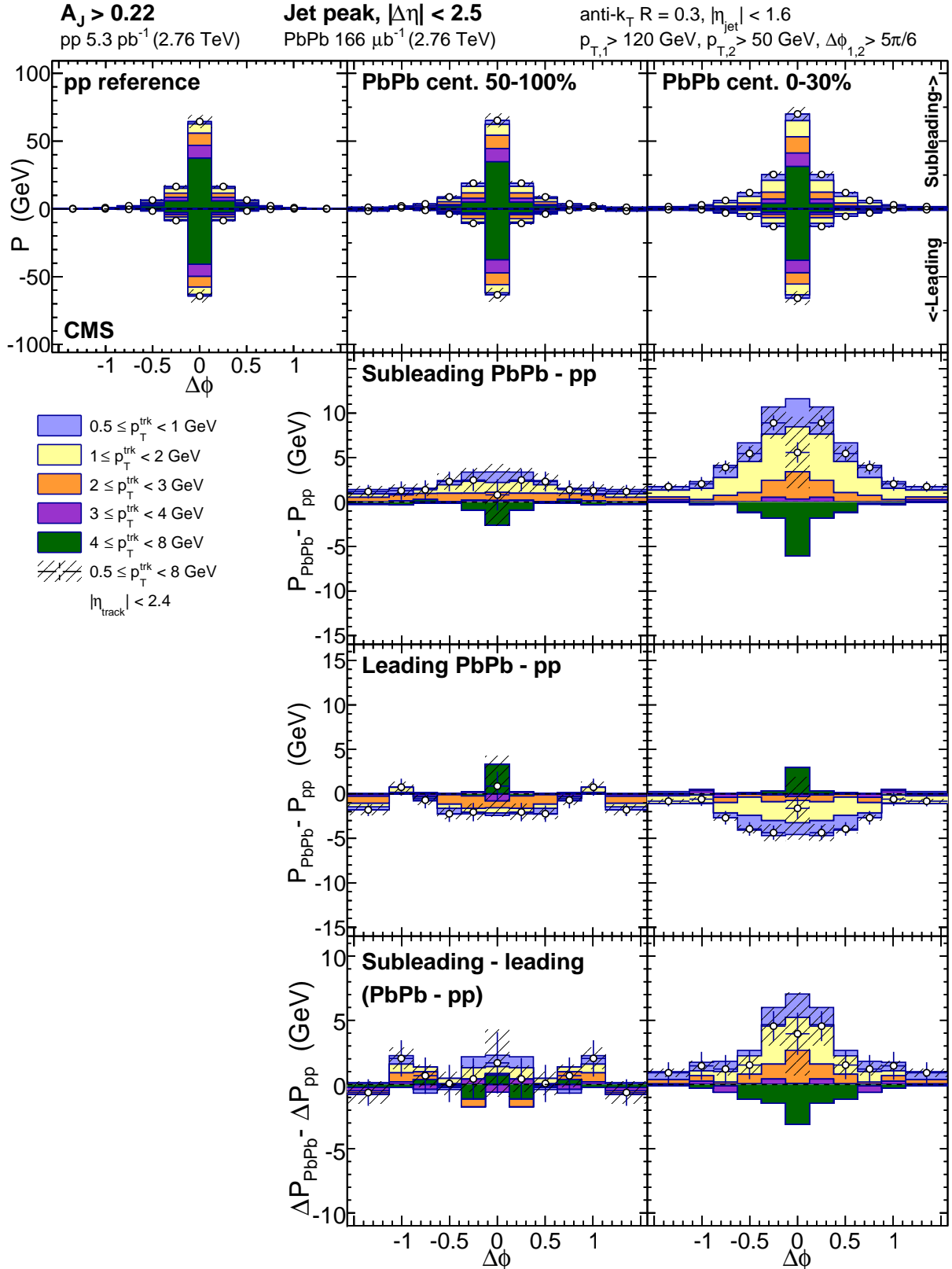


Figure 51. Top row: jet-peak (long-range subtracted) distribution in $\Delta\phi$ of transverse momentum about the subleading (plotted positive) and leading (plotted negative) jets for balanced dijets with $A_J > 0.22$. Middle rows: PbPb-pp momentum distribution differences for subleading and leading jets. Bottom row: PbPb-pp, subleading-leading double difference in these $\Delta\phi$ momentum distributions.

These jet-related studies are complemented by an analysis of the long-range subleading to leading asymmetry, presented in Fig. 52 and Fig. 53 for balanced and unbalanced jets respectively. The long-range correlated background in balanced dijet events is symmetric in pp and peripheral PbPb data, while in central PbPb data there is a small excess of low- p_T^{trk} particles. In unbalanced dijets, however, there is significant asymmetry already in pp reference, with a large correlated excess of particles in all p_T classes less than 8 GeV on the subleading relative to leading side of the underlying event. This asymmetry reflects the presence of other hard-scattering products in the subleading hemisphere dijet event, as required by momentum conservation when selecting asymmetric dijets in vacuum-like collisions. In the presence of the strongly interacting medium; however, this underlying event asymmetry in asymmetric dijet events changes notably. In peripheral PbPb collisions there is already some depletion of momentum carried by high- p_T^{trk} particles, and in central pp collisions subleading-to-leading underlying event excesses with $p_T^{\text{trk}} > 2$ GeV vanish nearly completely. To assess the contribution of this long-range asymmetry to the total hemisphere imbalance, the double difference PbPb–pp, subleading–leading is plotted on the bottom panel as for (and on the same scale as) the double difference shown for the jet peaks. To assess the overall hemisphere momentum balance attributed to this long-range asymmetry, the hemisphere integral ($|\Delta\phi| < \pi/2$ and $|\Delta\eta| < 2.5$) is presented in Fig. 54 for balanced versus unbalanced dijets. For unbalanced dijets, the the overall asymmetry rises with track- p_T pp reference, but falls with track- p_T for central PbPb data.

Finally, to show the relative contributions to overall hemisphere momentum balance from the leading and subleading jet peaks as well as from the long-range underlying event asymmetry, a summary of hemisphere-integrated excess (PbPb–pp) yield for balanced and unbalanced dijets in central PbPb collisions is shown in Fig. 55 and Fig. 56 for central and peripheral collisions respectively. The top panels of Fig. 55 present total PbPb minus pp differences in transverse momentum associated with the subleading jet (plotted positive) and leading jet (plotted negative). Modifications to the distribution of tracks with $p_T < 3$ GeV are evident for both the leading and subleading jet peaks, with a greater enhancement of low- p_T^{trk} particles associated with the subleading jet. These total jet peak modifications in central PbPb collisions are not significantly different in unbalanced versus balanced dijets. The bottom panels of Fig. 55 present these jet-peak modifications together with the long-range modifications evident in Fig. 54 to show the decomposed

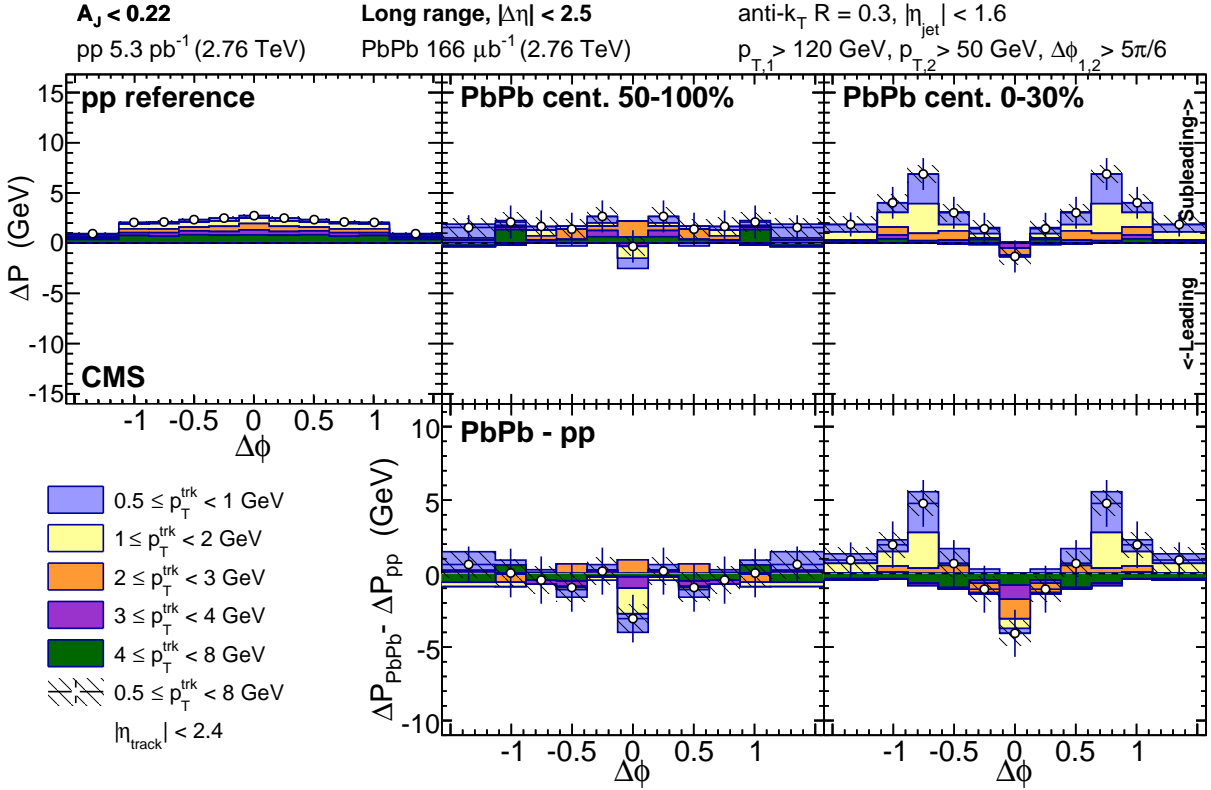


Figure 52. Top row: long-range distribution in $\Delta\phi$ of excess transverse momentum in the subleading relative to leading sides for balanced dijets with $A_J < 0.22$. Bottom row: PbPb–pp difference in these $\Delta\phi$ long-range momentum distributions.

hemisphere-wide differences in associated transverse momentum in each p_T^{trk} range. Unlike the jet peak contributions, the long-range PbPb versus modifications differ outside of uncertainties between balanced and unbalanced dijets: here the depletion of high- p_T^{trk} particles in unbalanced PbPb versus pp dijets corresponds to the reduced contribution from third jets (which are prominently evident in the long-range distribution for pp unbalanced dijet events) in central PbPb unbalanced dijet events. Figure 56 presents the same hemisphere-integrated PbPb minus pp excess information for peripheral collisions for comparison to the central results shown in Fig. 55. Some possible small modifications are already evident in this 50-100% centrality range, but these differences between peripheral PbPb and pp results are in most cases smaller than systematic uncertainties.

The decomposition of integrated jet peak and long-range correlated p_T^{trk} shown in Fig. 55 and Fig. 56 clarify the relationship between the jet peak correlation studies presented in this analysis and the missing- p_T measurements presented in Ref. [19]: as shown through this detailed decom-

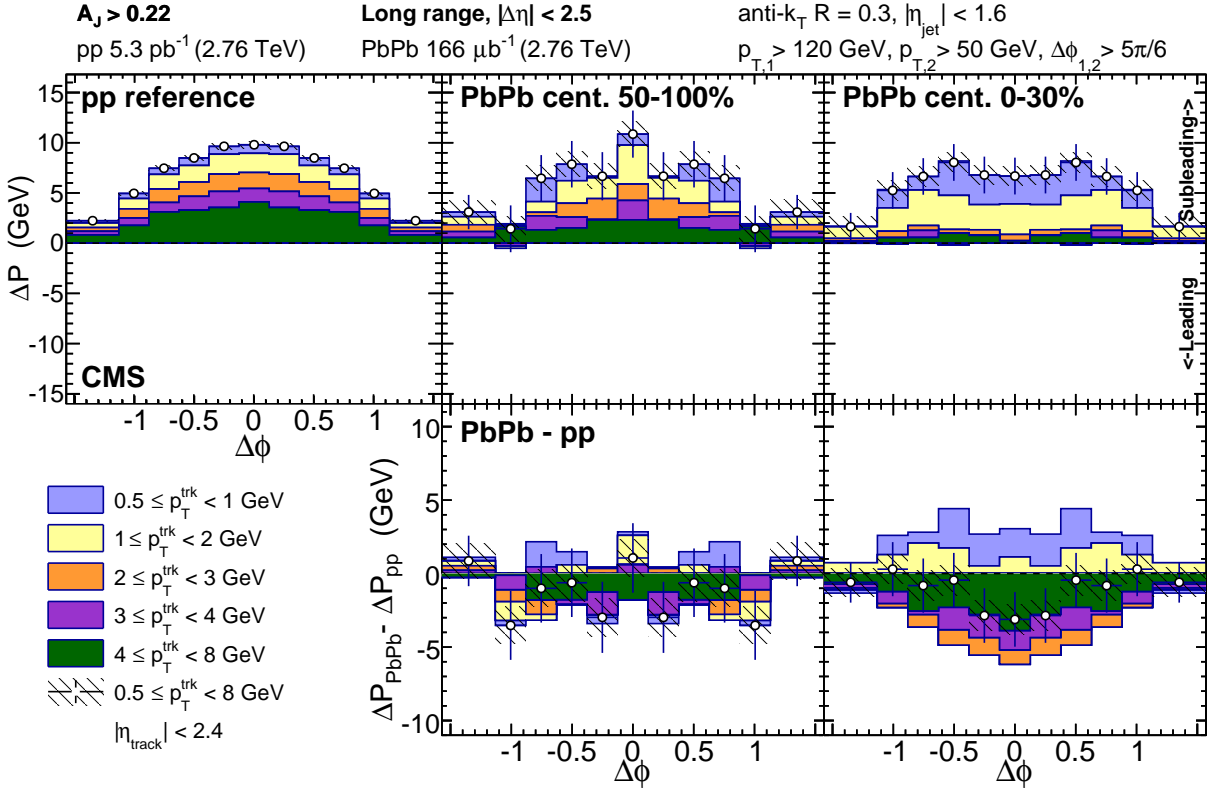


Figure 53. Top row: long-range distribution in $\Delta\phi$ of excess tranverse momentum in the subleading relative to leading sides for balanced dijets with $A_J > 0.22$. Bottom row: PbPb–pp difference in these $\Delta\phi$ long-range momentum distributions.

position, comparing hemisphere distributions as a whole include contributions from the subleading and leading jet peaks studied in correlation studies, but also a contribution from the underlying event. In both PbPb and pp data, the underlying event partially cancels with hemisphere subtraction: contributions from combinatoric background and even flow harmonics (V_2 etc.) will cancel, while contributions from 3rd jets and odd flow harmonics (V_1 etc.) will not. As we have seen, in pp the non-cancelling underlying event is dominated by 3rd jets, especially in the unbalanced dijet selection in which their presence is kinematically required. In PbPb, this underlying event has evident contributions from odd flow harmonics as well, reflecting coupling of jets to the event reaction plane.

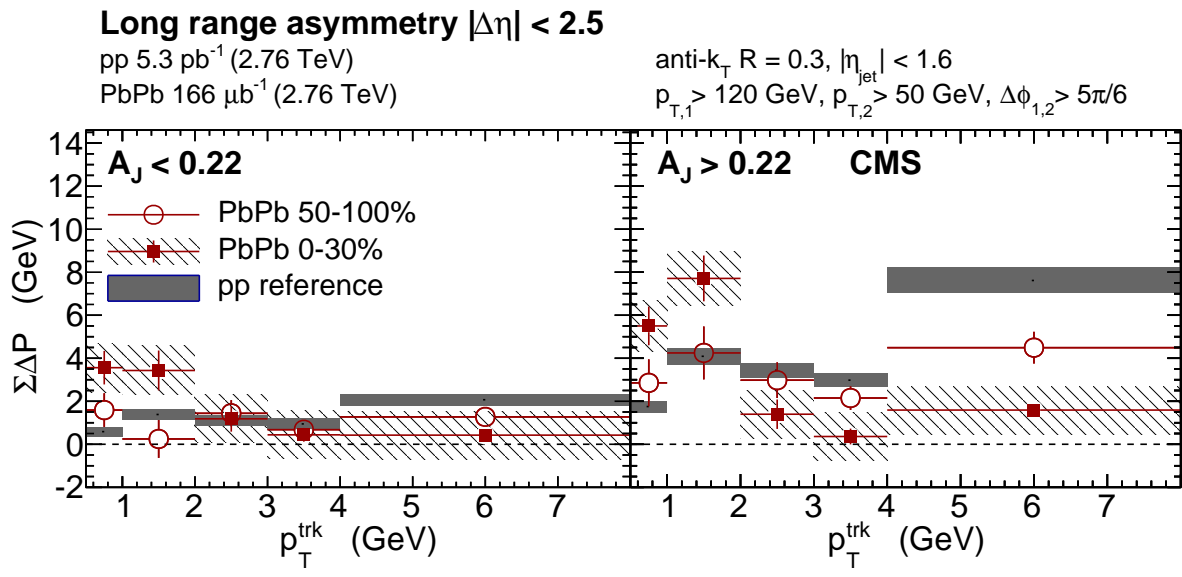


Figure 54. Integrated transverse momentum in the long-range $\Delta\phi$ -correlated distribution as a function of track- p_T integrated over $|\Delta\phi| < \pi/2$ and $|\Delta\eta| < 2.5$ and for pp reference, peripheral PbPb and central PbPb data for balanced compared to unbalanced dijets.

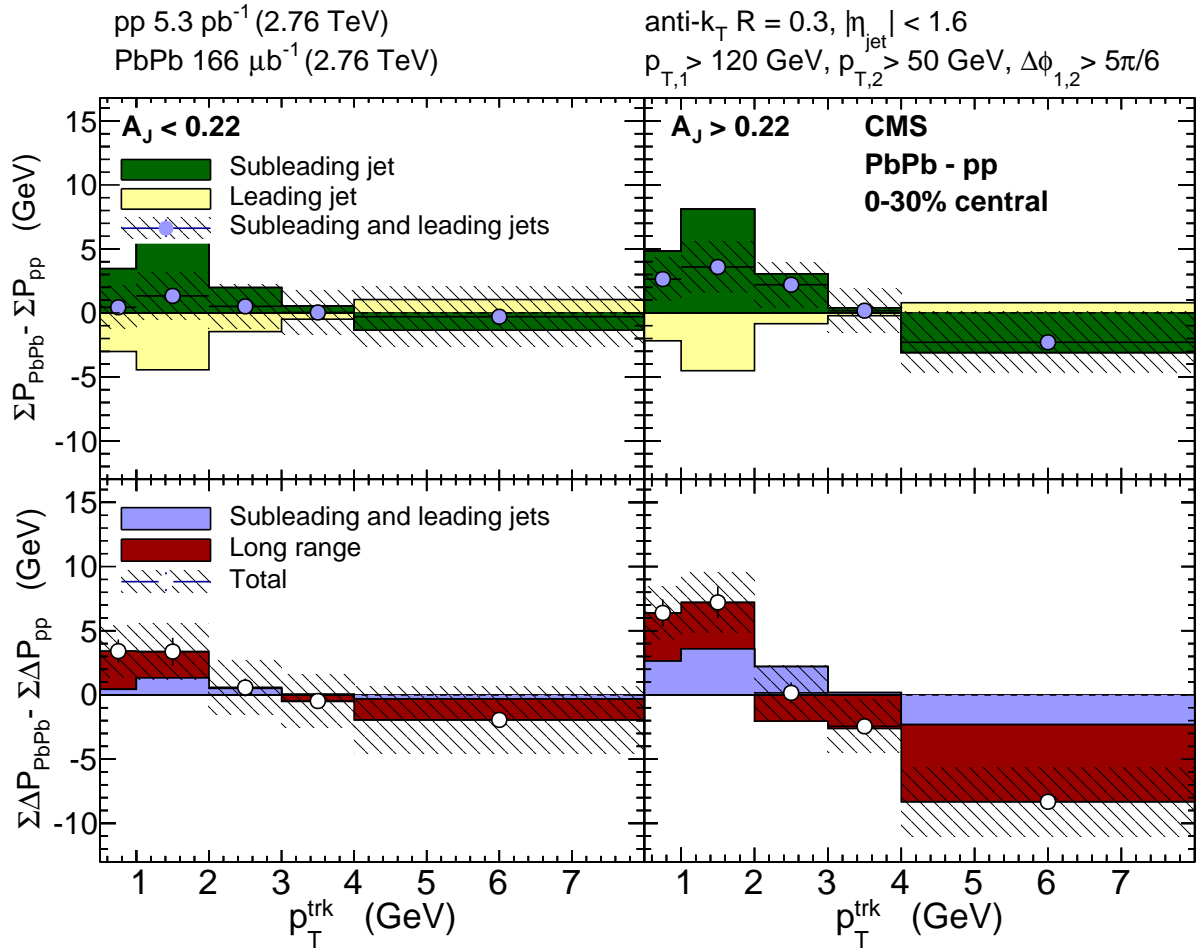


Figure 55. Modifications of jet-hadron correlated transverse momentum in central PbPb collisions with respect to pp reference, integrated $|\Delta\phi| < \pi/2$, $|\Delta\phi| < 2.5$. Top row: subleading and leading jet peak PbPb-pp. Bottom row: relative contributions from jet peaks and long-range asymmetry to the double difference PbPb-pp, subleading-leading in total hemisphere transverse momentum.

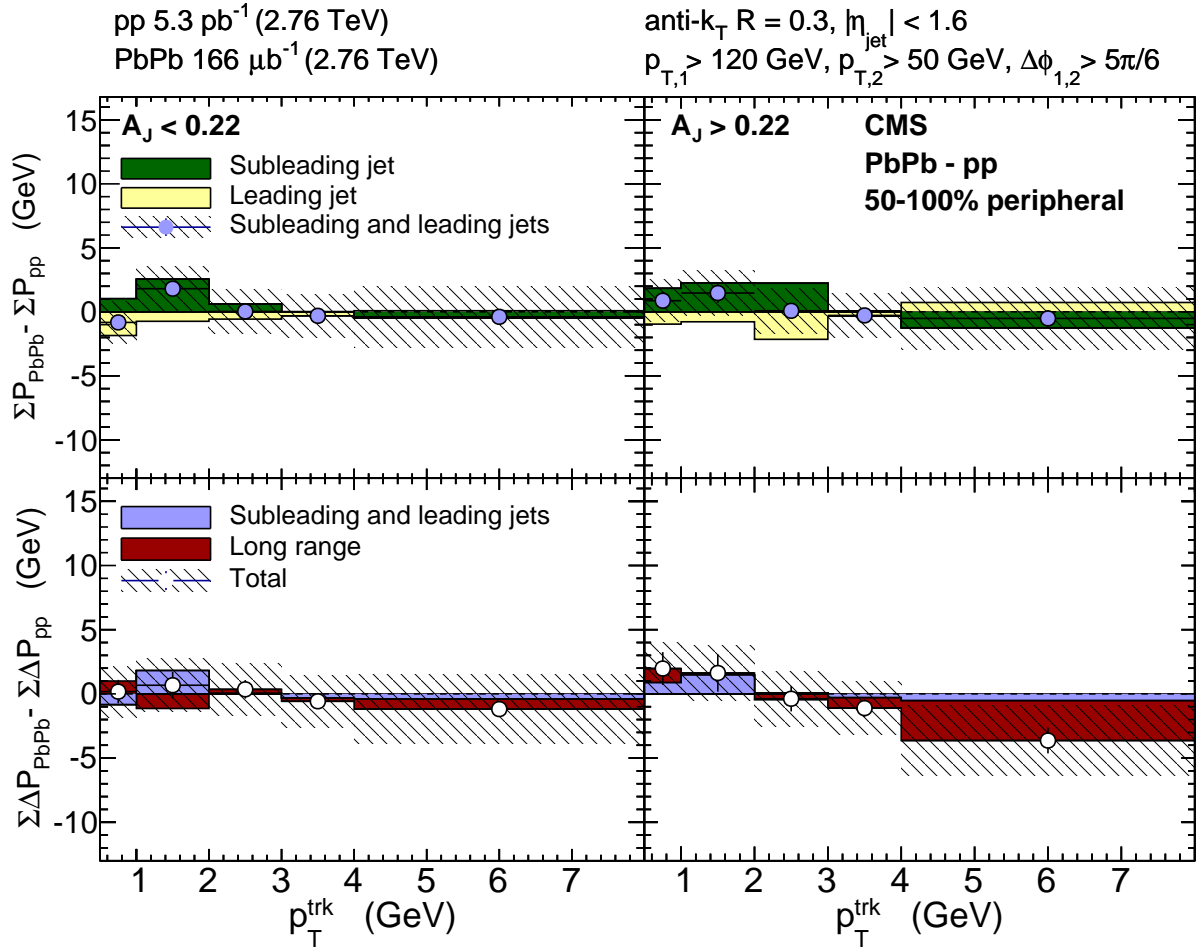


Figure 56. Modifications of jet-hadron correlated transverse momentum in peripheral PbPb collisions with respect to pp reference, integrated $|\Delta\phi| < \pi/2$, $|\Delta\phi| < 2.5$. Top row: subleading and leading jet peak PbPb-pp. Bottom row: relative contributions from jet peaks and long-range asymmetry to the double difference PbPb-pp, subleading-leading in total hemisphere transverse momentum.

1115 **8.5 Theory implications of these results**

9 CONCLUSION

REFERENCES

- 1118 [1] K. Aamodt et al. Harmonic decomposition of two-particle angular correlations in Pb-Pb
1119 collisions at $\sqrt{s_{\text{NN}}} = 2.76$ TeV. *Phys. Lett. B*, 708:249, 2012.
- 1120 [2] S. Agostinelli et al. GEANT4—a simulation toolkit. *Nucl. Instrum. and Methods A*, 506:250,
1121 2003.
- 1122 [3] M. Cacciari, G. P. Salam, and G. Soyez. The anti- k_t jet clustering algorithm. *JHEP*, 04:063,
1123 2008.
- 1124 [4] M. Cacciari, G. P. Salam, and G. Soyez. FastJet user manual. *Eur. Phys. J. C*, 72:1896, 2012.
- 1125 [5] S. Chatrchyan et al. The CMS experiment at the CERN LHC. *JINST*, 3:S08004, 2008.
- 1126 [6] S. Chatrchyan et al. Long-range and short-range dihadron angular correlations in central PbPb
1127 collisions at a nucleon-nucleon center of mass energy of 2.76 TeV. *JHEP*, 07:076, 2011.
- 1128 [7] S. Chatrchyan et al. Observation and studies of jet quenching in PbPb collisions at $\sqrt{s_{\text{NN}}} =$
1129 2.76 TeV. *Phys. Rev. C*, 84:024906, 2011.
- 1130 [8] S. Chatrchyan et al. Azimuthal anisotropy of charge particles at high transverse momenta in
1131 pb-pb collisions at $\sqrt{s_{\text{NN}}} = 2.76$ TeV. *Phys. Rev. Lett.*, 109:022301, 2012.
- 1132 [9] S. Chatrchyan et al. Centrality dependence of dihadron correlations and azimuthal anisotropy
1133 harmonics in PbPb collisions at $\sqrt{s_{\text{NN}}} = 2.76$ TeV. *Eur. Phys. J.*, C72:2012, 2012.
- 1134 [10] S. Chatrchyan et al. Measurement of jet fragmentation into charged particles in pp and PbPb
1135 collisions at $\sqrt{s_{\text{NN}}} = 2.76$ TeV. *JHEP*, 10:087, 2012.
- 1136 [11] S. Chatrchyan et al. Studies of jet quenching using isolated-photon+jet correlations in PbPb
1137 and pp collisions at $\sqrt{s_{\text{NN}}} = 2.76$ TeV. *Phys. Lett. B*, 718:773, 2013.
- 1138 [12] S. Chatrchyan et al. Description and performance of track and primary-vertex reconstruction
1139 with the CMS tracker. *JINST*, 9(10):P10009, 2014.
- 1140 [13] S. Chatrchyan et al. Modification of jet shapes in PbPb collisions at $\sqrt{s_{\text{NN}}} = 2.76$ TeV. *Phys.*
1141 *Lett. B*, 730:243, 2014.

- 1142 [14] CMS. Identification and Filtering of Uncharacteristic Noise in the CMS Hadron Calorimeter.
1143 *JINST*, 5:T03014, 2010.
- 1144 [15] C. Collaboration. Momentum flow relative to dijets in pbpb collisions at 2.76 tev. *CMS*
1145 *Analysis Note (Internal)*, AN-14-024, 2014.
- 1146 [16] L. Evans and P. Bryant. LHC Machine. *JINST*, 3:S08001, 2008.
- 1147 [17] C. Internal. Study of high- p_t charged particle suppression in pbpb compared to pp collisions
1148 at 5.02 tev. 2016.
- 1149 [18] V. Khachatryan et al. Performance of photon reconstruction and identification with the CMS
1150 detector in proton-proton collisions at $\sqrt{s_{\text{NN}}} = 8$ TeV. *JINST*, 10:P08010, 2015.
- 1151 [19] V. Khachatryan et al. Measurement of transverse momentum relative to dijet systems in PbPb
1152 and pp collisions at $\sqrt{s_{\text{NN}}} = 2.76$ TeV. *JHEP*, 01:6, 2016.
- 1153 [20] V. Khachatryan et al. The CMS trigger system. *JINST*, 12:P01020, 2017.
- 1154 [21] O. Kodolova, I. Vardanian, A. Nikitenko, and A. Oulianov. The performance of the jet iden-
1155 tification and reconstruction in heavy ions collisions with CMS detector. *Eur. Phys. J. C*,
1156 50:117, 2007.
- 1157 [22] I. P. Lokhtin and A. M. Snigirev. A model of jet quenching in ultrarelativistic heavy ion
1158 collisions and high- p_T hadron spectra at RHIC. *Eur. Phys. J. C*, 45:211, 2006.
- 1159 [23] G. P. Salam. Towards Jetography. *Eur. Phys. J.*, C67:637–686, 2010.
- 1160 [24] T. Sjöstrand, S. Mrenna, and P. Skands. PYTHIA 6.4 physics and manual. *JHEP*, 05:026,
1161 2006.

APPENDICES

1163 A Jet kinematics

1164 The following sections summarize jet kinematics for inclusive jets and dijets at 2.76 TeV, for inclu-
 1165 sive jets at 5.02 TeV, and for dijets in each asymmetry class at 2.76 TeV.

1166 A.1 Jet kinematics at 2.76 TeV

1167 The kinematic observables of jets in pp and PbPb 2.76 TeV events (solid markers) are compared
 1168 with Monte Carlo (hatched marks). All spectra have been normalized to unity. Comparing the jet
 1169 spectra observed in PbPb data (pp data) and in PYTHIA+HYDJET (PYTHIA) samples, a reasonable
 1170 agreement in the overall shape is found.

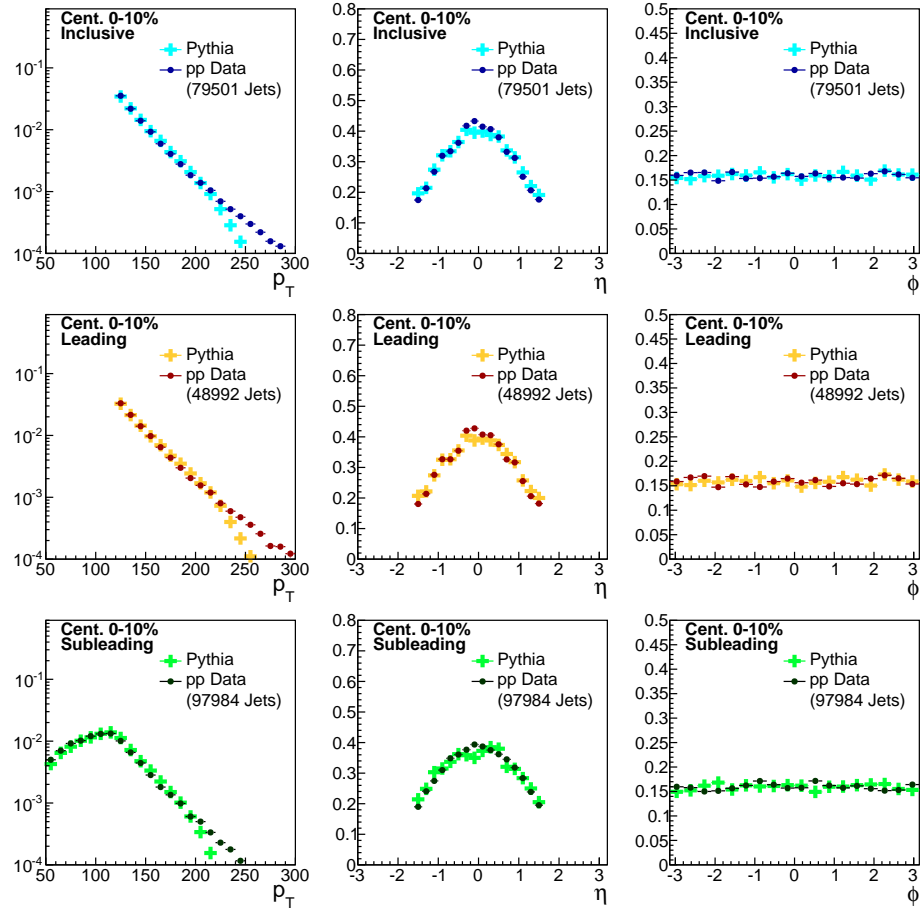


Figure 57. Distribution of transverse momentum, pseudorapidity, and azimuthal distribution of all jet selections for Pythia data compared to PYTHIA simulation.

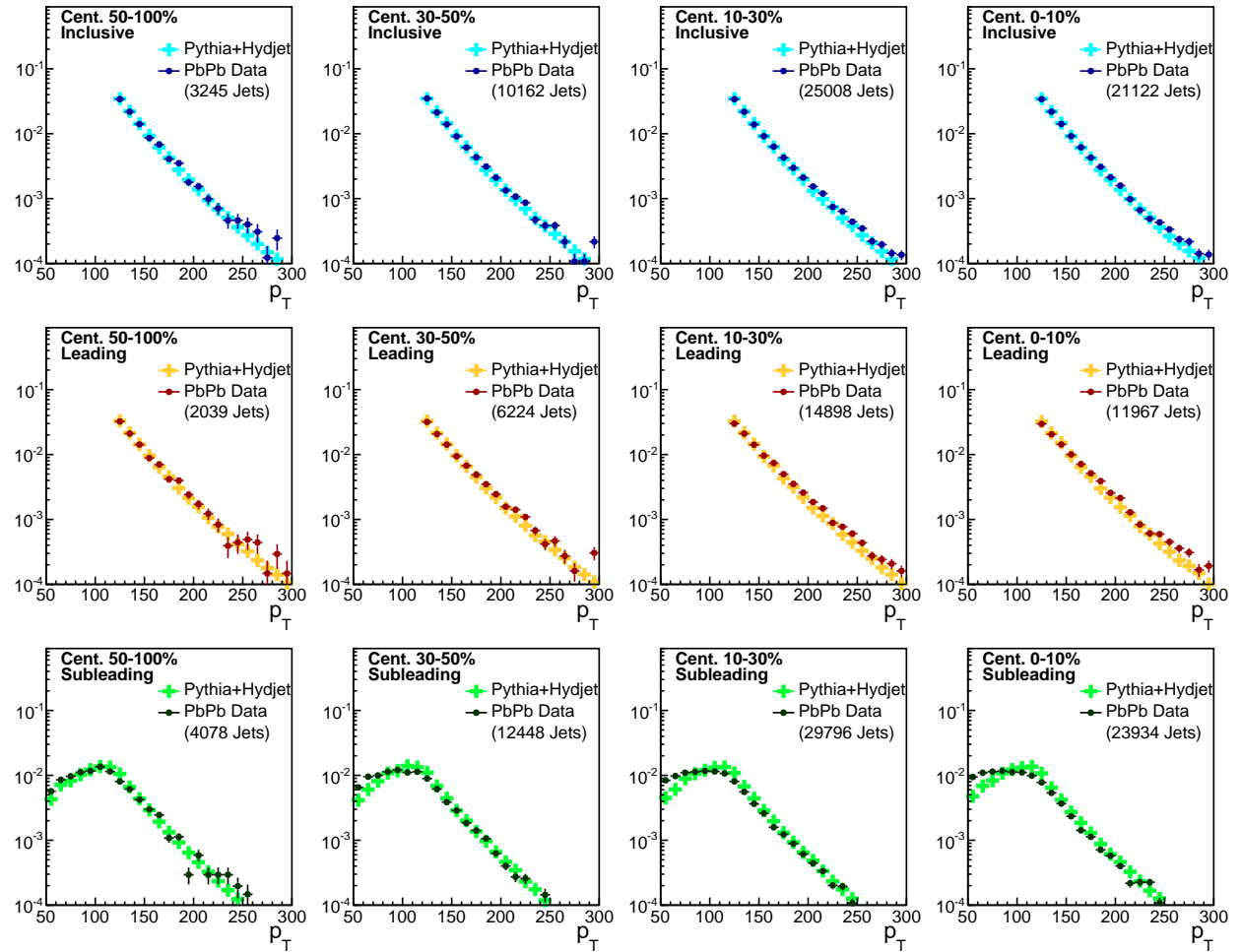


Figure 58. Transverse momentum distribution of all jet selections for PbPb data at 2.76 TeV compared to PYTHIA+HYDJET simulation.

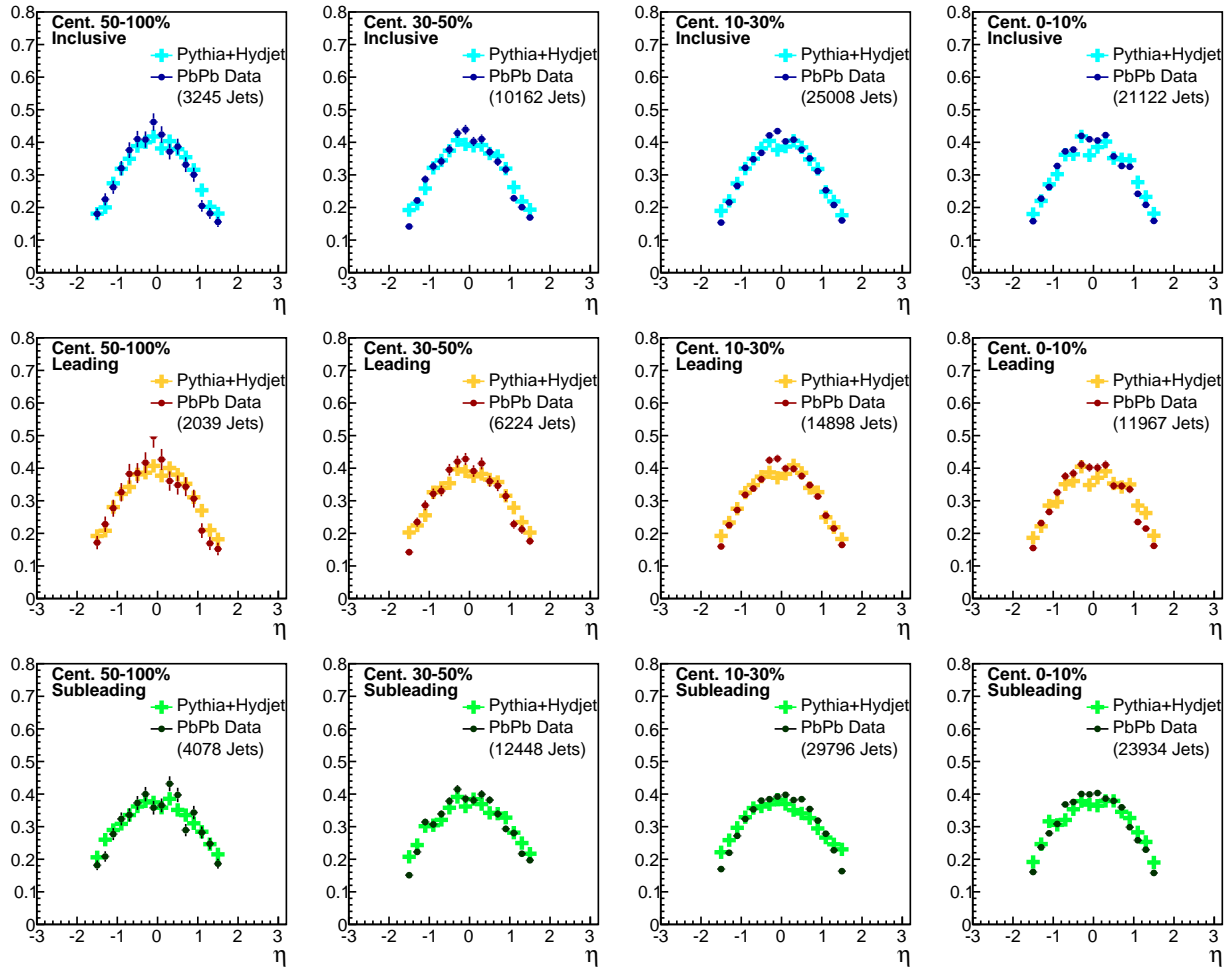


Figure 59. Pseudorapidity distribution of all jet selections for PbPb data at 2.76 TeV compared to PYTHIA + HYDJET simulation.

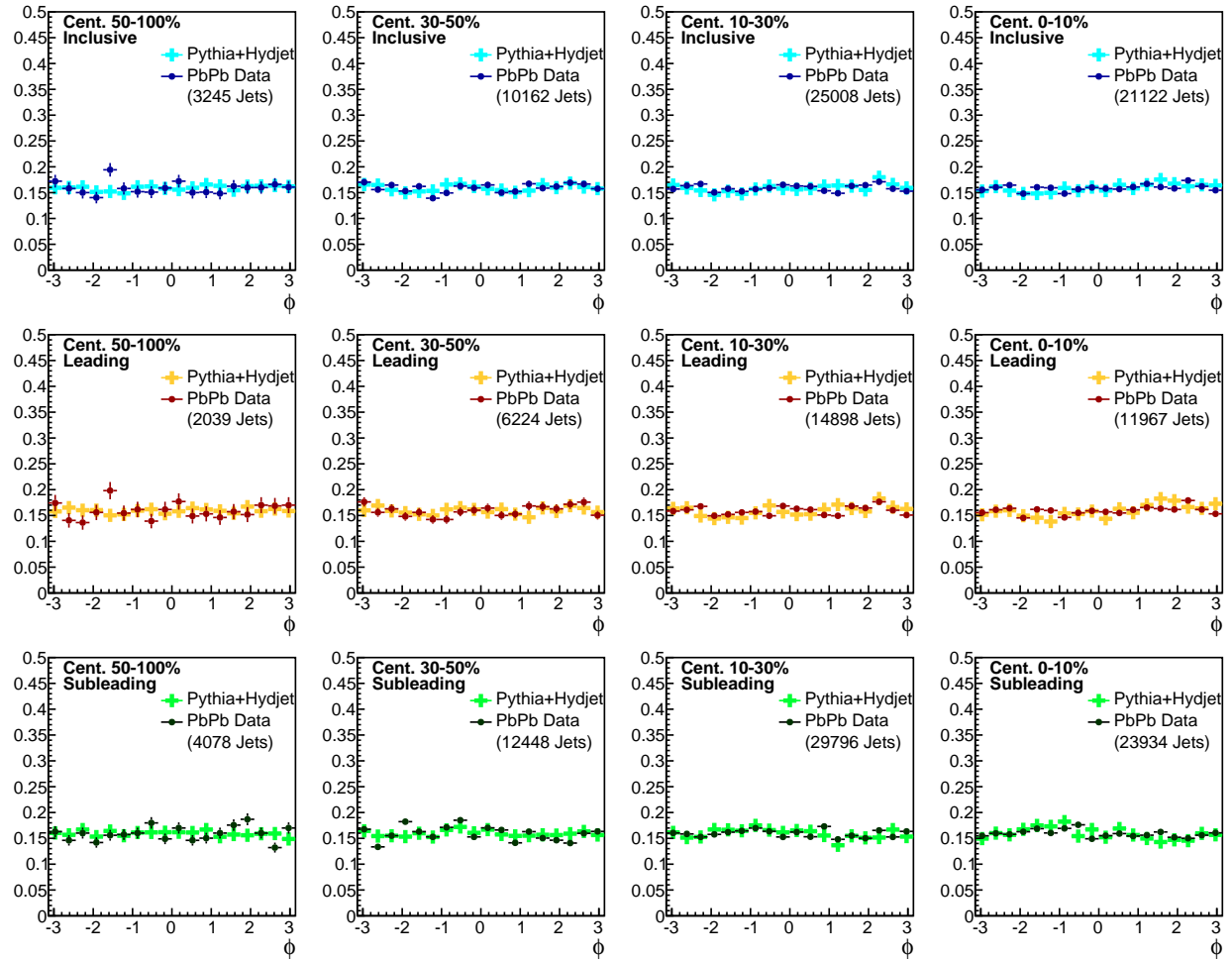


Figure 60. Azimuthal angle distribution of all jet selections for PbPb data at 2.76 TeV compared to PYTHIA+HYDJET simulation for each collision centrality bin.

1171 **A.2 Inclusive jet kinematics at 5.02 TeV**

1172 Jet p_T , η , and ϕ distributions for 5.02 TeV data, comparing PbPb data to PYTHIA+HYDJET and
 1173 pp data to PYTHIA simulation.

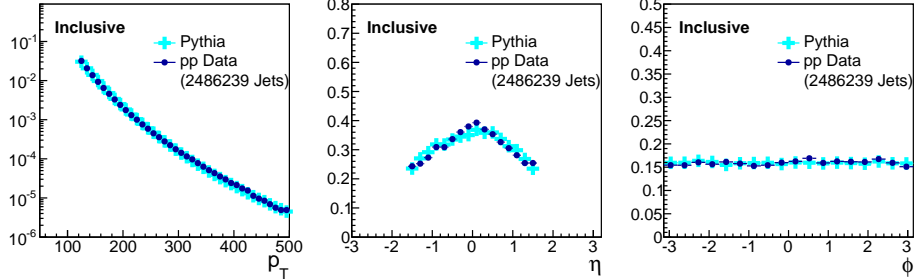


Figure 61. Distribution of pseudorapidity distribution of all jet selections for PbPb data compared to PYTHIA+HYDJet simulation for each collision centrality bin.

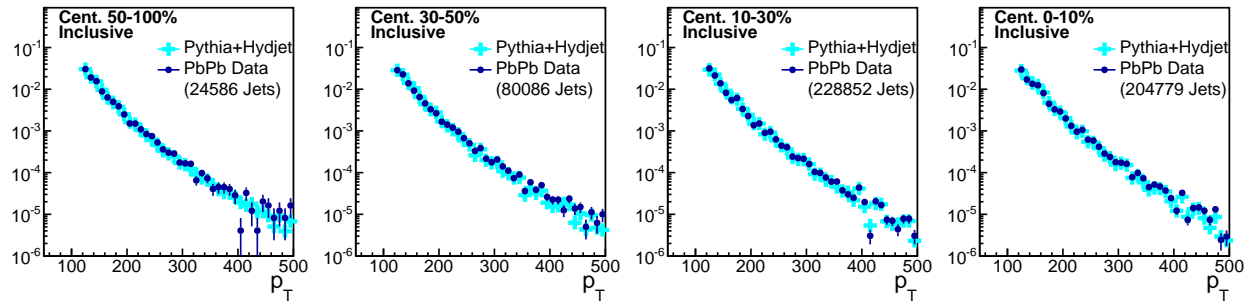


Figure 62. Transverse momentum distribution for PbPb data compared to PYTHIA+HYDJet simulation for each collision centrality bin.

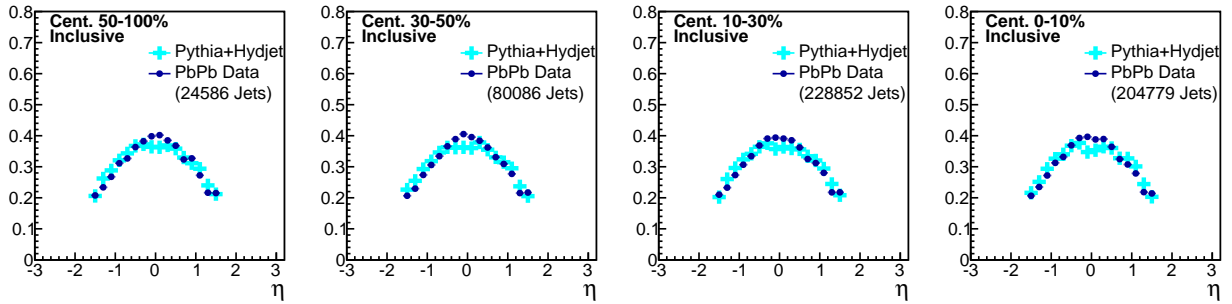


Figure 63. Jet η distribution for PbPb data compared to PYTHIA+HYDJet simulation for each collision centrality bin.

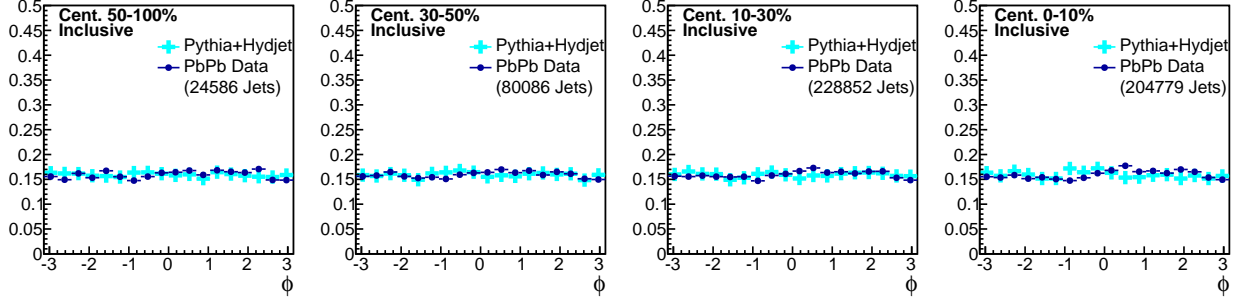


Figure 64. Jet ϕ distribution for PbPb data compared to PYTHIA+HYDJET simulation for each collision centrality bin.

¹¹⁷⁴ **A.3 Dijet kinematics in asymmetry classes at 2.76 TeV**

¹¹⁷⁵ In the figures below, jet transverse momentum, pseudorapidity, and azimuth are shown for our A_J -
¹¹⁷⁶ inclusive sample, compared to each A_J selection in our analysis. Note that A_J -selection primarily
¹¹⁷⁷ affects the subleading jet spectrum, while the leading jet spectrum is nearly unchanged. Jet η and
¹¹⁷⁸ jet ϕ exhibit no significant A_J -dependence for leading or subleading jets. Distributions are shown
¹¹⁷⁹ first for pp, and then for PbPb data at 2.76 TeV.

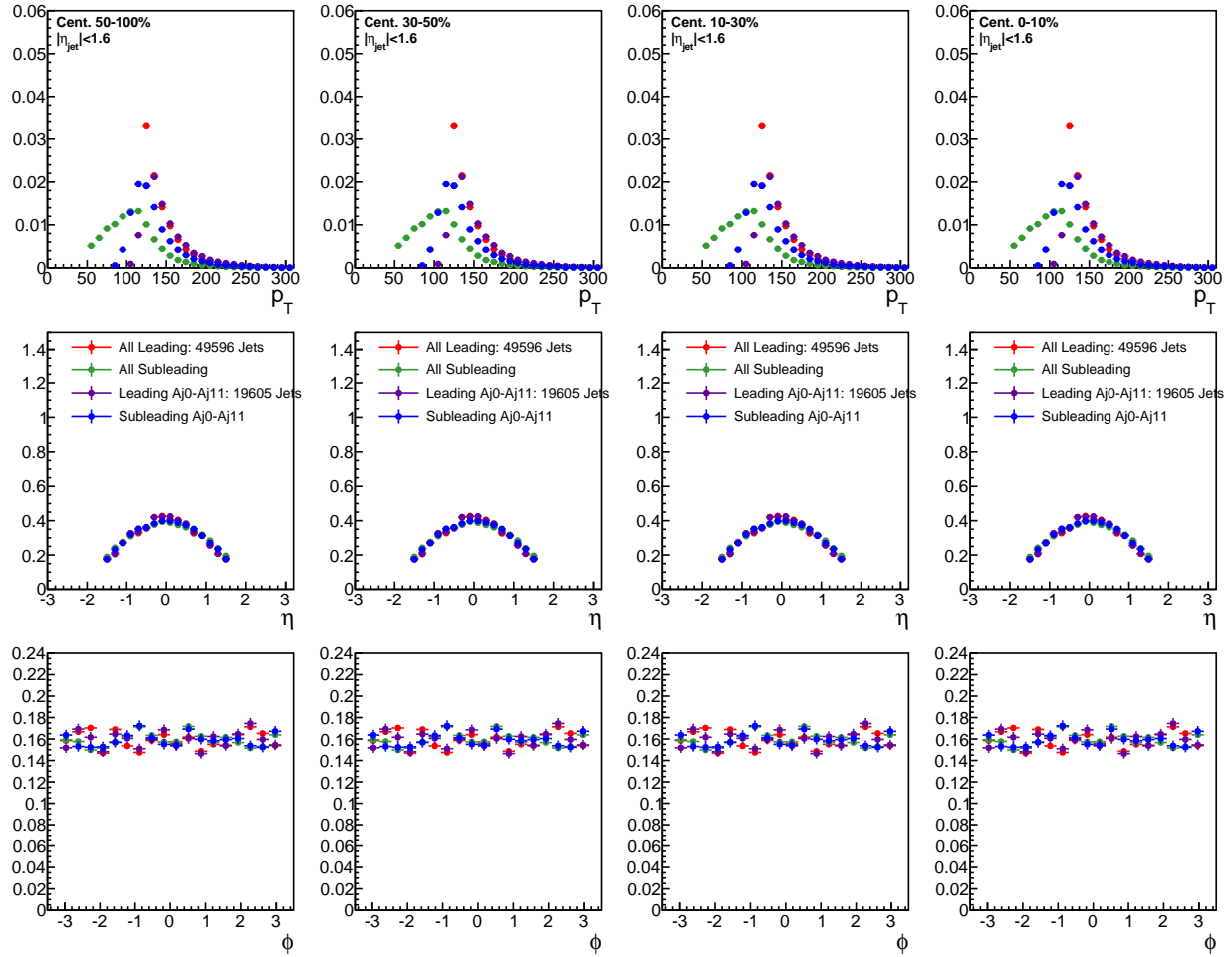


Figure 65. Jet p_T , η , and ϕ for all pp dijets and for pp dijets with A_J : $0 < A_J < 0.11$.

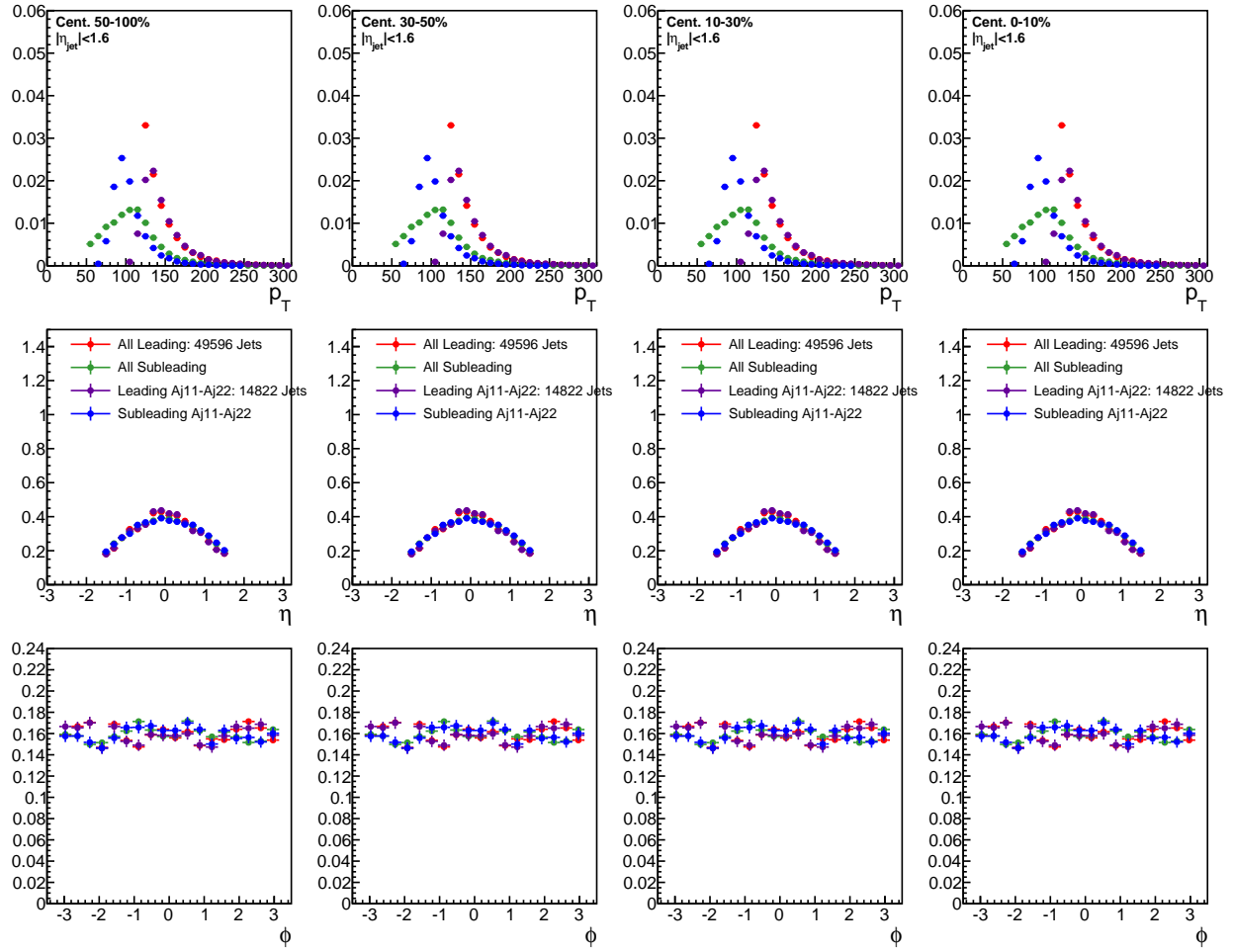


Figure 66. Jet p_T , η , and ϕ for all pp dijets and for pp dijets with A_J : $0.11 < A_J < 0.22$.

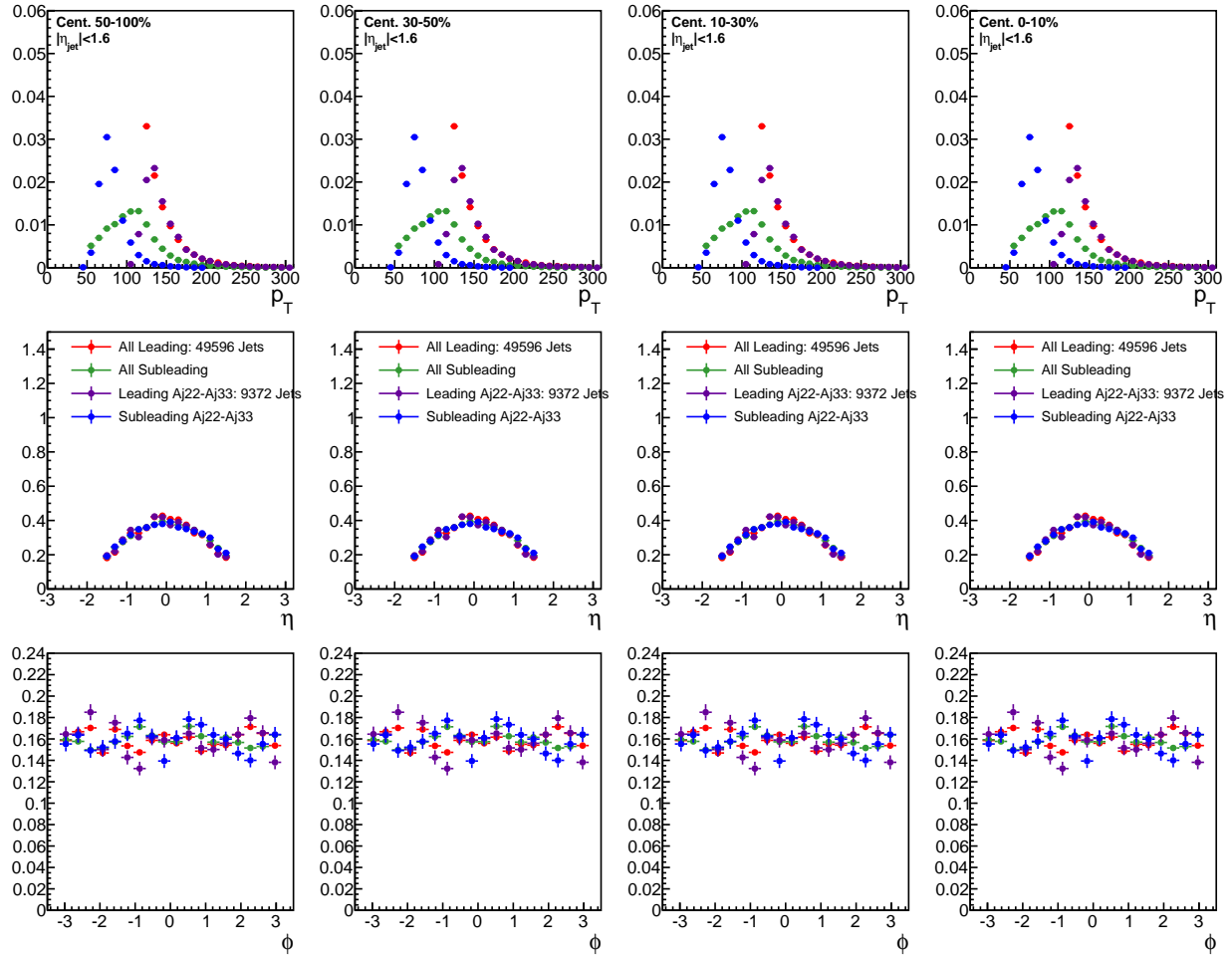


Figure 67. Jet p_T , η , and ϕ for all pp dijets and for pp dijets with A_J : $0.22 < A_J < 0.33$.

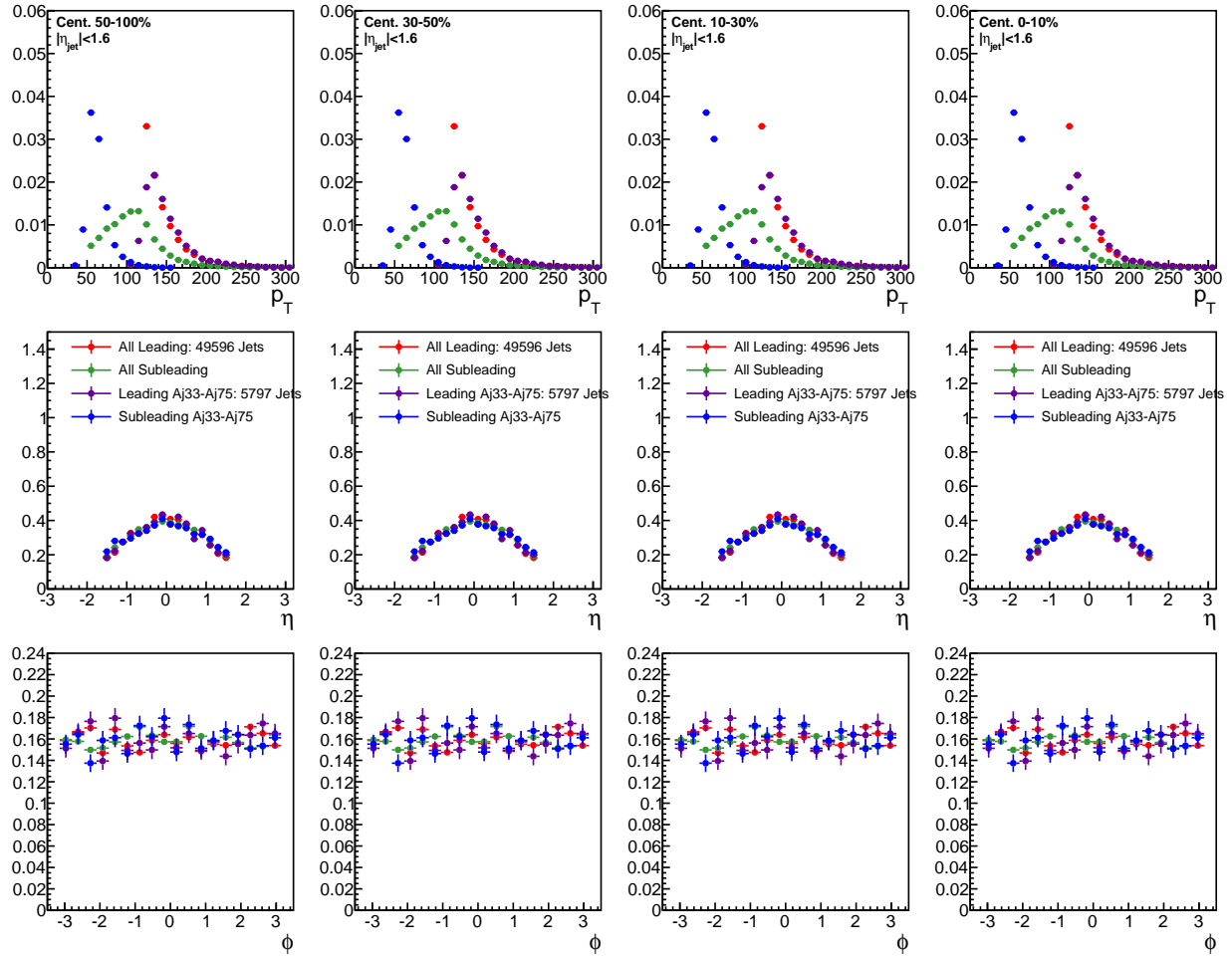


Figure 68. Jet p_T , η , and ϕ for all pp dijets and for pp dijets with A_J : $A_J > 0.33$.

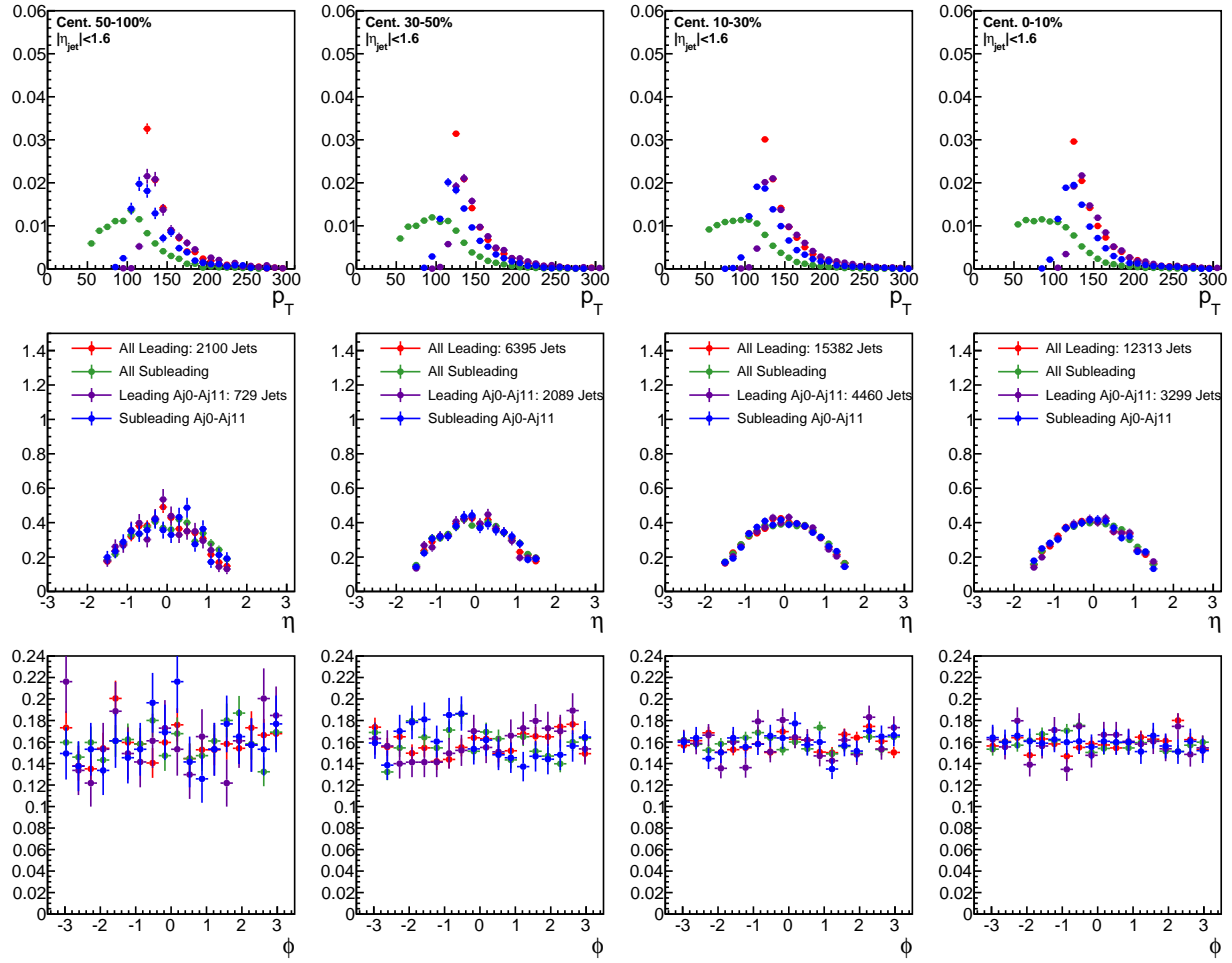


Figure 69. Jet p_T , η , and ϕ for all PbPb dijets and for PbPb dijets with $0 < A_J < 0.11$.

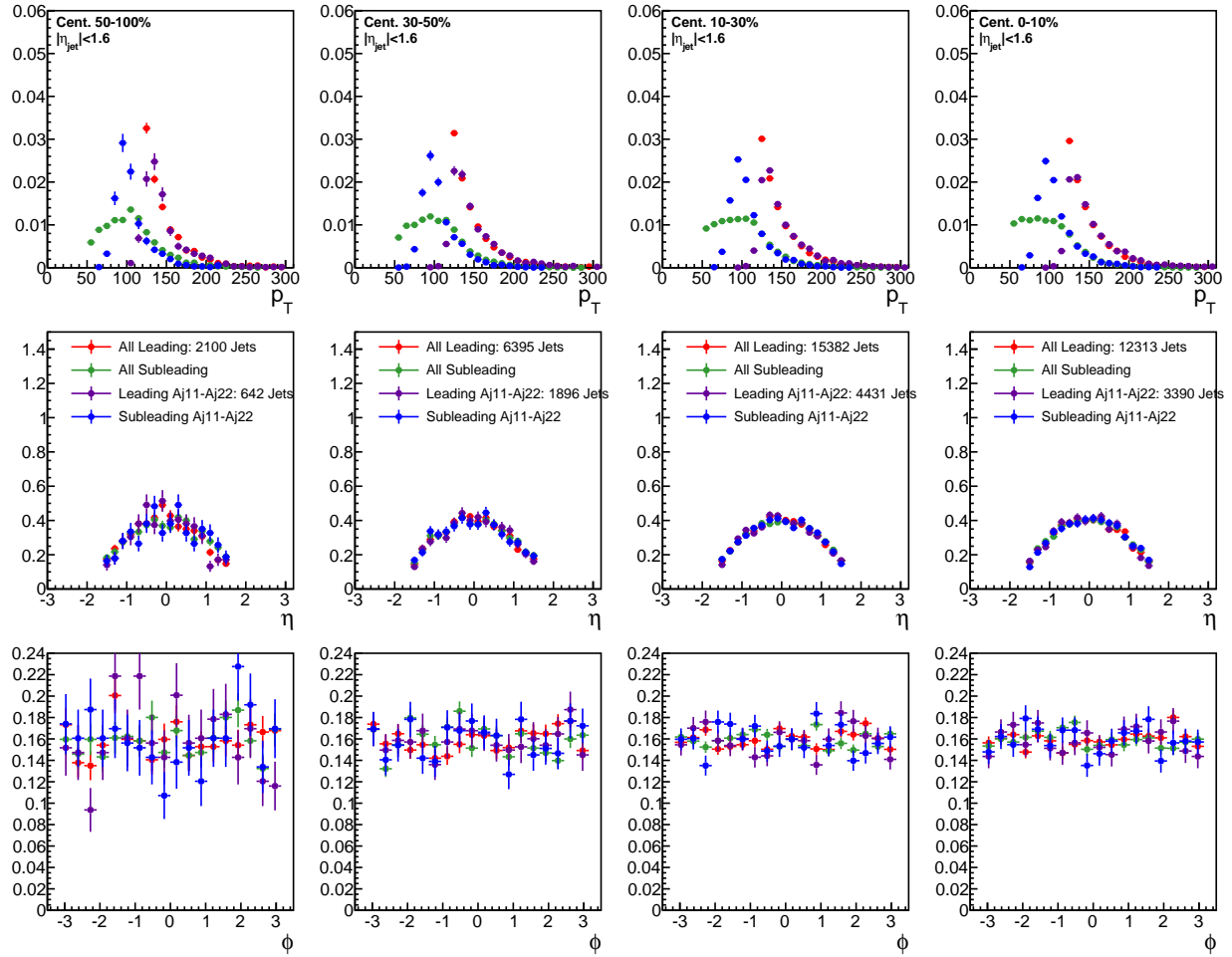


Figure 70. Jet p_T , η , and ϕ for all PbPb dijets and for PbPb dijets with $0.11 < A_J < 0.22$.

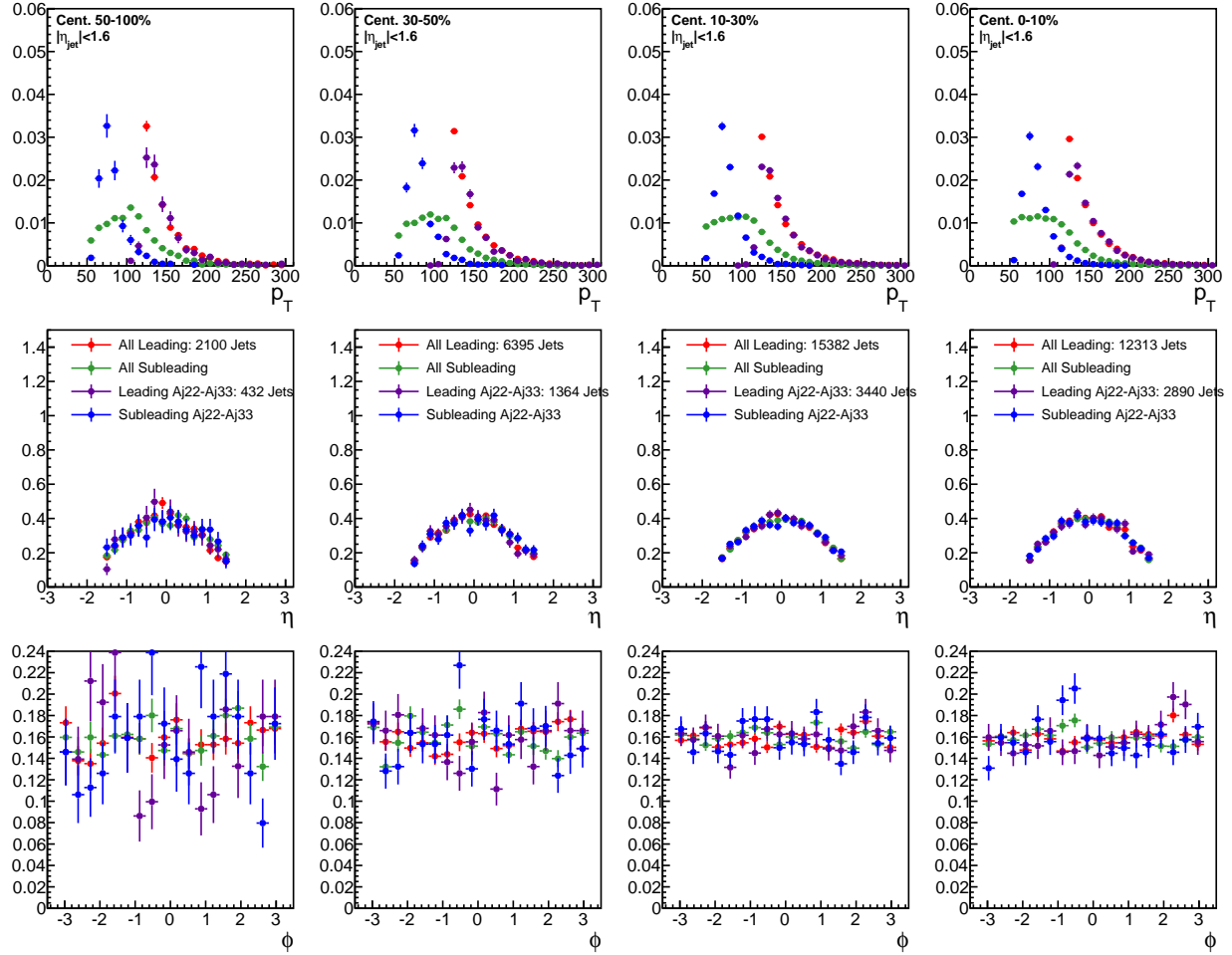


Figure 71. Jet p_T , η , and ϕ for all PbPb dijets and for PbPb dijets with $0.22 < A_J < 0.33$.

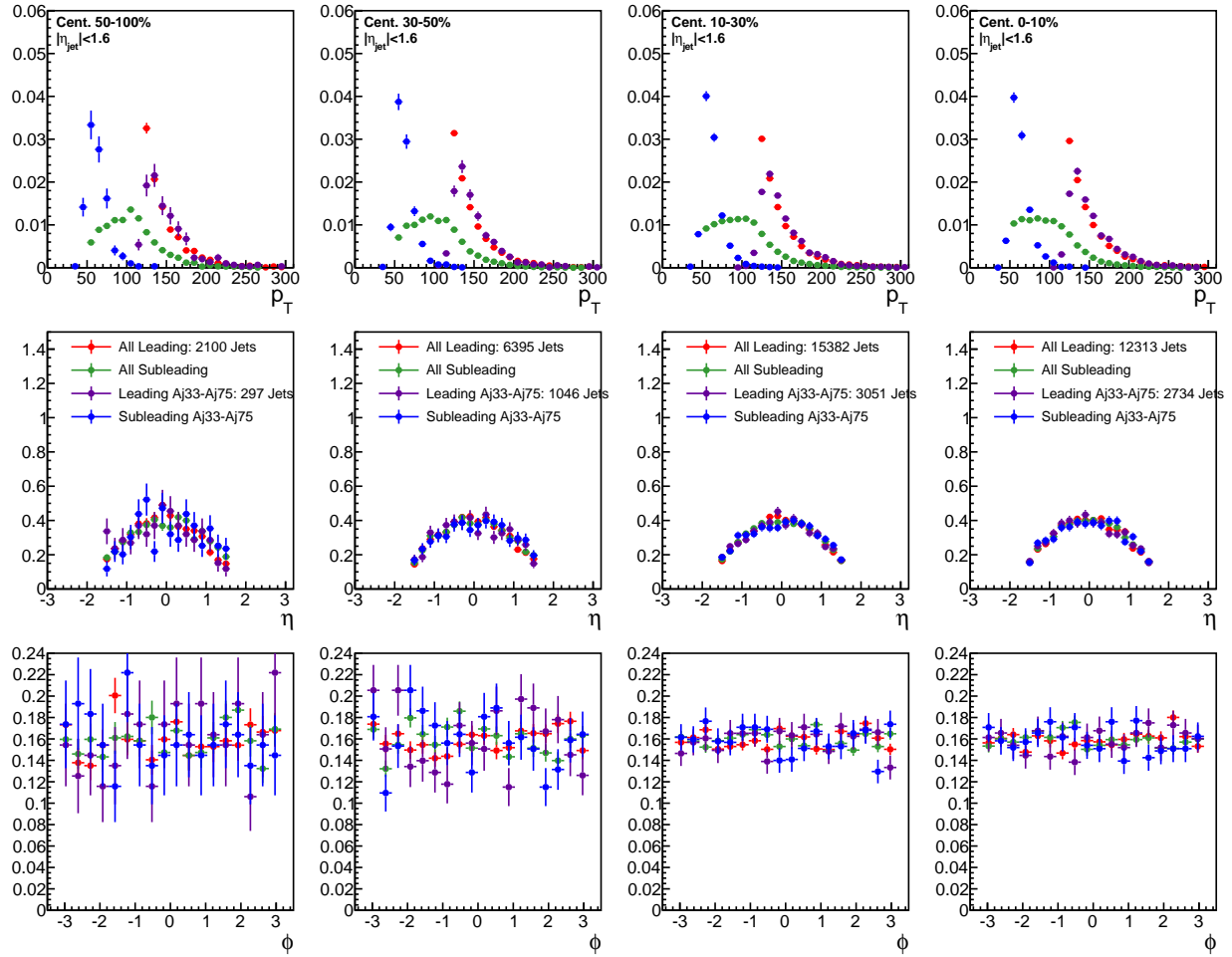


Figure 72. Jet p_T , η , and ϕ for all PbPb dijets and for PbPb dijets with $A_J > 0.33$.

1180 **B Background fitting details**

1181 Figures 73-76 show the two steps of fits involved in modeling the background distribution in
 1182 $\Delta\phi$, as discussed in section 7.3.

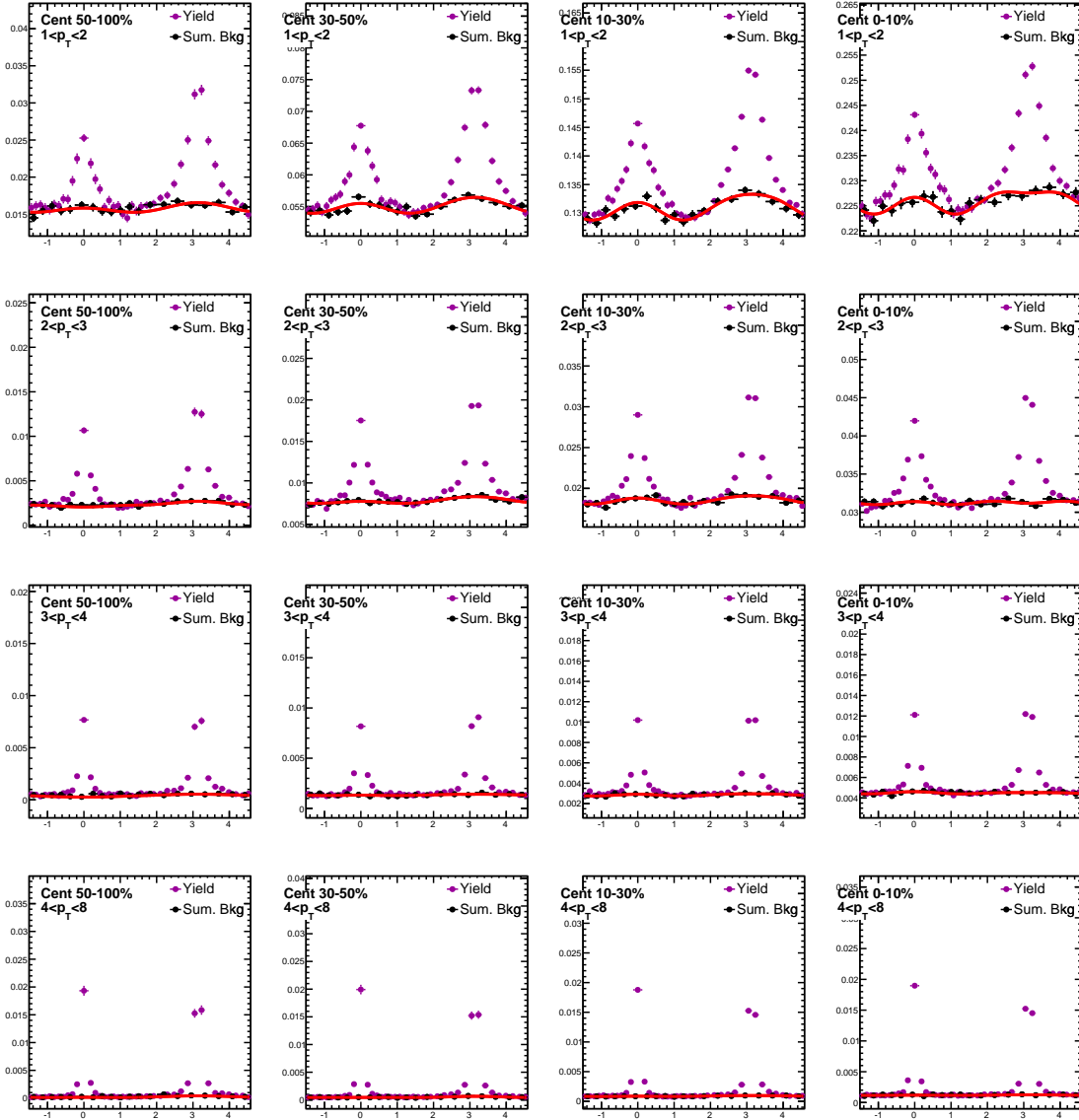


Figure 73. Dijet combined background $\Delta\phi$ distributions, estimated by projection over the region $1.5 < |\Delta\eta| < 3.0$. Here the "near-side" region $-\frac{\pi}{2} < \Delta\phi < \frac{\pi}{2}$ is taken from the leading jet correlation, while the "away-side" $-\frac{\pi}{2} < \Delta\phi < \frac{\pi}{2}$ is taken from the subleading jet correlation. The resulting combined background distribution is fit with the function $B^{dijet}(\Delta\phi) = B_0(1 + 2V_1\cos(\Delta\phi) + 2V_2\cos(2\Delta\phi) + 2V_3\cos(3\Delta\phi))$.

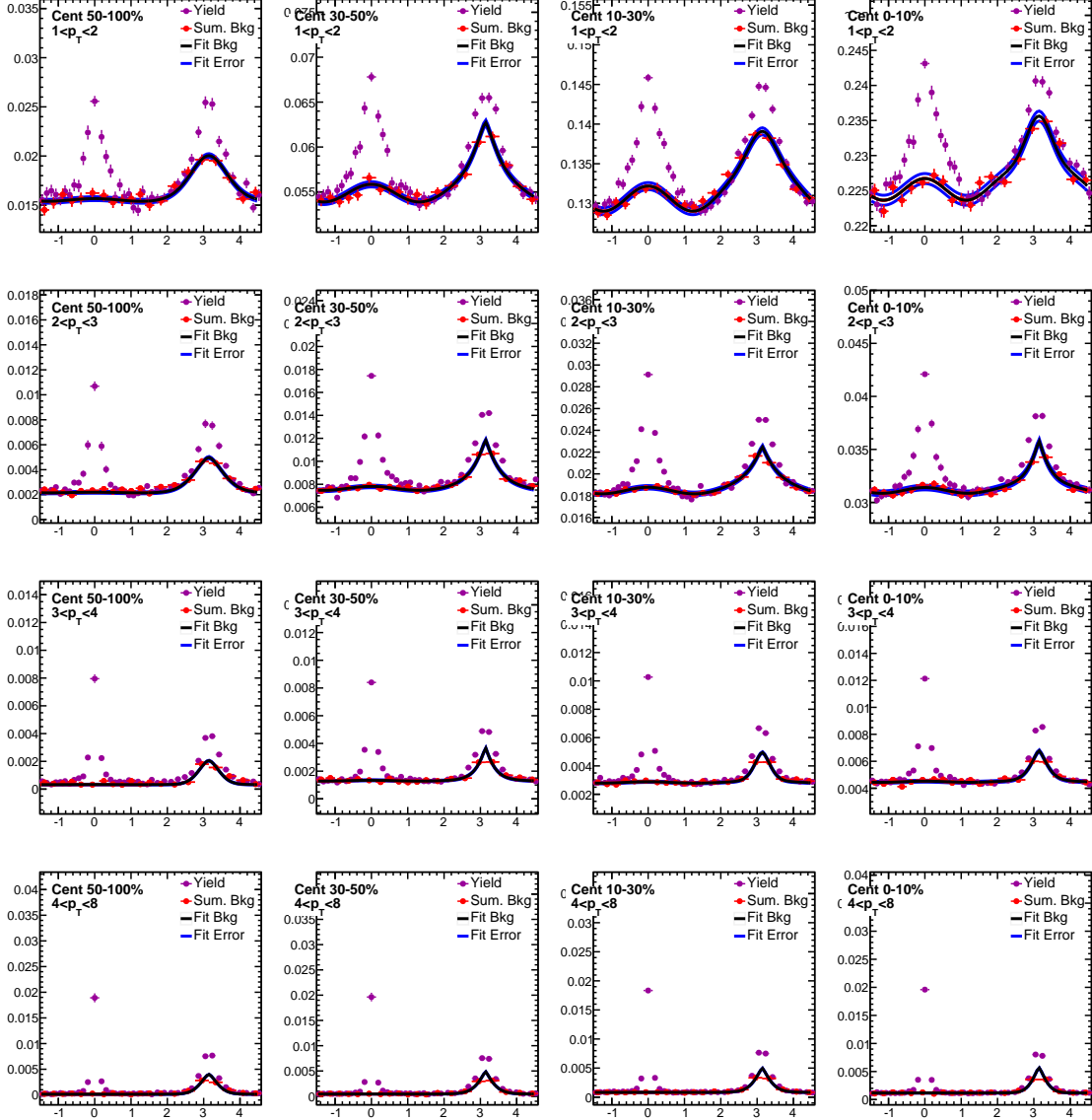


Figure 74. Background leading jet $\Delta\phi$ distributions, estimated by projection over the region $1.5 < |\Delta\eta| < 3.0$, is fit as shown. The 2D background distribution is estimated by propagating the black fit line in $\Delta\eta$, with uncertainty assigned by varying fit parameters by the appropriate fit error as shown in the blue error band.

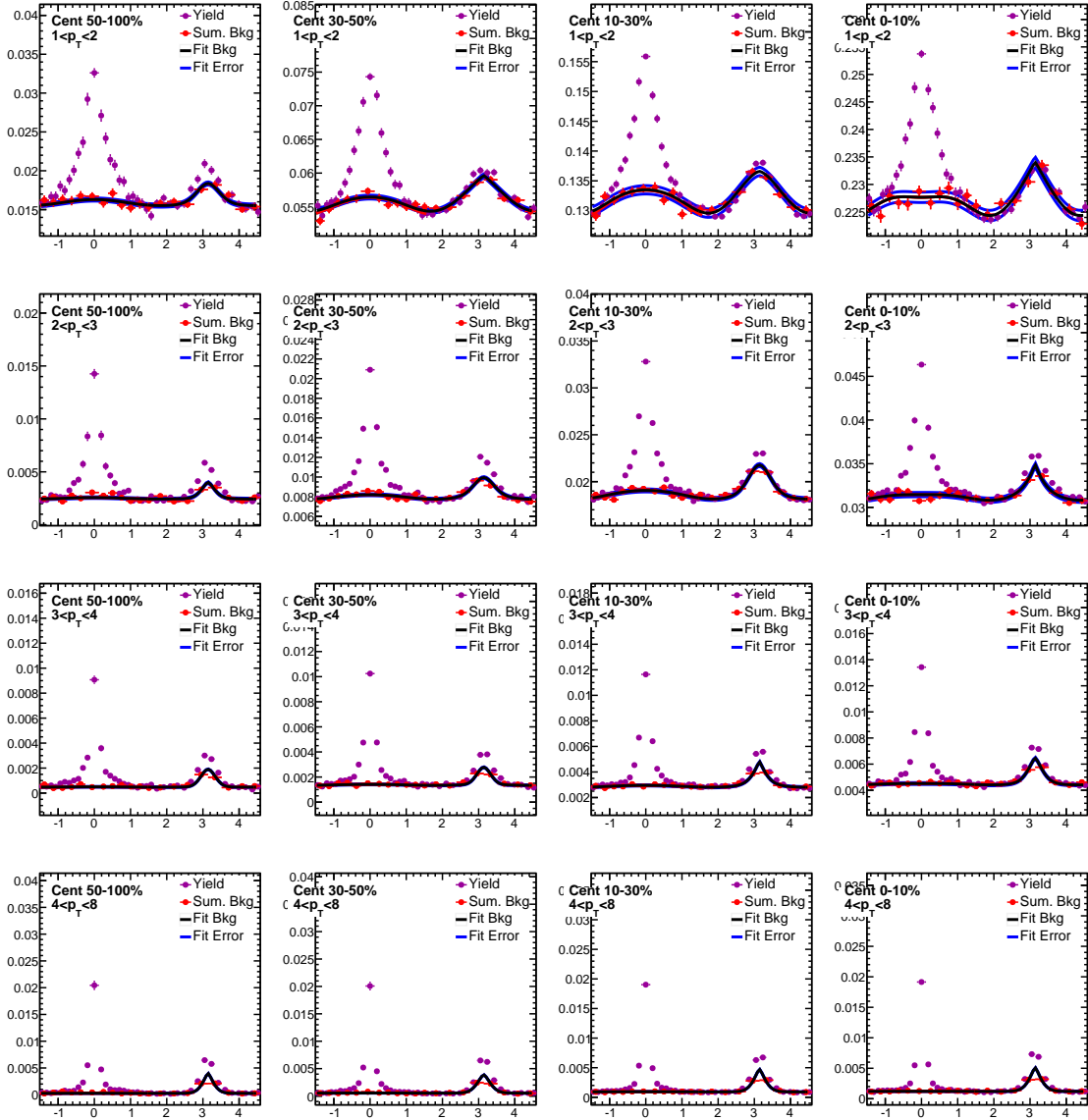


Figure 75. Background subleading jet $\Delta\phi$ distributions, estimated by projection over the region $1.5 < |\Delta\eta| < 3.0$, is fit as shown. The 2D background distribution is estimated by propagating the black fit line in $\Delta\eta$, with uncertainty assigned by varying fit parameters by the appropriate fit error as shown in the blue error band.

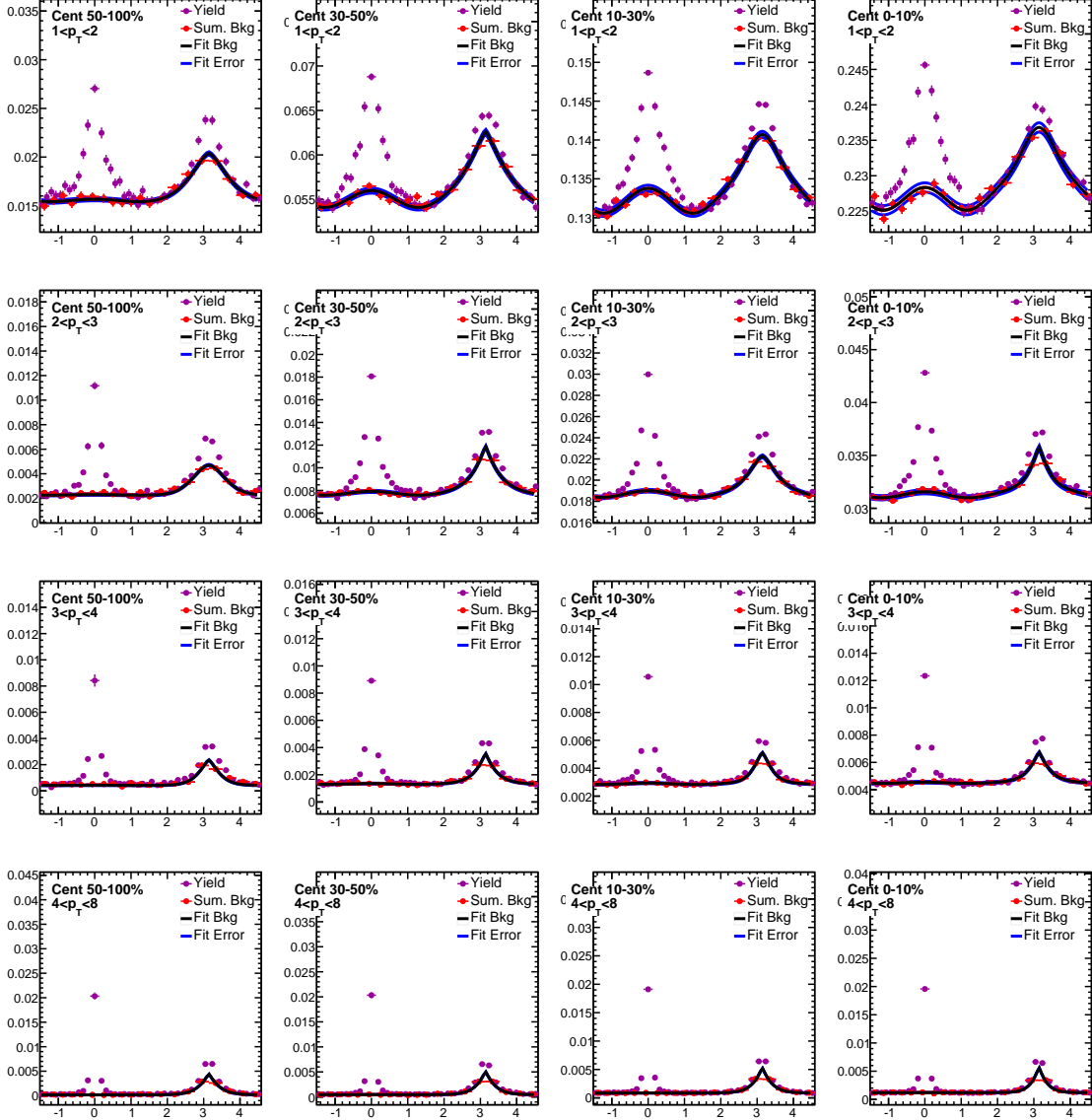


Figure 76. Background inclusive jet $\Delta\phi$ distributions, estimated by projection over the region $1.5 < |\Delta\eta| < 3.0$, is fit as shown. The 2D background distribution is estimated by propagating the black fit line in $\Delta\eta$, with uncertainty assigned by varying fit parameters by the appropriate fit error as shown in the blue error band.

1183 **C Pair acceptance and event decomposition systematic uncertainties**

1184 Figure 77 illustrates the estimation of pair-acceptance uncertainty, determined by considering the
 1185 sideband asymmetry in the $\Delta\eta$ distributions of background subtracted yield.

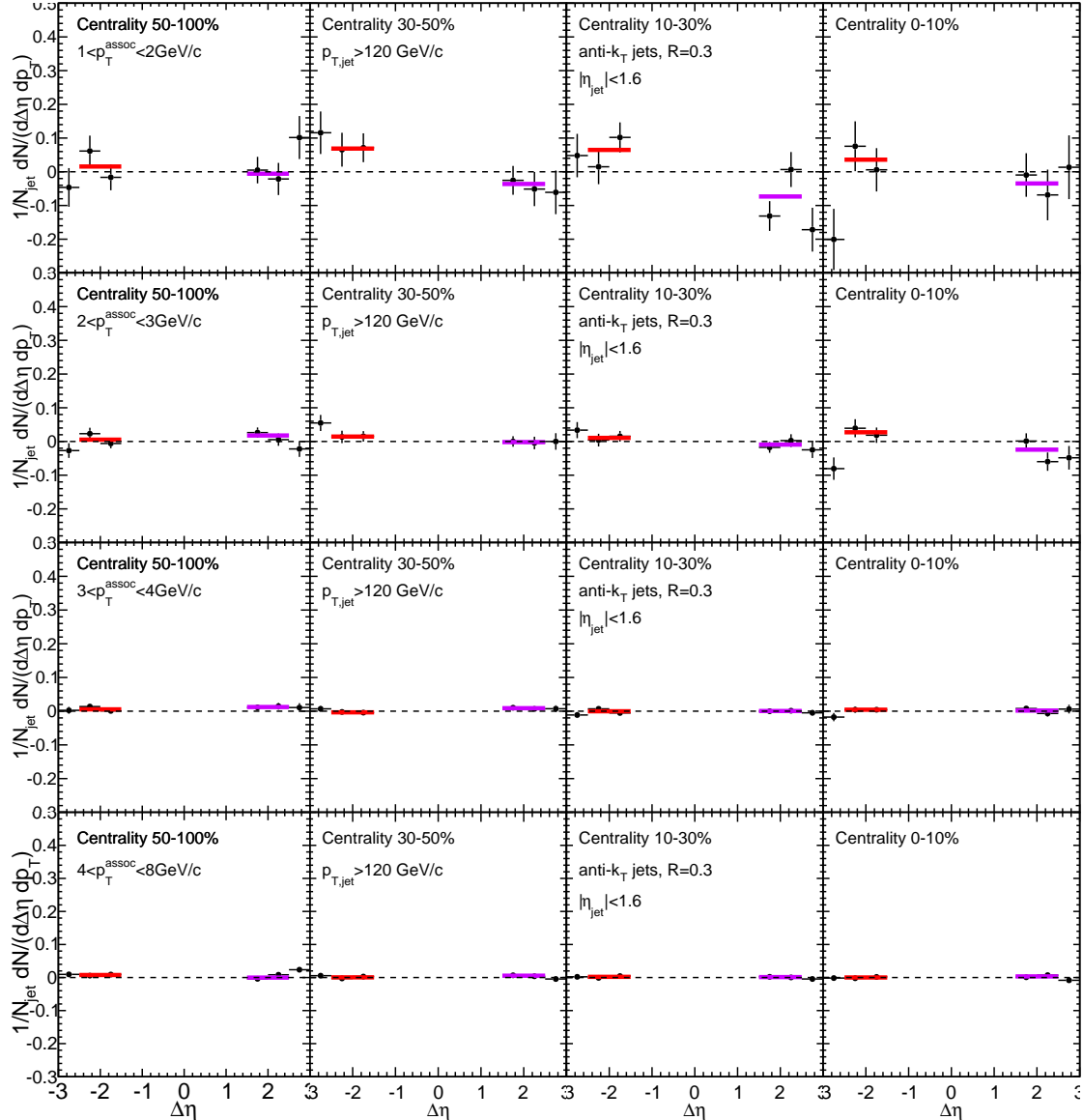


Figure 77. Background-subtracted inclusive jet $\Delta\eta$ distribution is shown for sideband region $1.5 < |\Delta\eta| < 3.0$ only. Each side is fit separately with a horizontal line, and the greater deviation from zero is assigned as systematic uncertainty arising from the pair-acceptance correction.

1186 Figure 78 illustrates the background-subtraction systematic uncertainty estimation: the average
 1187 content of the two $1.5 < \Delta\eta < 2.0$ bins is assigned as systematic uncertainty for each p_T and
 1188 centrality bin.

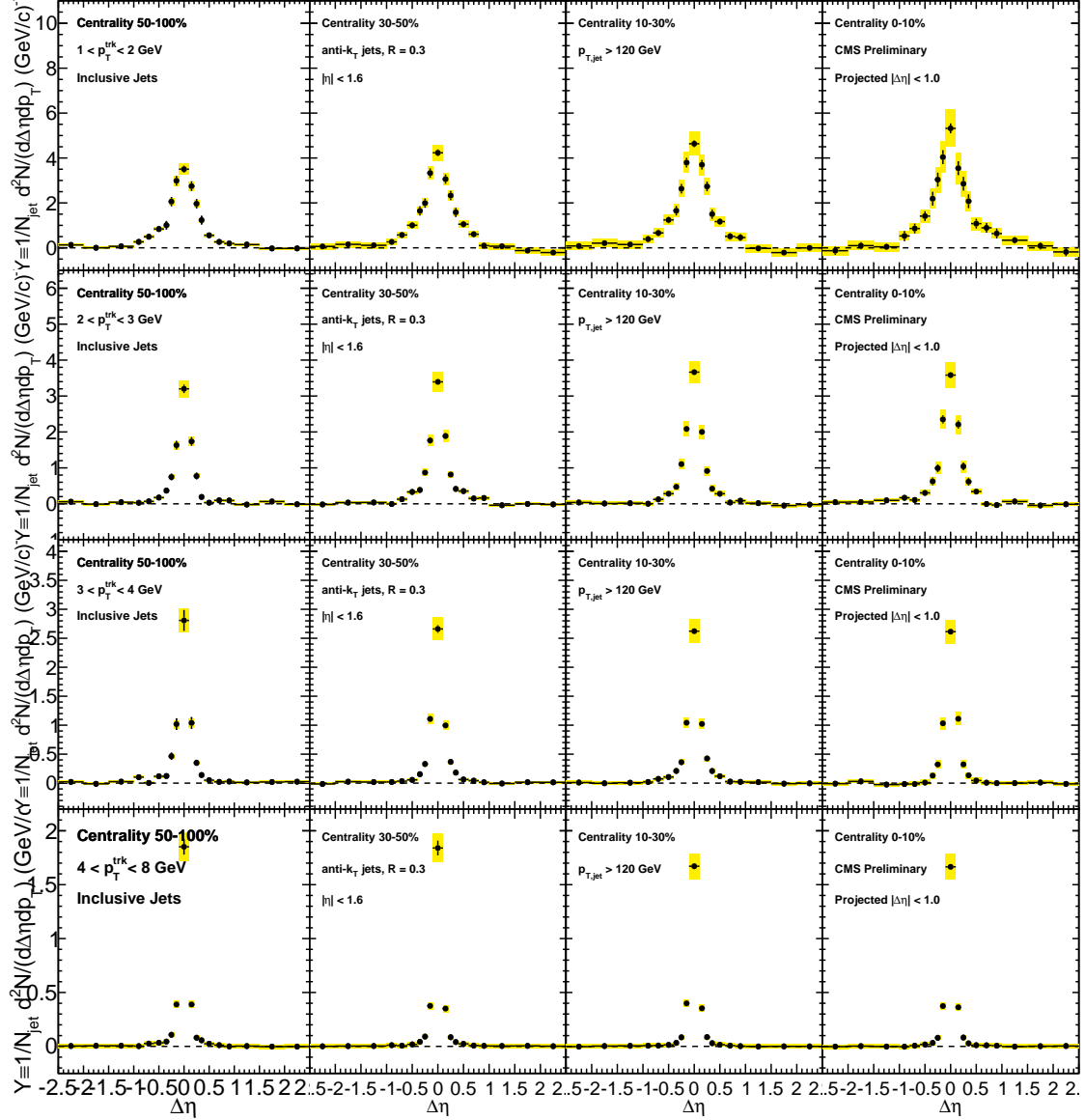


Figure 78. Inclusive jet correlated yield in $\Delta\eta$, shown to axis range $|\Delta\eta| < 2.0$. The deviation of the most peripheral points from zero is assigned as systematic uncertainty as discussed in the Systematic Uncertainty section above.

¹¹⁸⁹ D Correlation widths and related uncertainty

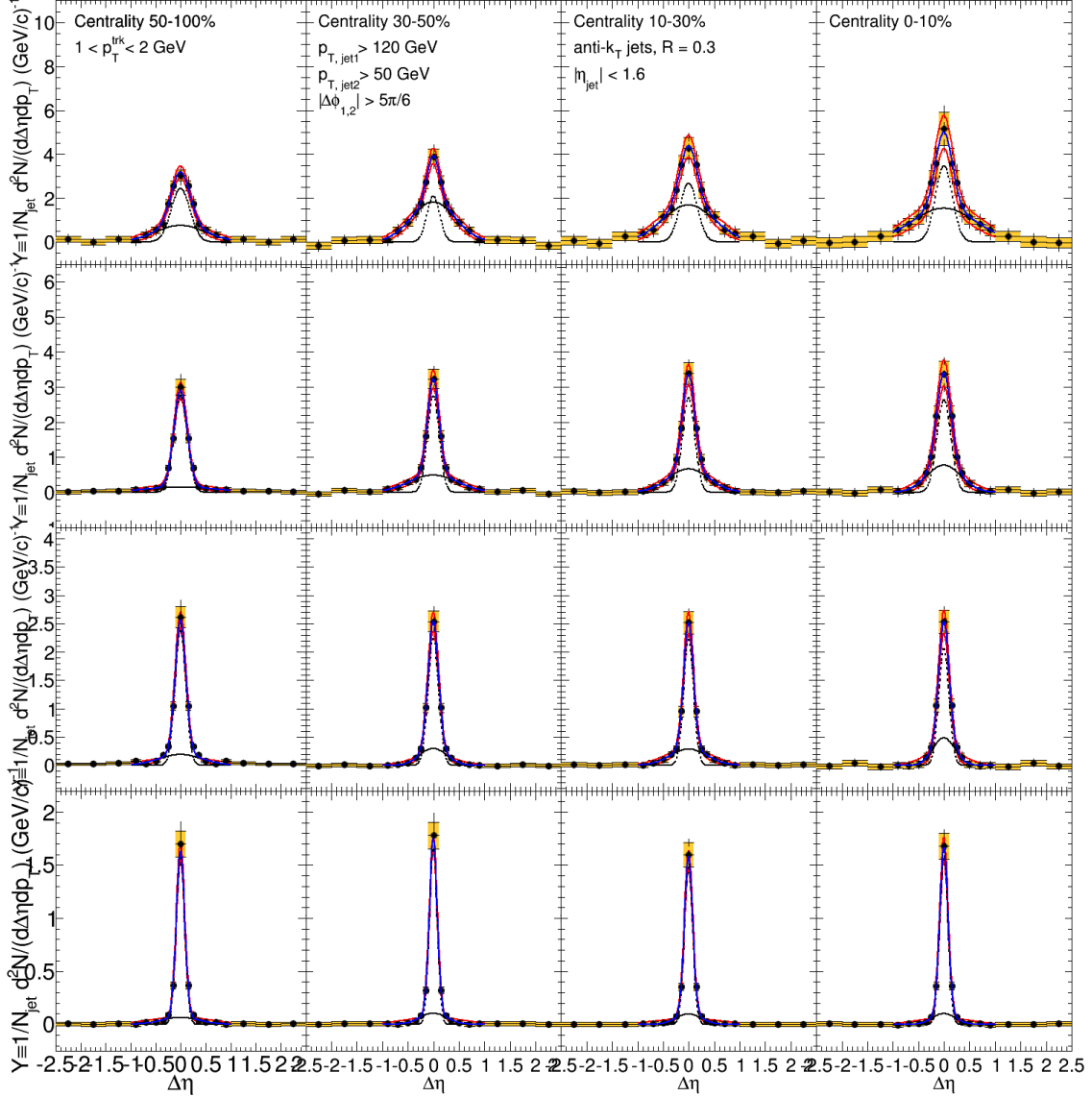


Figure 79. Illustration of the fits used to determine the distribution widths (shown here for leading jet PbPb $\Delta\eta$ correlations). Correlations are fit to a double gaussian (shown in blue, with black dashed lines indicating constituent gaussians), and width is taken as the $\Delta\eta$ value containing 67% of the total yield. Points are varied by their systematic errors and the fits are repeated (shown in red) to obtain the systematic error on the width.

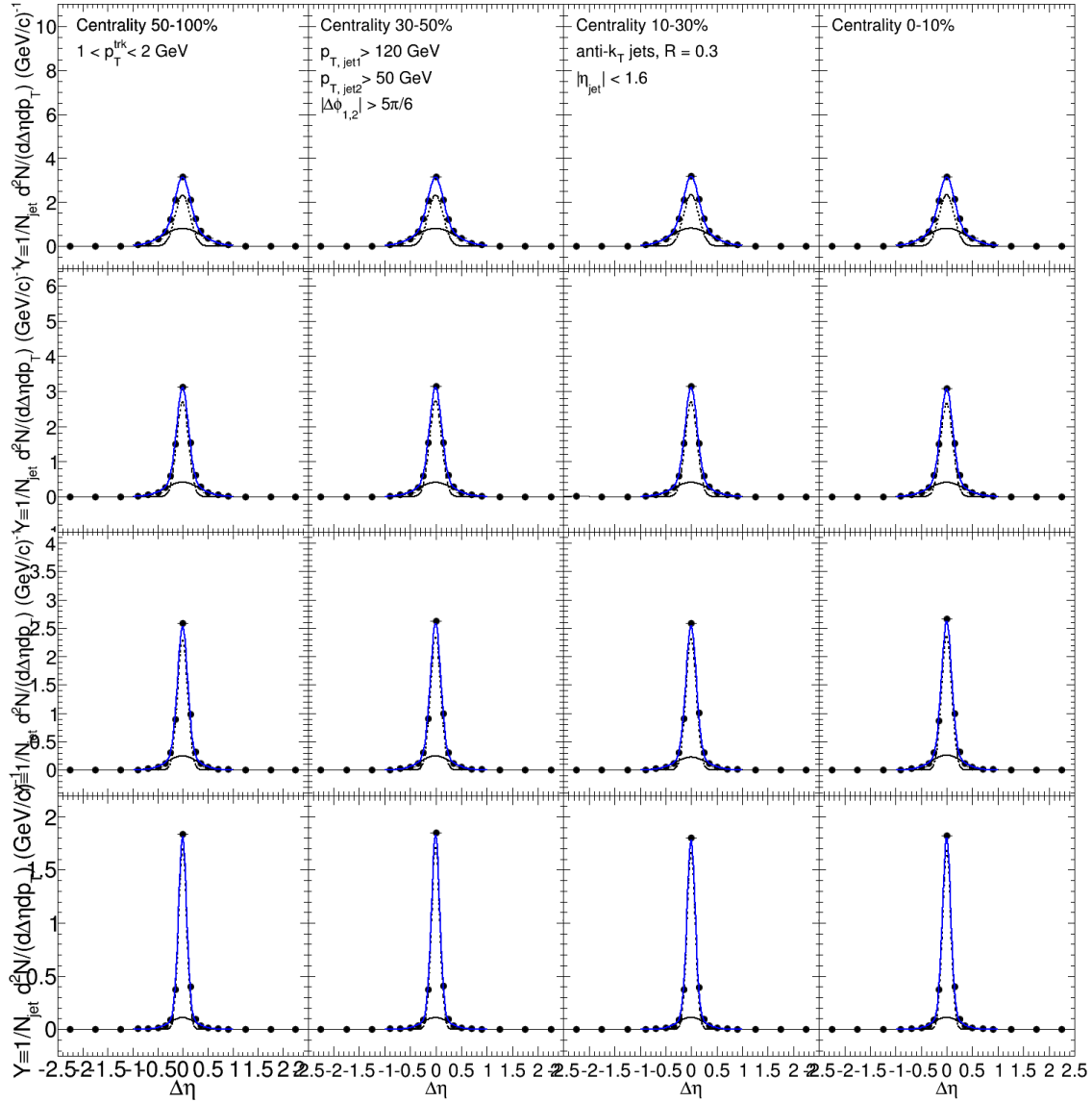


Figure 80. Illustration of the fits used to determine the distribution widths (shown here for leading jet pp $\Delta\eta$ correlations). Correlations are fit to a double gaussian (shown in blue, with black dashed lines indicating constituent gaussians), and width is taken as the $\Delta\eta$ value containing 67% of the total yield.

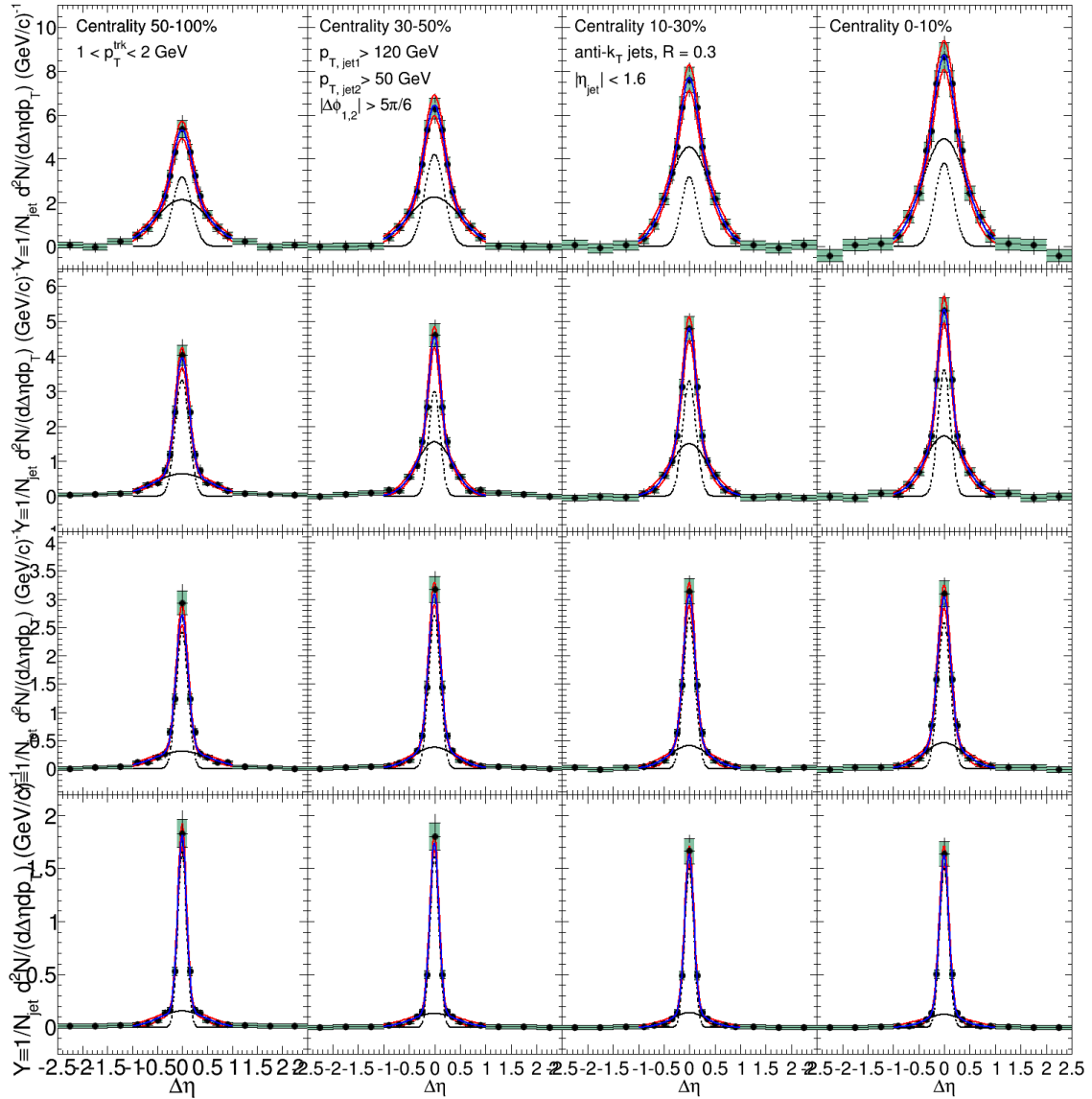


Figure 81. Illustration of the fits used to determine the distribution widths (shown here for sub-leading jet PbPb $\Delta\eta$ correlations). Correlations are fit to a double gaussian (shown in blue, with black dashed lines indicating constituent gaussians), and width is taken as the $\Delta\eta$ value containing 67% of the total yield. Points are varied by their systematic errors and the fits are repeated (shown in red) to obtain the systematic error on the width.

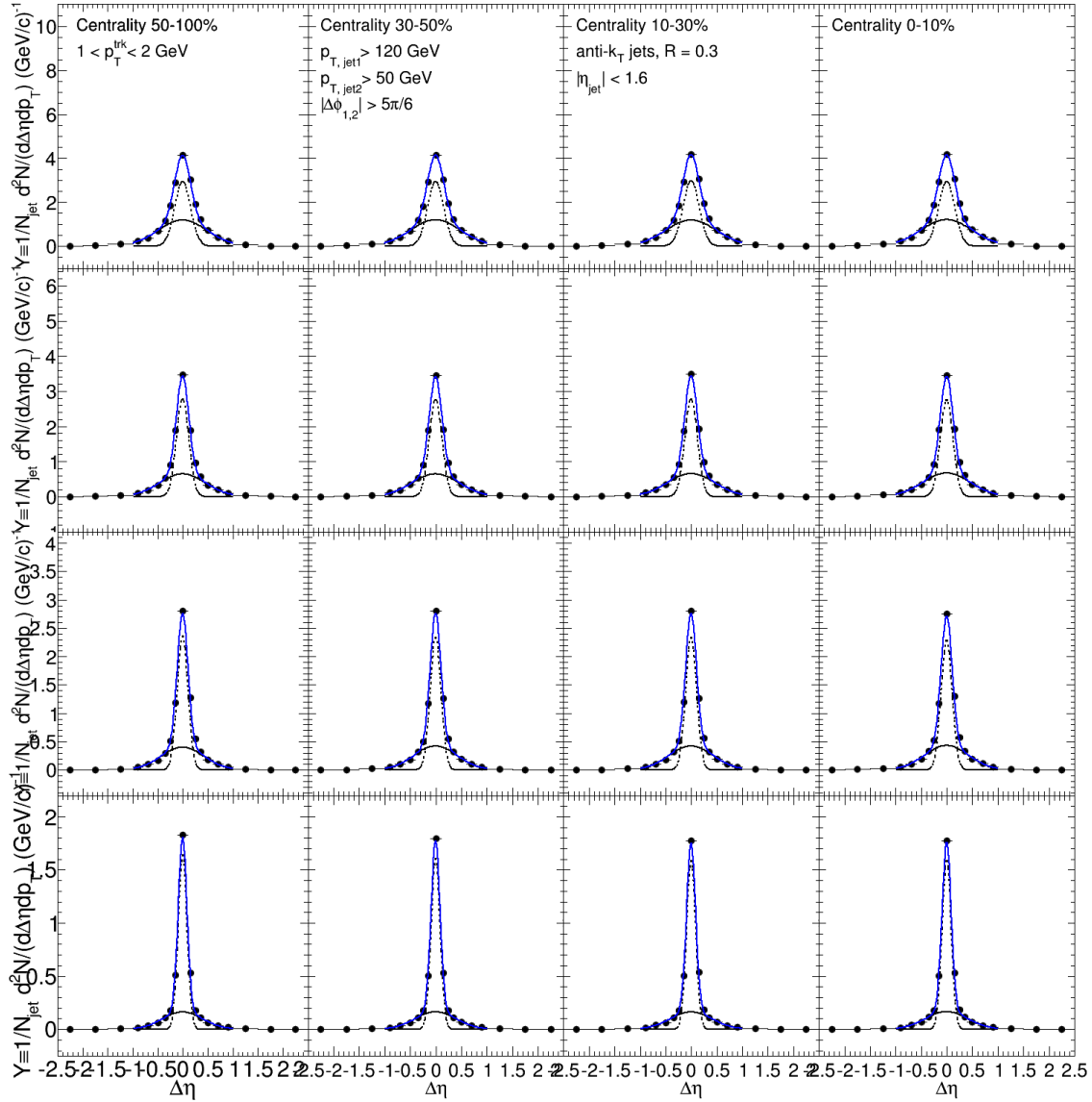


Figure 82. Illustration of the fits used to determine the distribution widths (shown here for sub-leading jet pp $\Delta\eta$ correlations). Correlations are fit to a double gaussian (shown in blue, with black dashed lines indicating constituent gaussians), and width is taken as the $\Delta\eta$ value containing 67% of the total yield.

VITA